MODELING AND ANALYSIS OF TRANSMISSION DYNAMICS OF RESPIRATORY INFECTIOUS DISEASES: CO-CIRCULATIONS, MUTATIONS AND DELAYED INTERVENTIONS

BUSHRA MAJEED

A DISSERTATION SUBMITTED TO THE FACULTY OF GRADUATE STUDIES
IN PARTIAL FULFILMENT OF THE REQUIREMENTS
FOR THE DEGREE OF
DOCTOR OF PHILOSOPHY

GRADUATE PROGRAM IN MATHEMATICS AND STATISTICS
YORK UNIVERSITY
TORONTO, ONTARIO

JUNE 2025

Abstract

Mathematical models are essential tools for understanding the transmission dynamics of infectious diseases and evaluating control strategies. This thesis develops compartmental mathematical models to investigate key issues observed during the COVID-19 pandemic, including the emergence of variants of concern (VOC) due to mutations, the co-circulation of respiratory pathogens, and the impact of delayed interventions. The first model assesses the effects of mutations, focusing on the emergence of new variants and variant-specific control strategies. The model analysis emphasizes the importance of rapid detection through whole genome sequencing (WGS) to manage outbreaks from two strains effectively. The second model considers concurrent epidemics of COVID-19 and influenza. The model simulates the transmission dynamics of both viruses and optimizes vaccination strategies to minimize strain on healthcare systems by delaying or separating peak infections. Finally, time-dependent removal rates are incorporated into classical SIR models to account for delays in diagnosis and isolation due to limitations of healthcare resources, and our study shows how this delay leads to oscillatory dynamics. This thesis research forms appropriate models, develops theoretical analyses, and provides valuable insights into the complex dynamics of respiratory diseases and offers strategies for managing mutations, co-circulation, and delayed interventions, ultimately improving pandemic preparedness.

Dedication

To my wonderful and beloved family

Acknowledgements

I would like to express my deepest gratitude to my supervisor, Professor Jianhong Wu, for his invaluable guidance and support throughout my PhD journey. I am also sincerely thankful to my supervisory committee members, Professor Jane Heffernan and Professor Jude Kong, for their insightful feedback and encouragement.

I extend my heartfelt appreciation to my colleagues Bushra Ashref, Denis, Farah, Marco, Mina, and other members of the Laboratory for Industrial and Applied Mathematics (LIAM). Their collaboration, encouragement, and camaraderie have made this journey more rewarding and enjoyable. A special thank you to my husband, Haider, whose unwavering patience, love, and support have been my source of strength throughout this journey. His belief in me has helped me persevere through the challenges of balancing family and academia. My deepest gratitude goes to my children, Bilal, Arfa, and Hira, whose smiles and love have been my greatest motivation. I also extend my heartfelt gratitude to my parents and siblings for their endless prayers and support.

Finally, I appreciate the Department of Mathematics and Statistics at York University for providing a nurturing academic environment. This journey would not have been possible without the kindness and support of so many wonderful people.

Table of Contents

List of Tables

List of Figures

Chapter 1

Introduction

Respiratory viruses significantly impact public health and the economy, as is evident by the recent COVID-19 pandemic, and the seasonal influenza as well as Respiratory Syncytial Virus (RSV) outbreaks.

COVID-19, influenza, and RSV are highly contagious infectious respiratory diseases caused by Severe Acute Respiratory Syndrome coronavirus 2 (SARS-CoV-2), Orthomyxoviridae RNA viruses, and Respiratory Syncytial Virus respectively. Infections from any of these viruses may lead to a spectrum of respiratory symptoms and disease severity, contributing to substantial morbidity, mortality, and economic losses worldwide [1, 2, 3]. Although coming from different families of viruses and varying in their genomic structures, the symptoms they cause in infected individuals are very similar. As such, when these viruses co-circulate, clinical distinction among these infections is often challenging, potentially delaying the testing and treatment, and amplifying the risk of rapid community spread. Delays in testing and isolating infected individuals can significantly accelerate disease transmission by allowing undiagnosed cases to remain in contact with susceptible individuals for extended periods, increasing secondary infections. Early detection followed by isolation has long been a cornerstone of infectious disease control and was widely adopted during the pre-vaccine phase of the COVID-19 pandemic. However, when testing and isolation are delayed, the effectiveness of

these measures diminishes. A prolonged response results in a low detection ratio, meaning that by the time an infected individual is identified, they may have already transmitted the disease to others. This, in turn, leads to resource limitations, overwhelming healthcare systems, and reducing the capacity to test, trace, and isolate effectively. This can destabilize the system, leading to oscillatory dynamics where infections rise and fall in repeated waves. Such waves have been observed in real-world outbreaks, where slow responses prolong the epidemic. In addition, constant mutations of viral pathogens may lead to the emergence of new variants of concern with potentially high transmissibility and severity of infection and impose significant challenges to effective and timely public health responses.

Keeping infectious diseases under control and preventing their spread has always been a public health challenge. Many control and prevention strategies can be applied before and during an infectious disease outbreak. Proper understanding through mathematical modeling of the transmission of these evolving pathogens may facilitate devising prevention tools including non-pharmaceutical measures and vaccine deployment and utilization optimization. The ability of mathematical models to pose and address specific questions allows for prediction-making under a range of assumptions. By simulating theoretical scenarios, these models offer a comprehensive way to explore complex disease dynamics and assess the potential impact of different interventions. In addition, mathematical models play a crucial role in evaluating the effectiveness of control measures and assessing a pathogen's potential to spread within a population [4]. They provide rapid, evidence-based assessments of prevention strategies, helping policymakers identify the most effective approaches to reducing disease burden. These models also aid in determining the optimal timing and intensity of interventions, ensuring maximum effectiveness while minimizing disruptions to society and the economy. It is therefore important to understand and analyze the spread and persistence to inform possible control and/or elimination strategies of these co-circulating multi-variant viral pathogens in order to prevent new and concurrent outbreaks. Various mathematical and statistical models

have been formulated to examine the patterns of infectious diseases when control measures are applied. Overall, the insights gained through mathematical modeling and simulations not only improve our understanding of infectious disease dynamics but also inform the development and implementation of targeted strategies to reduce the health and economic impacts of epidemics and pandemics. Simulations are also used when data collection is costly or numerous scenarios need to be evaluated. New emerged pandemics such as the severe acute respiratory syndrome (SARS) of 2002–2003, the H1N1 swine flu of 2009 and more recently the COVID-19 pandemic remind us about the significance of epidemiological models. Control measures like testing, isolation, school closures, lockdowns, and vaccination have been critical in mitigating disease spread. However, a deeper understanding of how these interventions impact the control of infectious diseases with similar characteristics and natural histories is still developing.

This thesis aims to improve this understanding by analyzing the dynamics of these diseases using deterministic compartmental models along with relevant mathematical technologies including the theory of dynamical systems and incorporating evolving epidemiological knowledge and public health intervention tools. In early 20th century, 1927, the first and now most well-known compartmental model was used in the study of the transmission of infectious diseases by Kermack and McKendrick. In such compartmental models, the population is split into different classes based on their infectious state, and the movement of people between these classes is governed by ordinary differential equations (ODEs) [5, 6, 7]. These deterministic models assume that populations are completely mixed and ignore the spatial effects of spreading epidemics. For example, the earliest such model, called the SIR model, divides the population into Susceptibles $S(t)$, Infected $I(t)$ and Removed $R(t)$, which are respectively the number of individuals susceptible to infection at time t, the number of infectious individuals at time t and the individuals removed from interactions through recovery or death. The general SIR model is an exceptionally effective framework that serves as a powerful tool

for understanding and analyzing the spread of infectious diseases. This simple model forms the foundation for many complex compartmental models [8, 9, 10, 11]. By modifying its structure, it can be tailored to uncover critical patterns and behaviors within an epidemic or outbreak.

1.1 A Brief Overview of Respiratory Infections of Influenza and COVID-19

When developing a model for the progression of a respiratory viral disease, it is crucial to consider factors such as how the disease spreads, the severity of illness it causes, the potential for new variants to emerge, and the impact of various interventions to control the spread. Respiratory viral pathogens, which affect the respiratory tract (including the lungs, nose, and throat), are responsible for a range of illnesses. Common examples of such pathogens include Influenza, Respiratory Syncytial Virus (RSV), and Severe Acute Respiratory Syndrome Coronavirus 2 (SARS-CoV-2). Influenza is an upper respiratory infectious disease, caused by RNA viruses belonging to the Orthomyxoviridae family, specifically the influenza viruses [12, 13]. It is commonly known as the "flu," that affects all age groups and is a significant cause of morbidity and mortality in humans. There are three types of human influenza: A, B, and C [14]. Influenza A and B viruses are endemic in humans and responsible for annual epidemics across the globe [13]. Influenza is highly seasonal and usually runs in winter. It induce symptoms such as fever, chills, achiness, drowsiness, fatigue, sneezing, coughing, and sore throat [15]. The influenza virus undergoes constant mutations known as antigenic drift (point mutations small changes in the virus) and antigenic shift (gene reassortment that produces a naive virus) [16]. As a result of antigenic drift, different strains appear every year and escape pre-existing immunity. This leads to seasonal influenza epidemics and outbreaks that are hardly predictable. Consequently, developing a new vaccine each year becomes an

absolute necessity, and ongoing research is essential to minimize the associated risk factors and prevent excess mortality. Antigenic shift has caused four pandemics in the past 100 years and continues to kill tens of thousands of people annually. The first pandemic of the last century occurred during World War I in 1918(H1N1) and millions of people were killed during this pandemic worldwide. Three additional influenza pandemics took place in 1957 (H2N2), 1968 (H3N2), and 2009 (H1N1) [17, 18].

Coronavirus disease 2019 (COVID-19) is an infectious disease caused by severe acute respiratory syndrome coronavirus-2 (SARS-CoV-2), which was first publicly reported in the last month of the year 2019, in Wuhan, province of Hubei in China [19]. It quickly spread across the globe, turning into a pandemic. Subsequently, the World Health Organization (WHO) declared a global pandemic on March 11, 2020 [20, 21]. Over the course of the COVID-19 pandemic millions of deaths and hospitalizations have been reported [22]. These reported numbers are in the lower bounds, since there are asymptomatic (individuals who are infectious but do not manifest symptoms) and under-reported cases [23, 24].

SARS-CoV-2 is a highly transmissible respiratory virus that shares symptoms with influenza but is significantly more contagious. One key characteristic that sets SARS-CoV-2 apart is its extended incubation period, which is notably longer than that of influenza.

During the early COVID-19 pandemic, there was an urgent need to understand how to control the rapid spread of the virus and therefore it was critical to develop modeling analyses to assess the effects of various mitigation measures, such as quarantine, isolation, contact tracing, lockdown as well as travel restrictions in the absence of a vaccine or any other treatment. Additional challenges for both public health and modeling emerged with rapid emergence of new variants of the virus. Different SARS-CoV-2 variants had been recognized during this pandemic and some of these variants have caused uncertainty and changes in the dynamics. Characterizations of these variants depend on the type and number of mutations. The World Health Organization (WHO) defines its variants in two main categories: variants

of interest (VOI) and variants of concern (VOC). A VOI may affect transmissibility, disease severity, immune evasion, and diagnostic accuracy. If a VOI demonstrates significantly increased transmissibility, causes severe outcomes or the ability to evade immunity from natural infection or vaccination, it is elevated to a VOC [25].

Several variants of concern have indeed led to a large increase in incidence, hospitalization, and mortality in many countries after more than a year of the initial report of the COVID-19 outbreak. During the COVID-19 pandemic, different strains of the SARS-CoV-2 virus were found [26, 27]. The most common VOC internationally identified include Alpha (B.1.1.7) (identified in September, 2020), beta (B.1.351) (identified in October, 2020), Gamma (P.1)(identified in December, 2020), delta (B.1.617.2)(identified in December, 2020), and omicron (B.1.1.529)(identified in November, 2021).

SARS-CoV-2 variants differ in their characteristics, particularly in terms of contagiousness and severity. Some variants have a significant impact on the number of infected cases, hospitalizations, and deaths. For example, the original strain of SARS-CoV-2 was estimated to have a reproduction number in the range of $2 - 3.5$ [28], whereas the Omicron variant, the most transmissible variant at the time of this thesis, had a reproduction number of 9.5 [29]. These variants often exhibit increased transmissibility, immune escape, and higher virulence, which can render existing interventions less effective. Addressing these challenges requires robust diagnostic and containment strategies, with whole genome sequencing (WGS) playing a pivotal role. WGS is a laboratory technique used to determine the complete DNA sequence of an organism's genome at a single time. In the context of SARS-CoV-2, it allows for the identification and monitoring of mutations in the virus, enabling the detection of new variants and the assessment of their transmissibility, virulence, and potential resistance to vaccines or treatments. The importance of WGS lies in its ability to inform public health responses by providing timely and accurate data on the emergence and spread of variants. This information is critical for devising targeted interventions, such as updating vaccines or implementing

variant-specific containment measures. However, healthcare resource constraints, such as limited testing and isolation capacities, can delay diagnosis and intervention, potentially leading to recurrent waves of infection. Minimizing these delays is essential for effective epidemic control and resource optimization.

Although the end of the global pandemic has been declared May 5, 2023, [30], these variants have contributed to making COVID-19 a long-term public health challenge, similar to seasonal influenza. While the two viruses belong to different families, they share many similarities, including transmission routes, symptoms, and clinical outcomes. Both are spread through direct contact, contaminated surfaces, droplets, and aerosols. Symptoms range from mild cases of fever, cough, and sore throat to severe outcomes like pneumonia and death, particularly in high-risk populations.

Antiviral treatments and vaccines are available to reduce the risk of these diseases. The development of influenza and COVID-19 vaccines is a cornerstone to protect against illness of both diseases and potentially their severe consequences, including hospitalization and fatality [31]. The concurrent circulation of SARS-CoV-2 and influenza viruses is anticipated to persist, necessitating comprehensive, long-term public health strategies to effectively manage both respiratory infections and their complications. Simultaneous circulation of these viruses, given their similar symptoms and diagnostic challenges, has the potential to alter each other's transmission dynamics. For instance, one virus may amplify the spread of the other, creating a complex interaction that can make public health interventions more difficult. Analyzing the impact of such interactions at the population scale can help shape the formulation of well-informed public health decisions and policies. Understanding these interactions on a population scale is essential for developing targeted, evidence-based policies that can efficiently control the spread of both diseases and minimize their societal impact.

Mathematical models have been instrumental in understanding the transmission dynamics of respiratory infectious diseases and evaluating control strategies. Recent literature has

addressed several key aspects of these dynamics, including the variants of concern (VOCs) of SARS-CoV-2 [32, 33, 34, 35] and interaction of respiratory pathogens [36, 37].

1.2 Motivation and Scope of the Thesis

This dissertation addresses some of the necessities that arose during the course of the COVID-19 pandemic. In this thesis, we explored three distinct facets of the transmission dynamics of respiratory virus pathogens, motivated by COVID-19 and influenza and their co-circulation. The selection of these viruses is based on their significant healthcare impact, the existence of protective interventions, and their time relevance to the current and future public health landscape. In particular, the co-circulation models studied in this work are grounded in the early epidemic dynamics of COVID-19, where diagnostic delays and healthcare capacity constraints posed significant challenges to timely interventions and outbreak control.

- In the first part of this study, we examine an early pandemic scenario caused by a novel, rapidly mutating virus that presents significant challenges for disease control. We focus on the transmission dynamics of two co-circulating strains: the original strain and a more transmissible variant, classified as a Variant of Concern (VOC). Mathematical modeling of two-strain infectious diseases is well-established in the literature, with applications to malaria, dengue, influenza [38, 39, 40], and COVID-19 [33, 34, 35, 41]. For recent SARS-CoV-2 VOCs, various studies have examined strain competition, co-infection, and the effects of different interventions [42, 43, 44, 45]. However, no study explicitly considers strain-specific interventions and the impact of testing delays caused by limited resources.

  During the early stages of the pandemic, non-pharmaceutical interventions were used to control the spread of the original strain in the absence of vaccines or treatments. However, the emergence of a more transmissible VOC raised concerns about the effectiveness of

these measures. In such situations, variant-specific control strategies become essential, even when healthcare resources are limited. A key aspect of VOC-specific interventions is the ability to identify and distinguish between different strains, which requires whole genome sequencing (WGS). Whole genome sequencing (WGS) plays a crucial role in identifying and tracking new variants, allowing for better monitoring and response. To address these challenges, we develop a novel mathematical model to evaluate the variant-specific strategies, emphasizing the importance of rapid detection and targeted measures to control VOC-driven outbreaks. Using COVID-19 as a case study, we analyze optimal strategies to prevent or mitigate outbreaks fueled by these emerging variants. This work addresses the limited research on interventions tailored to SARS-CoV-2 variants of concern, filling an important gap in pandemic management strategies.

- In the second part, the study examines the co-circulation of influenza and COVID-19, which, despite no longer being a pandemic, remains a public health concern with periodic outbreaks. Simultaneous waves of these respiratory infections can overload healthcare systems, particularly during flu season. To better understand the dynamics of these two diseases when circulating concurrently, various studies have been developed [46, 47, 48, 49, 48]. In addition, some studies have focused specifically on the dynamics of co-infection with both viruses [50, 51, 52]. The economic burden associated with the co-circulation of these infections has also been explored in [53]. Manuel A et al. in [54] developed a model to study the interaction between SARS-CoV-2 and influenza, considering different scenarios of vaccination. While vaccines are available for both diseases, challenges remain in optimizing vaccine coverage and managing overlapping symptoms. To address this gap, a deterministic mathematical model is formulated that allows for the simulation of the transmission of COVID-19 and influenza simultaneously. Immunization by vaccination is incorporated. By considering varying levels of vaccination coverage, including individuals vaccinated against one

or both viruses, the model identifies optimal strategies for managing these infections concurrently. While some studies have looked into the coexistence of COVID-19 and influenza, addressing coinfection, economic impacts, and vaccination strategies, gaps remain in managing overlapping symptoms and optimizing vaccine coverage, especially with varying COVID-19 vaccine doses. A key focus is on delaying or separating their peaks to minimize the combined burden on healthcare systems.

- Third part enhances classical SIR models by incorporating a time dependent removal rate to account for delays in diagnosis and isolation caused by healthcare resource constraints. The integration of time-dependent removal rates into epidemic models offers a novel perspective on the impact of resource limitations. The removal rate is modeled as a bell shaped function of infected individuals includes a time delay reflecting the lag between infection and isolation. Also, considering a bell shaped function allows for a variable removal rate corresponding to different stages of an epidemic. This model captures the destabilizing effects of strained healthcare systems, including oscillatory dynamics, offering insights to optimize public health strategies and resource management.

This thesis contributes to understanding the complex dynamics of respiratory infectious diseases by exploring mathematical modeling approaches focusing on variant-specific interventions, the cocirculation of SARS-CoV-2 and influenza and incorporating delay models, particularly in the removal rate, to account for the limited availability of healthcare resources. By considering these delays, the model reflects the reality that healthcare systems may not be able to respond instantaneously to rising cases, which can result in fluctuations in infections and the effectiveness of interventions over time. While general public health measures such as contact tracing, isolation, and lockdowns have been widely studied, this research addresses an important gap by analyzing the interactions between SARS-CoV-2 and its VOCs, providing insights into how targeted interventions can improve pandemic control. Moreover, it offers

practical recommendations for managing concurrent epidemics of respiratory diseases through integrated vaccination strategies and optimized resource allocation. The findings gained from this research are not only vital for addressing the pandemic situation but also for preparing future public health responses to similar challenges.

1.3 Author Contributions for the Published and Submitted Papers

Chapters of the thesis are based on the following publications and pre-prints:

Chapter 2:

- Majeed Bushra, Marco Tosato, and Jianhong Wu. Variant-specific interventions to slow down replacement and prevent outbreaks. Mathematical Biosciences 343 (2022): 108703.

  Author contribution: J. W. and B. M. originated the research idea. The model formulation was carried out by B. M. Numerical simulations were performed by B. M. The writing of the manuscript was completed by B. M. after feedback from M. T. and J. W. The project was supervised by J. W.

Chapter 3:

- Majeed, B., David, J.F., Bragazzi, N.L., McCarthy, Z., Grunnill, M.D., Heffernan, J., Wu, J. and Woldegerima, W.A., 2023. Mitigating co-circulation of seasonal influenza and COVID-19 pandemic in the presence of vaccination: A mathematical modeling approach. Frontiers in Public Health,10 (2023): 1086849.

  Author contribution: B.M, W.W, and J.W originated the research idea. The

model formulation was carried out by B.M. Numerical simulations were performed by B.M with the help of J.D and W.W. The writing of the manuscript was completed by B.M, reviewed and edited by J.W, N.B, and W.W. The literature review was done by B.M and N.B. The project was supervised by J.W. All authors provided critical feedback and helped shape the research and analysis.

Chapter 4:

- Majeed Bushra., Denis Fernandes and Wu Jianhong. A Mathematical Epidemic Model with Delay in the Removal Rate.

Author contribution: B.M, and J.W originated the research idea. The model formulation was carried out by B.M. The analysis was done by B.M. with the help of Denis. Numerical simulations were performed by B.M. The writing of the manuscript was completed by B.M, reviewed and edited by Denis and J.W. The literature review was done by B.M. The project was supervised by J.W.

Chapter 2

Modeling Variant-specific Interventions to Slow Down Replacement and Prevent Outbreaks

2.1 Introduction

Genetic mutations play an important role in the evolution of virus in general, and in the ongoing evolution and emergence of novel Severe Acute Respiratory Syndrome Coronavirus 2 (SARS-CoV-2) variants in particular [55]. These genetic variations can lead to the emergence of new variants with selection of phenotypes increasing viral fitness (replication, transmissibility, immune escape). In this chapter, we consider a novel ongoing infectious disease pandemic caused by a virus with the ability to mutate rapidly and present a significant global health challenge. Our investigation focuses on the transmission dynamics of two strains, the original strain and its mutant with the ability to transmit more rapidly, referred to as a Variant of Concern (VOC). In this study, we use COVID-19 as a case study to assess the optimal approaches to prevent or mitigate a VOC-driven outbreak.

Within the context of the COVID-19 pandemic, we scrutinize a scenario where public health interventions, such as social distancing, testing, quarantine, and isolation, in the absence of vaccines have been implemented to mitigate the outbreak with some success, caused by the wild/original strain in the early pandemic. Subsequently, a more transmissible mutant strain, a VOC emerges, challenging the efficacy of established interventions. In such circumstances, strain-specific interventions are needed in an already strained public health system where there are limited additional resources available for mitigating VOC emergency and establishment. Any VOC-specific intervention relies on the use of a whole genome sequencing (WGS) test to specify the strain.

Genome sequencing methods are used to decode the genes to better understand the virus mutations. Genomic sequencing permits recognition of pathogen, monitoring its evolution over time, and detecting appearance of a new variant [14]. Here, we develop a modeling framework and analysis, in order to quantify the role of variant-specific interventions in preventing replacement and outbreak of the VOC under consideration. Obviously, this design and implementation of variant-specific interventions needs rapid whole genome sequencing (WGS) of confirmed cases, this in turn requires that 1) the total confirmed cases (for both the original or resident lineage and its variant) to be sufficiently small such that the time delay from contact tracing to testing and to case and strain confirmation can be minimized, and 2) the WGS can be performed on majority, if not all, COVID-19 test positive cases.

During a pandemic, non-pharmaceutical interventions (NPI) are used to control outbreaks in the absence of vaccines and treatments. Many countries have indeed used rapid testing, contact tracing, isolation and mandatory quarantining of international travellers as effective tools to keep case counts significantly low. The role of rapid tests to enhance contact tracing and quarantine/isolation for controlling past outbreaks has been modeled and analyzed [56, 57, 58, 59, 60, 61], and other modeling studies have addressed VOC-relevant issues including evaluating the impact of increasing impermissibility and estimating the replacement time [62,

63, 64, 26, 65, 66, 67, 68]. In contrast, we seek to evaluate, under different scenarios of clinical COVID-19 and WGS testing capacity, the impact of the co-circulation of old-lineage and VOC on testing delays, the impact of these delays on contact tracing and quarantine/isolation, and the impact of strain-specific contact tracing and quarantine/isolation measures on the disease spread potential and disease burden. In particular, we seek to answer the question of whether VOC-specific public health investments and interventions can optimize the resources to avoid a new VOC-induced outbreak or, if this outbreak is unavoidable, to mitigate the outbreak.

2.2 Material and Methods

2.2.1 Model formulation

We consider a situation during a viral disease pandemic like the COVID-19 global pandemic, when various public health interventions, such as social distancing, testing, quarantine, and isolation, are implemented to curb the spread of infection. While these measures prove somewhat effective in controlling the outbreak, the introduction of a variant of concern poses new challenges. In this context, we focus on the SARS-CoV-2 virus and its B.1.1.7 (Alpha) variant as a background, although the analysis is applicable to other variants of concern (VOCs) such as B.1.351(Beta), P.1(Gamma), and B.1.617(Delta). This study, conducted during the early stages of the COVID-19 pandemic, examines the impact of these emerging variants and the challenges they pose to ongoing efforts to control the spread of the virus. The introduction of VOCs can lead to higher transmission rates and greater virulence, which may necessitate adjustments in public health strategies and interventions. In our model formulation, we use sub-index r for the original (resident) lineage, and m for the variant of concern being considered. We assume co-circulation of both lineages, i.e, one lineage is not replaced by another. For the sake of simplicity, we assume both r-lineage and m-variant

provide complete immunity to the other immediately on infection that will last for the entire period of the outbreak and so no co-infection can happen. Therefore, by a susceptible individual, we mean an individual that who is susceptible to both r-lineage and m-variant, and an individual recovered from infection with one of r-lineage and m-variant is completely immune to both. So, recovered will not return to susceptible class.

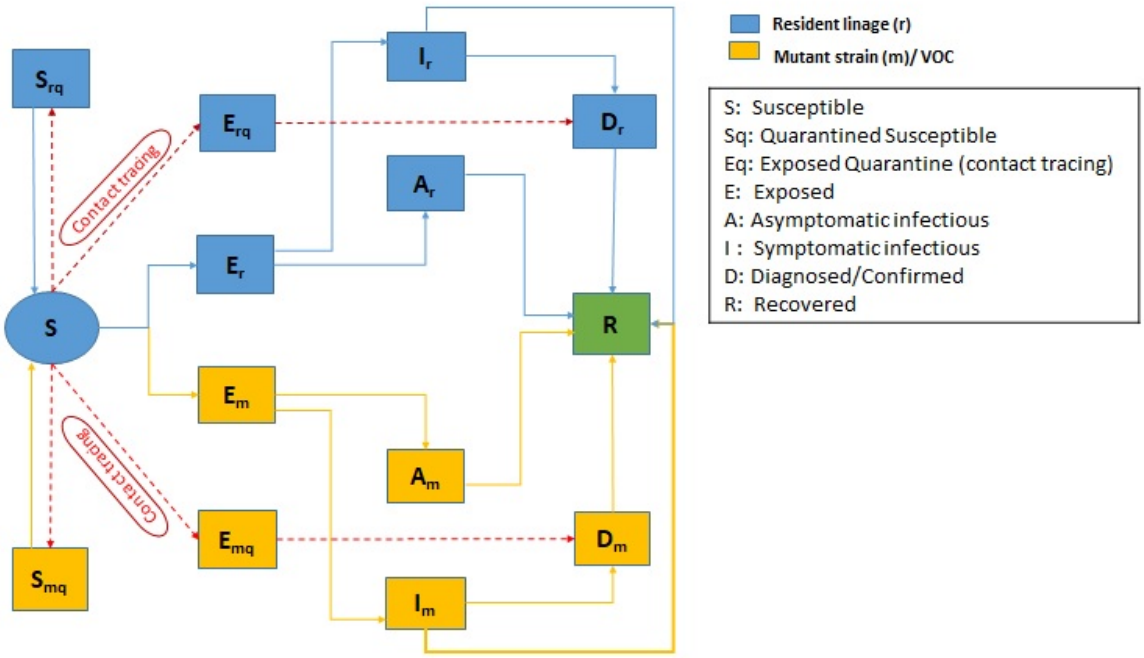

Figure 2.1: The flowchart illustrating the COVID-19 infection dynamics with two strains, original resident strain (r-linage) and mutant strain (m-variant)/VOC. Interventions including intensive contact tracing followed by quarantine and isolation are indicated.

In our formulation, we stratify the population into 14 mutually exclusive compartments (Figure 1) based on the epidemiological status of the individuals and the control interventions: susceptible (S), exposed with the r-lineage and its variant ($i = r, m$), (E_i), asymptomatic infectious (A_i), infectious with symptoms (I_i), diagnosed and isolated (D_i), isolated susceptible (S_{qi}), isolated exposed under contact tracing (E_{qi}) and recovered (R). Following the basic model structure developed by the LIAM group [69], we also consider contact tracing, where a

proportion, q, of individuals exposed to the virus are traced and isolated. The quarantined individuals can either move to the compartment E_{qi} or S_{qi}, depending on whether the transmission has occurred (with probability β_i if the contact is with someone that has strain i), while the other proportion, $1-q$, consists of individuals exposed to the virus who are escaped from contact tracing and, therefore, move to the exposed compartment E_i once infected, or stay in the compartment S otherwise. Here, we adopt the standard public health definitions of quarantine and isolation to describe these compartments clearly. Quarantine refers to separating individuals who may have been exposed to the infection but are not yet confirmed to be infected, as represented by the compartments S_{qi} and E_{qi} in our model. These individuals are quarantined by contact tracing as a precautionary measure. In contrast, isolation refers to separating individuals who are known to be infectious through confirmed testing, as represented by the compartment D_i. We distinguish between prediagnosis measures (quarantine) and post-diagnosis measures (isolation), which reflect standard public health practices during epidemics like COVID-19.

We assume that resident lineage and m-variant have different transmission probabilities and the VOC is more transmissible, i.e. $\beta_m > \beta_r$ with $\beta_m = \kappa\beta_r$, hence $\kappa > 1$.

Unlike the early model formulation, here we assume the testing (both COVID-19 testing to confirm cases and WGS testing for VOC) capacity is limited, and the quarantine proportion of traced contacts of cases confirmed by the testing is negatively proportional to the total number of individuals being tested. We describe this by the classical Holling-type II saturated function. In particular, let B be the total number of people needed to be tested. These include exposed individuals who have been traced, and those who are symptomatically infected (and have escaped from contact tracing when they were in their incubation period). That is,

$$B = E_{rq} + E_{mq} + I_r + I_m.$$

In what follows, we also write $I = I_r + I_m$ and $E_q = E_{rq} + E_{mq}$. Let w be the constant such

that $1/w$ is the maximum number of people who can be tested per day(testing capacity per day). Let

$$H(B) = \frac{1}{1+wB}.$$

Then H is a decreasing function, with $H(0) = 1$ and $H(\infty) = 0$. We use δ_I and δ_q to denote the fastest rate to diagnostically confirm a symptomatically infectious and a traced exposed individual, respectively. Then the practical rate to diagnostically confirm a symptomatically infectious and a traced exposed individual, is respectively given by $\delta_I H(B)$ and $\delta_q H(B)$, and the larger the B, the smaller the diagnostic confirmation rate. Therefore, the total number of individuals to be practically tested per day is given by the Holling-type II like function $(\delta_I I + \delta_q E_q)H(B)$. This, like the normal predator-prey model, assumes that processing of testing and searching for candidates to be tested are mutually exclusive behaviors. In this analogue, w is also the test processing time per individual. We mention that this formulation is similar to that in the Monod equation for the growth of microorganisms and that in the Michaelis–Menten equation for the rate of enzymatic reactions.

In what follows, we let

$$F_1(I, E_q) = \frac{\delta_I I}{1 + w(I + E_q)},$$

$$F_2(I, E_q) = \frac{\delta_q E_q}{1 + w(I + E_q)},$$

or, in terms of E_{rq},E_{mq}, I_r, and I_q, separately, we have

$$F_{rI}(I_r, I_m, E_{rq}, E_{mq}) = \frac{\delta_{Ir} I_r}{1 + w(I_r + I_m + E_{rq} + E_{mq})},$$

$$F_{mI}(I_r, I_m, E_{rq}, E_{mq}) = \frac{\delta_{Im} I_m}{1 + w(I_r + I_m + E_{rq} + E_{mq})},$$

$$F_{rE}(I_r, I_m, E_{rq}, E_{mq}) = \frac{\delta_{rq} E_{rq}}{1 + w(I_r + I_m + E_{rq} + E_{mq})},$$

$$F_{mE}(I_r, I_m, E_{rq}, E_{mq}) = \frac{\delta_{mq} E_{mq}}{1 + w(I_r + I_m + E_{rq} + E_{mq})}.$$

These functions characterise the saturation phenomenon of limited testing resources. All of the above saturated functions are C^1-smooth, and each reaches its peak or maximum at ∞, that is,

$$\lim_{I_i \to \infty} F_{iI} = \frac{\delta_{Ii}}{w},$$

and

$$\lim_{E_{iq} \to \infty} F_{iE} = \frac{\delta_{iq}}{w}.$$

Since tracing happens as a consequence of testing with some delay, we can define the quarantine fraction q_r and q_m for both r-lineage and m-variant respectively as

$$q_r = q_{r0}(\tau_1) H(B(t - \tau_1)), \tag{2.1}$$

$$q_m = q_r + (1 - q_r) q_{m0}(\tau_2) H(B(t - \tau_2)). \tag{2.2}$$

In this formulation, we have

$$q_{r0}(\tau_1) = \begin{cases} q_{r0}\left(\frac{L - \tau_1}{L}\right), & \text{if } \tau_1 < L, \\ 0 & \text{otherwise,} \end{cases}$$

and similarly,

$$q_{m0}(\tau_2) = \begin{cases} q_{m0}\left(\frac{L - \tau_2}{L}\right), & \text{if } \tau_2 < L, \\ 0 & \text{otherwise.} \end{cases}$$

Here L represents the incubation period, and τ_1 and τ_2 are testing delays in clinical COVID-19 test and WGS test respectively. This formulation reflects the fact that the

quarantine proportion decreases linearly as a function of the testing delay, and quarantine proportion becomes zero when the testing delay exceeds the incubation period. Here q_{r0} and q_{m0} represent the maximum quarantine fractions of confirmed COVID-19 tests and of mutants/VOC after WGS tests respectively. Because of similar symptoms, simple COVID-19 clinical diagnostic test can only confirm the infection but cannot identify m-variant from r-lineage. So, the contacts traced for both strains would be quarantined at the same rate, that's why q_r is added in equation (2.2). In addition, in equation (2.2), we model the quarantine rate of mutant strain if additional WGS test confirms the m-variant and extra efforts to trace and quarantine those exposed to the m-variant.

The constant delay τ_1 in equation (2.1) represents the time lag between COVID-19 confirmation of an index case and successful tracing and quarantine/isolation of its exposed contacts. Since WGS test is required to identify VOC type and this test often requires sending samples to a central lab for sequencing, there will be additional time lag between the WGS identification and this delay is denoted by $\tau_2 - \tau_1$. Therefore, any additional intervention to enhance the contact tracing and quarantine of m-variant will be implemented with the delay $\tau_2 = \tau_1 + (\tau_2 - \tau_1)$, hence the delay τ_2 in the second term of equation (2.2).

In practice, the capacity for WGS only allows for WGS testing for a small portion of COVID-19 diagnosed cases. Assuming these are randomly drawn, then the quarantine rate for m-variant cases must be modified as

$$q_m = q_r + (1 - q_r) q_{m0}(\tau_2) H_g(B(t - \tau_2)), \tag{2.3}$$

with

$$H_g = \frac{1}{1 + w_g B}.$$

Here, $1/w_g = p(1/w)$ is the maximum WGS testing capacity per day, p is the proportion of clinically COVID-19 confirmed cases further tested for genetic sequence, and B is the total number of infected to be tested.

Under all these assumptions and incorporating saturated diagnostic functions, we end up with the following dynamical system of nonlinear equations:

$$
\begin{aligned}
S' &= \sum_{i=r,m} \left[- \left((\beta_i c + c q_i (1-\beta_i)) S \frac{(I_i + \theta A_i)}{N} + \lambda S_{iq} \right) \right] \\
E_i' &= \beta_i c (1-q_i) S \frac{(I_i + \theta A_i)}{N} - \sigma E_i \\
E_{iq}' &= \beta_i c q_i S \frac{(I_i + \theta A_i)}{N} - F_{iE}(I_r, I_m, E_{rq}, E_{mq}) \\
S_{iq}' &= (1-\beta_i) c q_i S \frac{(I_i + \theta A_i)}{N} - \lambda S_{iq} \\
A_i' &= \sigma(1-\rho) E_i - \gamma_A A_i \\
I_i' &= \sigma \rho E_i - F_{iI}(I_r, I_m, E_{rq}, E_{mq}) - (\alpha + \gamma_I) I_i \\
D_i' &= F_{iI}(I_r, I_m, E_{rq}, E_{mq}) + F_{iE}(I_r, I_m, E_{rq}, E_{mq}) - (\alpha + \gamma_D) D_i \\
R' &= \sum_{i=r,m} (\gamma_I I_i + \gamma_A A_i + \gamma_D D_i)
\end{aligned}
\tag{2.4}
$$

2.2.2 Basic reproduction number

In this section, we look at the basic reproduction number R_0, a centerpiece parameter in infectious disease dynamics (the average number of new infections per infected individual during its infectious period in a 'naive' population without any public health interventions). Typically, if the value of the reproduction number is greater than 1, disease would persist in a population and continue to spread, and if it is less than 1, the epidemics would decline gradually and eventually die out. The basic reproduction number is influenced by several factors, such as the transmission rate, the duration of infectiousness, the virulence of the pathogen, and the contact rate within the population. Understanding this number is crucial for forecasting and managing the spread of an outbreak. When control measures or interventions are applied during an epidemic, the reproduction number is referred to as the control/effective reproduction number, denoted as R_{c0}.

The basic reproduction number of this two strain transmission model with control

interventions such as contact tracing and isolation, the R_{c0} control/effective reproduction number, is given by

$$R_{c0} = \max(R_{r0}, R_{m0}).$$

Several methods have been developed to calculate an analytical expression for reproduction number. Here, we use the next-generation matrix approach shown by Diekmann et al. and Van den Driessche et al [70]. The authors provide a comprehensive explanation of how to use the next-generation matrix method to calculate R_0 in compartmental models.

So, following the next generation method, to find the expression for the effective reproduction number for our epidemic model when contact tracing and isolation are used. The computation is done by linearizing the system around the disease-free steady state.

$$\frac{dx_i}{dt} = \mathcal{F}(x, y) - \mathcal{V}(x, y), \tag{2.5}$$

where x_i represents the disease compartments. $\mathcal{F}$ operator represents the rate secondary infections increase(gain) the ith disease compartments. $\mathcal{V}$ denotes the rate progression, death recovery, etc, decrease (loss) in the ith compartment.

At the disease-free equilibrium no infections exist, so all infected compartments must be zero i.e., disease free equilibrium point for both strains has E_i, E_{qi}, A_i, I_i equal to zero. The resulting four dimensional linearized system we have $x' = (F - V)x$, where $x = \begin{pmatrix} E_i & E_{qi} & A_i & I_i \end{pmatrix}^T$, $F = \frac{\partial \mathcal{F}}{\partial x}$ and $V = \frac{\partial \mathcal{V}}{\partial x}$.

From our model

$$\mathcal{F} = \begin{pmatrix} \beta_i c(1 - q_i) S \frac{(I_i + \theta A_i)}{N} \\ \beta_i c q_i S \frac{(I_i + \theta A_i)}{N} \\ 0 \\ 0 \end{pmatrix}, \mathcal{V} = \begin{pmatrix} \sigma E_i \\ F_{iE} \\ -\sigma(1 - \rho)E_i + \gamma_A A_i \\ -\sigma\rho E_i + F_{iI} + (\alpha + \gamma_I) I_i \end{pmatrix}$$

Thus we get, at disease free equilibrium with $S \approx N$

$$F = \begin{pmatrix} 0 & 0 & \beta_i c\theta(1-q_i) & \beta_i c(1-q_i) \\ 0 & 0 & \beta_i c\theta(q_i) & \beta_i c(q_i) \\ 0 & 0 & 0 & 0 \\ 0 & 0 & 0 & 0 \end{pmatrix}$$

$$V = \begin{pmatrix} \sigma & 0 & 0 & 0 \\ 0 & \delta_q & 0 & 0 \\ -\sigma(1-\rho) & 0 & \gamma_A & 0 \\ -\sigma\rho & 0 & 0 & \delta_I + \alpha + \gamma_I \end{pmatrix}$$

The effective reproduction number is the largest eigenvalue of the matrix FV^{-1}.

Hence, using the standard next generation matrix approach [70, 71] applied to the case when delays, τ_1, τ_2 equal to zero in equations (2.1) and (2.2), we get the following control reproduction number for both r-lineage and m-variant respectively as

$$R_{r0} = \frac{\beta_r c\rho(1-q_{r0})}{\delta_I + \alpha + \gamma_I} + \frac{\beta_r c\theta(1-\rho)(1-q_{r0})}{\gamma_A}, \tag{2.6}$$

and

$$R_{m0} = \frac{\beta_m \rho c(1-q_{r0})(1-q_{m0})}{\delta_I + \alpha + \gamma_I} + \frac{\beta_m c\theta(1-\rho)(1-q_{r0})(1-q_{m0})}{\gamma_A}. \tag{2.7}$$

In particular, R_{m0} can be written in terms of R_{r0} as

$$R_{m0} = \kappa(1-q_{m0})R_{r0}, \tag{2.8}$$

where $\kappa = \frac{\beta_m}{\beta_r}$, $(\kappa > 1)$ is the ratio of the transmission probability (the relative infectivity)

of m-strain over the r-lineage. In equation (2.8), $1 - q_{m0}$ represents the effect of a contact tracing strategy targeted to VOC to reduce the number of secondary infections of mutant strain in the community/population.

Lemma 2.2.1: The following results hold for R_{r0} and R_{m0}:

(i) $R_{r0} = R_{m0} \iff q_{m0} = 1 - \frac{1}{\kappa}$;

(ii) If $R_{r0} < \frac{1}{\kappa}$, then $R_{m0} < 1$;

(iii) If $R_{r0} \geq \frac{1}{\kappa}$, then $R_{m0} < 1 \iff q_{m0} > 1 - \frac{1}{\kappa R_{r0}}$.

Proof: Using Eq. (2.8) to replace R_{m0} in $R_{r0} = R_{m0}$, it derives that $q_{m0} = 1 - \frac{1}{\kappa}$. Let $R_{r0} > \frac{1}{k}$, we analyze when $R_{m0} < 1$. Using Eq. (2.8), we have

$$\kappa(1 - q_{m0})R_{r0} < 1.$$

By isolating q_{m0}, we get

$$q_{m0} > 1 - \frac{1}{\kappa R_{r0}}. \tag{2.9}$$

Note that $0 \leq q_{m0} \leq 1$, since it is a fraction. If $R_{r0} < \frac{1}{k}$, (2.9) always holds therefore $R_{m0} < 1$. If $R_{r0} \geq \frac{1}{k}$, then (2.9) has to hold in order for $R_{m0} < 1$.

Further Eq. 2.8 with $\kappa > 1$ and $q_{m0} \in (0, 1)$ implies that there are four generic possibilities.

(I) $R_{r0} < 1$

(a) $R_{m0} < 1$ for all quarantine choices if $R_{r0} < 1/\kappa$ (i.e. if basic reproduction number for resident strain is very small) guarantees that both strains die out.

(b) $R_{m0} > 1$ if $R_{r0} > 1/\kappa$ and $q_{m0} < 1 - \frac{1}{\kappa R_{r0}}$ (i.e. if quarantine rate is too small and basic reproduction number for resident strain is larger than the threshold $\frac{1}{\kappa}$) would lead to persistence of a mutant strain and extinction of the resident strain.

(II) $R_{r0} > 1$

(c) $R_{m0} < 1$ if $q_{m0} > 1 - \frac{1}{\kappa R_{r0}}$ (i.e. if quarantine rate for mutant strain is large enough) would lead to the resident strain becoming prevalent.
(d) $R_{m0} > 1$ if $q_{m0} < 1 - \frac{1}{\kappa R_{r0}}$ (i.e. if quarantine rate for mutant strain is smaller than a threshold) would guarantee coexistence of the strains.

Furthermore, we need to address two key points here:

- The structure of our model does not require $\kappa > 1$. The compartmental framework, saturation dynamics for testing delays, and strain-specific interventions can still accurately capture transmission dynamics when the mutant strain is weaker, i.e., when $\kappa < 1$.

- However, lemma 2.2.1 relies critically on the assumption $\kappa > 1$, and conditions established for outbreak prevention, strain replacement, and coexistence become inapplicable when $\kappa < 1$.

  In fact, the lemma's statement (iii) would lead to incorrect conditions when $\kappa < 1$ (e.g., requiring q_{m0} to be negative (negative quarantine fractions). This is impossible. So, for $\kappa < 1$, new analysis will be required.

2.2.3 Parameters

We have used some data from the Province of Ontario, Canada as a case study for our model simulations. We start with the assumption that resident lineage is under control, i.e. its reproduction number is less than 1. We fix the following parameters: the probability of transmission of resident lineage $\beta_r = 0.1446$, contact rate $c = 5.78$ and the fastest diagnostic rate $\delta_I = 0.333$, such that the value of R_{r0} stays less than 1, for any quarantine rate q_r less than 0.3. We assume that these parameter values do not change over the simulations we conduct with the introduction of the VOC. We consider the incubation period as 5 days (mean 5–6 days, range 1–14 days)[72] for both resident and VOC. Even though relative transmissibility of VOCs ranges from 140% to 160% [65, 66], we use the conservative assumption that

$\beta_m = 1.4\beta_r$, which represents a 40% increase in transmission of m-strain compared to resident lineage. All other parameters are taken from [69], given in Table 3.1 and we assume that the relevant parameters, except the transmission probability per contact, are the same for the r-lineage and m-strain. We note that it takes usually 2-3 days from sampling to the return of results, so, our assumed fastest diagnose rate of symptomatic infected individuals seems plausible.

We consider the initial values of model variables for r-lineage as estimated in [69] according to the data from the end of December 2020. We assume that when the first few cases of mutant strain were diagnosed in Ontario, resident lineage was predominant and the initial frequency of the VOC was very low (about 0.1%) relative to the r-lineage. So, initial values for m-strain variables are chosen accordingly. Furthermore, we assume that the resources allow for a maximum 40% - 70% of tracing coverage (proportion of contacts that are successfully traced and isolated) after the clinical COVID-19 test.

Table 2.1: Model variables and their initial values

Variable List			
Variable	Definition	Initial Value	Source
S	Number of individuals susceptible to both diseases	1.42033×10^7	Data
S_{rq}	Quarantined susceptible population with resident lineage	0.01617×10^7	[69]
S_{mq}	Quarantined susceptible population with mutant strain	0	chosen
E_{rq}	Quarantined exposed population with resident lineage	0.00123322×10^7	[69]
E_{mq}	Quarantined exposed population with mutant strain	2	chosen
E_r	Exposed population with resident lineage.	0.001177×10^7	[69]
E_m	Exposed population with mutant strain	10	chosen
A_r	Asymptomatic infectious with resident lineage	0.0004497×10^7	[69]
A_m	Asymptomatic infectious with mutant strain	0	chosen
I_r	Symptomatic infectious with resident lineage	0.000543029×10^7	[69]
I_m	Symptomatic infectious with mutant strain	5	chosen
D_r	Diagnosed isolated with resident lineage	0.0010226×10^7	[69]
D_m	Diagnosed isolated with mutant strain	2	chosen
R	Recovered from both strains	0.02905217×10^7	[69]

Table 2.2: Parameters, definitions and values

Parameter List			
Parameter	Definition	Value	Source
β_r	Probability of transmission of resident lineage	0.1446	[69]
β_m	Probability of transmission of mutant strain	$1.4\times\ \beta_r$	chosen [65, 66]
c	Contact rate	5.78	chosen
σ	Transition rate of exposed individuals to infected class	1/5	[72]
λ	Rate at which quarantine uninfected released to community	1/14	[69, 73]
ρ	Probability of having symptoms from exposed class	0.724	[69]
α	Disease-induced death rate	0.008	[69]
γ_I	Recovery rate of symptomatic infected from both strains	0.1627	
γ_A	Recovery rate of asymptomatic infected from both strains	0.134	[69]
γ_D	Recovery rate of diagnosed isolated individuals	0.2	[69]
θ	Modification factor of asymptomatic infectiousness	0.0342	[69]
q_{r0}	Maximum quarantine fraction of resident lineage	vary	chosen
q_{m0}	Maximum quarantine fraction of mutant strain	vary	chosen
$\frac{1}{\omega}$	Maximum capacity of testing per day	vary	
δ_{rI}	Fastest diagnose rate of symptomatic infected resident lineage	0.333	chosen
δ_{mI}	Fastest diagnose rate of symptomatic infected mutant strain	0.333	chosen
δ_{rq}	Fastest diagnose rate of exposed individuals resident lineage	0.1237	[69]
δ_{mq}	Fastest diagnose rate of exposed to mutant strain	0.1237	[69]
p	Fraction of diagnosed cases further tested for WGS test	vary	chosen

2.2.4 When and how VOC-specific intervention is needed?

In this subsection, we conduct some numerical experiments to see when and how VOC-specific interventions such as additional quarantine and rapid WGS testing are needed.

2.2.4.1 Reproduction number: full control

The control reproduction number of the VOC with higher transmissibility plays a dominating role to determine whether a VOC-induced outbreak can be prevented with the interventions, primarily contact tracking and quarantine/isolation. Note that if the control reproduction number of the r-lineage $R_{r0} \geq 1$ or slightly below one, then R_{m0} will surely exceed the unity, so our focus is on conditions for the quarantine fractions of r-lineage and m-variant such that $R_{m0} < 1$.

Figure 2.2 shows the linear relationship between R_{m0} and q_{m0} when q_{r0} is fixed, where each colored straight line corresponds to a fixed quarantine fraction for the traced exposed individuals. In this case, there is a threshold value of q_{m0} at which $R_{m0} = R_{r0}$, and this is given by the dotted vertical line. We use the horizontal line to represent the threshold $R_{m0} = 1$ so the intersection of the colored line with the horizontal line gives the minimal additional quarantine fraction for the exposed to the VOC in order to avoid the VOC-induced outbreak. For example, with a $q_{r0} = 0.3$ quarantine fraction for all exposed traced, we need an additional $q_{m0} = 0.2$ quarantine fraction of all those exposed to VOC in order to avoid an outbreak; however increasing $q_{r0} = 0.4$ will reduce the need of q_{m0} to about 0.05.

Figure 2.3 gives isoclines of the control reproduction number R_{m0} as R_{r0} and q_{m0} vary. In particular, if R_{r0} is kept less than $\frac{1}{\kappa} \approx 0.7142$(under our parameter assumptions), variant-specific contact tracing and additional quarantine would not be necessary. In other words, to control the epidemic and to slow disease progression without any strain-specific interventions, a goal is to ensure that $R_{r0} \leq \frac{1}{\kappa}$. In case this cannot be achieved, intensive contact tracing of VOC cases after WGS testing will be required, following the theoretical result in Lemma

2.2.1.

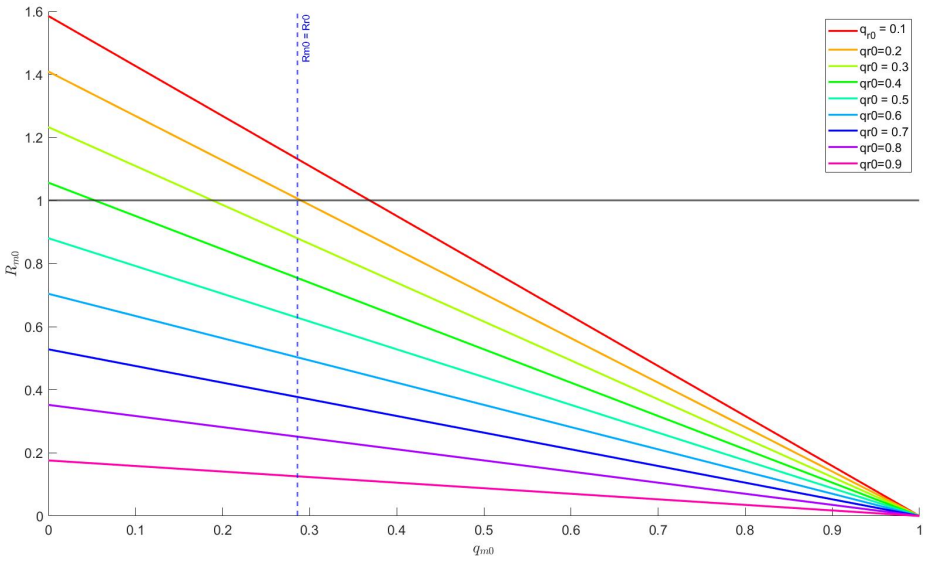

Figure 2.2: Plot of R_{m0} as a function of q_{m0}. There is a linear relationship between reproduction number R_{m0} and strain-specific quarantine fraction q_{m0} when q_{r0} is fixed. Here the vertical dotted line represents the value of $q_{m0} \approx 0.2857$ at which $R_{m0} = R_{r0}$ and horizontal line represents threshold value of $R_{m0} = 1$.

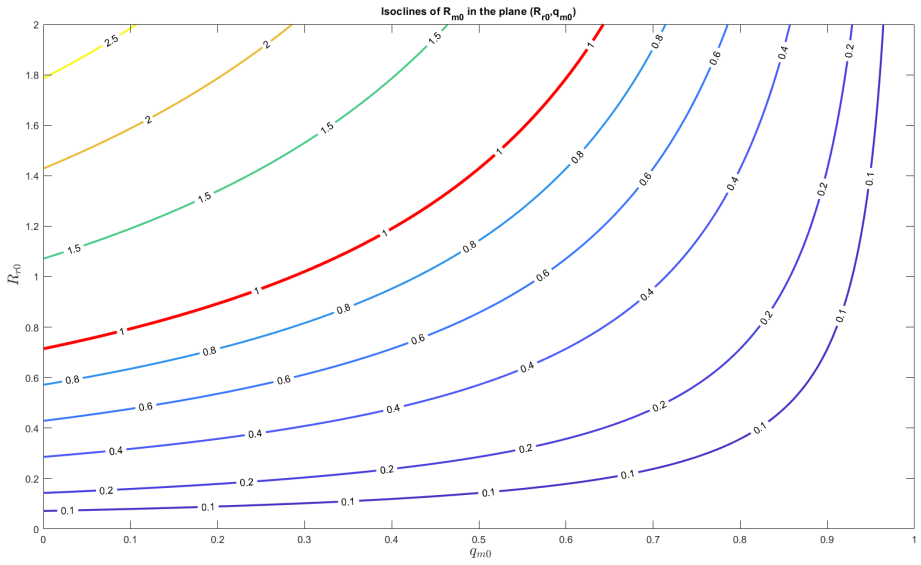

Figure 2.3: Isoclines of effective reproduction number R_{m0} of m-vstrain/VOC, in plane (R_{r0}, q_{m0}), where red line represents $R_{m0} = 1$.

2.2.4.2 Impact of testing capacity and delays

We now examine the impact of testing capacity w and test-tracing-quarantine delays τ_1 and τ_2 on disease prevalence when COVID-19 clinically confirmed cases are receiving further WGS testing.

For the simulations reported below, we vary the maximum testing capacity per day from 30,000 to 70,000 and take different combinations of both delays (1, 3), (1, 4), (2, 3) and (2, 4). We consider an ideal situation in which resources allow for a maximum of 80% successful contact tracing, with baseline scenario where $q_{r0} = 40\%$, $q_{m0} = 40\%$. We assume that the initial cases with VOC are $I_{m0} = 5$, which are relatively small compared with the cases I_{r0} of predominant resident lineage. We run our simulations for a period of 500 days.

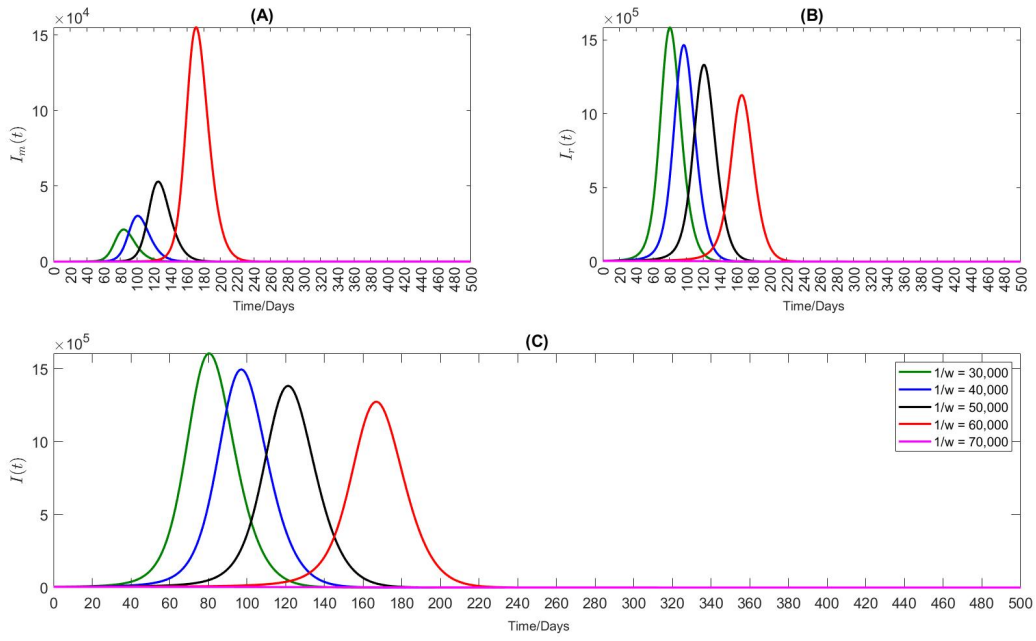

Figure 2.4: The impact of varying the maximum capacity on disease prevalence with delays $(\tau_1, \tau_2) = (1, 3)$ and quarantine fraction $(q_{r0}, q_{m0}) = (0.4, 0.4)$. Plots (A) and (B) represent number of infections with m-strain $(I_m(t))$ and r-lineage $(I_r(t))$ respectively, plot (C) shows total number of infections $I(t) = I_m(t) + I_r(t)$.

Figure 2.4 highlights the impact of varying the maximum testing capacity per day when

delays are $(\tau_1, \tau_2) = (1, 3)$. We observe that by increasing the testing capacity from 30,000 to 60,000, the peak time for the r-lineage outbreak (plot (B)) is postponed and peak value is reduced. The peak time for the m-strain is also postponed, however, against the intuition, the peak number of infections with m-strain increases (plot (A)). This is because the r-lineage is dominant at the beginning of the outbreak, with much higher number of initial infections as compared to the m-strain; so if more testing is done per day more cases of r-lineage are diagnosed and isolated. As a result, it speeds up the frequency of the m-strain and speeds up the transmission of m-strain. However, for the total number of infections (with either r-lineage and m-strain), the large the testing capacity, the later the outbreak peak and the smaller the peak value (plot (C)). The peak time is delayed by 100 days and the number of infections at the peak time is reduced by more than 20% from 30,000 to 60,000 of testing capacity. Figure 2.5 shows the significance of large testing capacity. It shows that the outcome

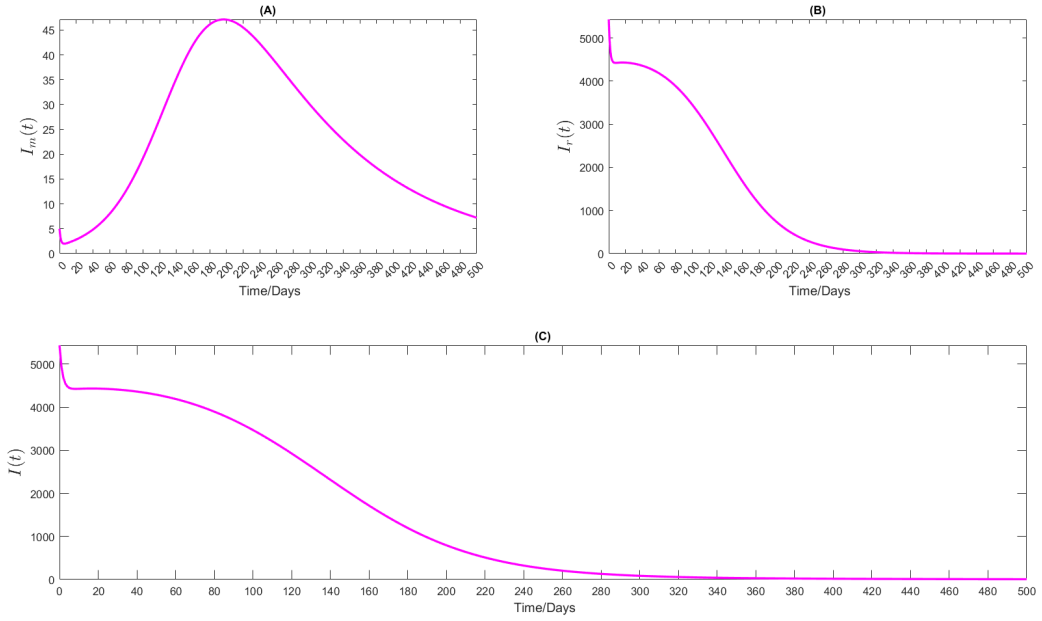

Figure 2.5: This plot shows with high resolution the case in Figure 2.4 with the maximum capacity 70000. Note that the scale of the infections in this plot is several orders of magnitude smaller than Figure 2.4.

with the testing capacity increased 70%, with $(\tau_1, \tau_2) = (1, 3)$. In this case, an outbreak by r-lineage is completely prevented (Plot (B)); while an outbreak by m-strain is not prevented, its outbreak is very small with the only 45 cases at the peak time (Plot (A)). Adding them together, we notice an overall declining trend for the total cases.

Figure 2.6 illustrates the effect of testing capacities on prevalence, by increasing one more day in the WGS test delay $(\tau_1, \tau_2) = (1, 4)$. In this case, for the capacity from 30,000 to 60,000, the epidemic results are similar to that with delay (1, 3) (Figure 2.4).

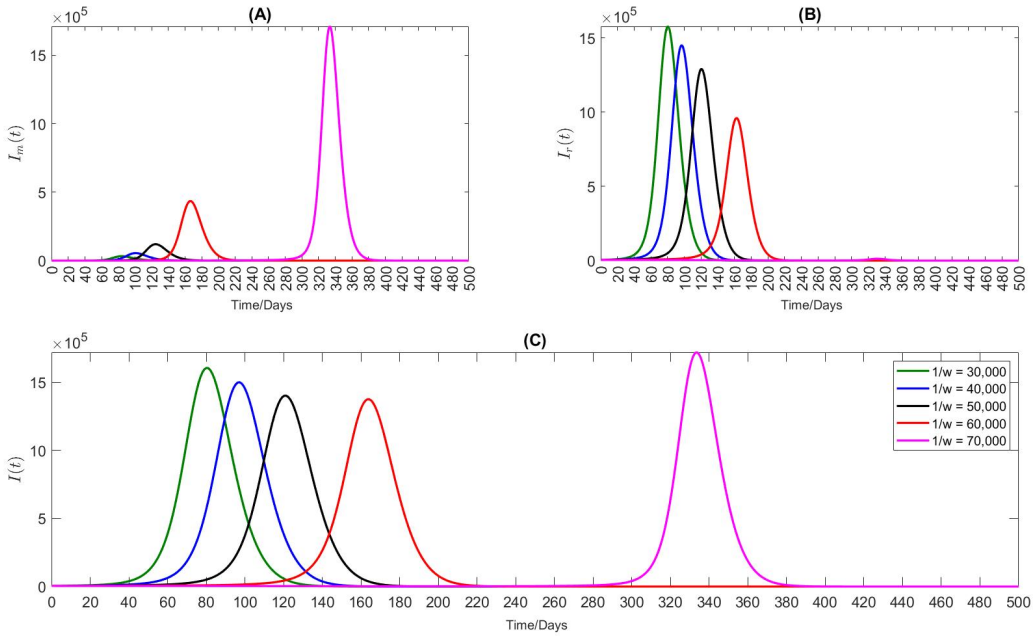

Figure 2.6: The impact of varying the maximum capacity on disease prevalence with delays $(\tau_1, \tau_2) = (1, 4)$ and quarantine fractions $(q_{r0}, q_{m0}) = (0.4, 0.4)$, Plots (A) and (B) represent the numbers of infections with m-strain $(I_m(t))$ and r-lineage $(I_r(t))$ respectively, plot (C) shows the number of total infections $I(t) = I_m(t) + I_r(t)$.

However, with 70,000 testing capacity, the results are dramatically different for mutant strain and the total number of infections. Under this delay structure, infections with m-strain continue to increase slowly and dominate the r-lineage. Figure 2.7 clearly displays this aspect. We can see in plot (A), infections with m-strain rise and in plot (B), infection with r-lineage

declines slowly. It can be noted that overall prevalence (plot (C)) first decreases and then starts to rise quickly after about 210 days, leading to an outbreak. Which shows that in this specific case, m-strain has established and dominates the r-lineage.

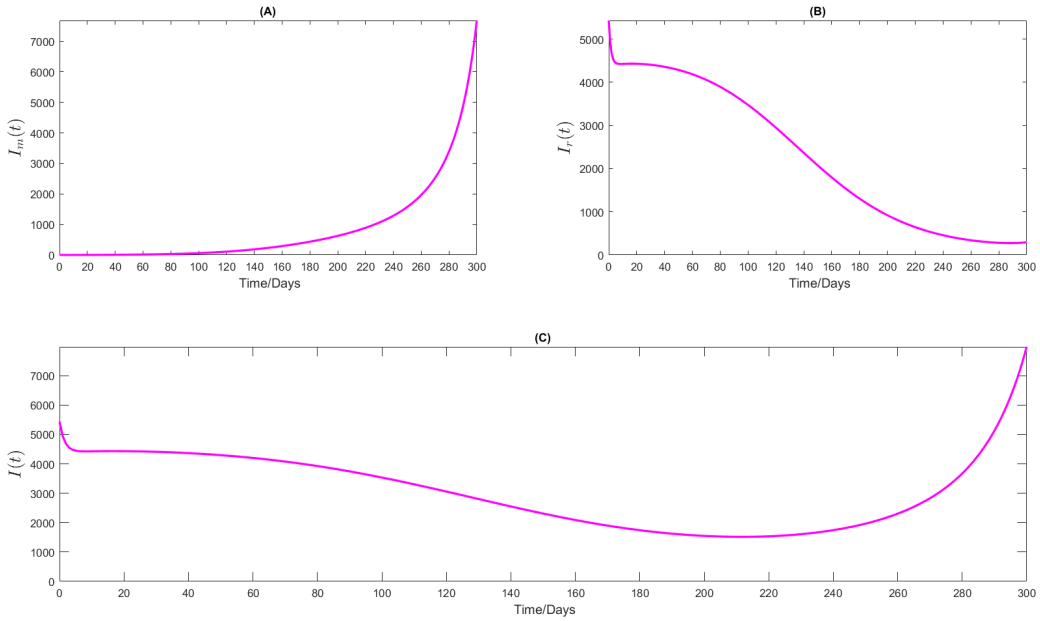

Figure 2.7: This plot shows with high resolution the case in Figure 2.6 with the maximum capacity 70000, where the time scale analysed extends for 300 days. Note that the scale of the infections in this plot is several orders of magnitude smaller than Figure 2.6.

Delay in the WGS testing triggers delay in the strain-specific interventions, specially the tracing and quarantine. We show what happens when τ_2 is increased from 3 days to 4-days in Figure 2.6 plot (A)): not only the peak values of infections increase compared with the situation of $(\tau_1, \tau_2) = (1, 3)$, (Figure 2.4 plot (A)) with the same testing capacity, but more importantly, when the maximum capacity is 70,000 per day, increasing the value of τ_2 by one day significantly changes the outcome from outbreak being avoided to a large m-strain induced outbreak. After the clinical COVID-19 testing, a fraction of contacts is traced and quarantined, but the others (exposed to the m-strain) escaped from the tracing when WGS testing is delayed and contribute to the spread in the population.

To consider the impact of delaying the clinical COVID-19 test for case identification, we consider the situation where $(\tau_1, \tau_2) = (2, 3)$ subject to different levels of testing capacities, and we report the simulations in Figure 2.8. In comparison to Figure 2.4, we notice that with an additional day of delay in clinical testing would lead to a surge in infections even with the testing capacity of 70,000 per day. In addition, the peak time is advanced significantly. For example, with testing capacity of 60,000, the peak time changes from 180 days to 120 days with τ_1 increasing from 1 to 2 days. Therefore, a single day delay in testing can result in peak time shorten by several weeks.

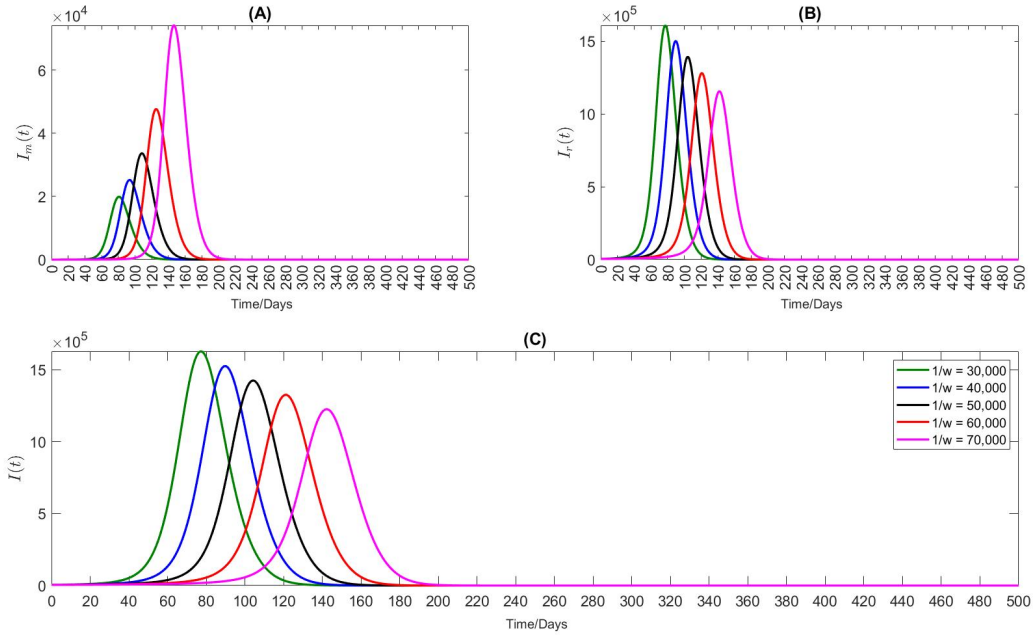

Figure 2.8: The impact of increasing the maximum capacity on disease prevalence with delays $(\tau_1, \tau_2) = (2, 3)$. Plot (A) represents the case where infections with m-strain ($I_m(t)$ are rising and (B) shows the declining trend in the number of infections with r-lineage when we increase the maximum capacity. Plot (C) shows the total number of infections $I(t) = I_m(t) + I_r(t)$ with decreasing trend and peak time delayed.

In summary, we conclude that the final outcome in terms of both r-lineage and m-strain after an introduction of the m-strain depends not only on the maximum testing capacity but

also on both clinical and WGS testing delays and their combination. For example, in the scenarios discussed above, the testing delays (1, 3) coupled with a testing capacity of 70,000 per day avoid a new outbreak despite the initial increase of m-strain infections.

2.2.4.3 Targeted tracing and quarantine efforts

We now consider the issue of optimizing public health resources with designated efforts of increasing the WGS testing and enhancing the tracing and quarantine effort for contacts of the confirmed m-strain cases.

We assume that public health system is able to trace and isolate $40\% - 70\%$ of cases after the clinical COVID-19 test, and we aim to find the minimal amount of additional efforts needed in tracing contacts of m-strain cases after their strains have been confirmed through the WGS testing in order to avoid or mitigate a VOC-induced outbreak.

We have produced extensive simulations for different combinations of testing capacity, testing delays (1, 3),(2, 3), (1, 4) and (2, 4), when the maximum quarantine fractions are in the range $q_{r0} = 40\% - 70\%$ and $q_{m0} = 0\% - 30\%$ to see whether it may or may not prevent an outbreak. First, we have found that if the testing capacity is low (30,000-40,000), we need very strong contact tracing in COVID-19 clinical testing ($q_{r0} = 70\%$), and very stringent additional tracing and quarantine of m-strain cases contacts after their WGS confirmation are required. So, in what follows, we focus on the case where COVID-19 test capacity is between 50,000-70,000. We summarize our simulations in Tables 2.3, 2.4 and 2.5.

With 50,000 testing capacity, as shown in Table 2.3, an outbreak cannot be prevented under any realistic combinations of testing delays, when we consider the parameters in the following range $q_{r0} = 40\% - 50\%$ and $q_{m0} = 0\% - 30\%$. Increasing q_{r0} to 60%, as shown in Figure 2.9, subplots (A) and (B), the outbreak can be prevented if the testing delay is one day. (noting the scale of the cases for two different strains). The simulations also show that given such a short and unrealistic testing delay, additional strain-specific tracing would not make

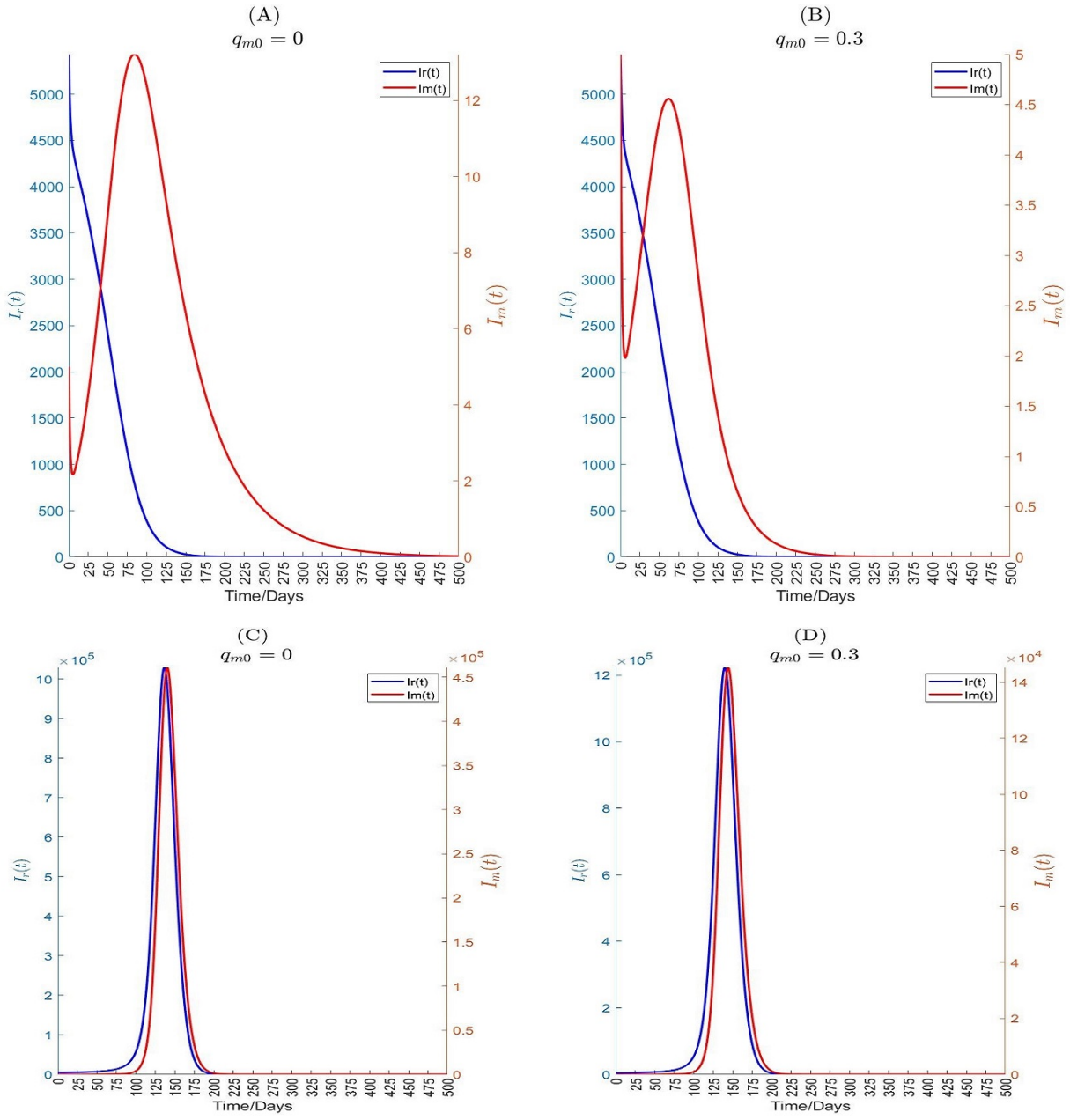

Figure 2.9: The impact of intensive VOC-specific quarantine ($q_{m0} = 0\%, 30\%$) after WGS test on the number of infections $I_m(t)$ with m-strain (red with scale on right side) and $I_r(t)$ with resident lineage (blue with scale on left side). We hold quarantine fraction ($q_{r0} = 0.6$) after clinical COVID-19 test with testing capacity 50,000 per day and testing delays $(\tau_1, \tau_2) = (1, 3)$ in subplots (A), (B) and $(\tau_1, \tau_2) = (2, 3)$ in subplots (C), (D). Note that the scales for r-lineage and for the m-strain are different. With delay (1,3) subplots (A and B) at the peak of a tiny outbreak by m-strain, we have only 6 cases and the r-lineage is under control. While with one day more testing delay $(\tau_1, \tau_2) = (2, 3)$ (subplots C and D) there is an outbreak with both r-lineage and m-strain.

<table>
<tr><th colspan="5">Maximum testing capacity 50,000</th></tr>
<tr><td>Delay/
(q_{r0}, q_{m0})</td><td>(1, 3)</td><td>(2, 3)</td><td>(1, 4)</td><td>(2, 4)</td></tr>
<tr><td>(0.4,0)
(0.4,0.1)
(0.4,0.2)
(0.4,0.3)</td><td colspan="4">Outbreak</td></tr>
<tr><td>(0.5,0)
(0.5,0.1)
(0.5,0.2)
(0.5,0.3)</td><td colspan="4">Outbreak</td></tr>
<tr><td>(0.6,0)
(0.6,0.1)
(0.6,0.2)
(0.6,0.3)</td><td>Under control</td><td>Outbreak</td><td>Under control</td><td>Outbreak</td></tr>
<tr><td rowspan="2">(0.7,0)
(0.7,0.1)
(0.7,0.2)
(0.7,0.3)</td><td rowspan="2">Under control</td><td>Outbreak</td><td rowspan="2">Under control</td><td>Outbreak with VOC</td></tr>
<tr><td>Small outbreak with VOC, Overall controlled</td><td>Small outbreak with VOC, Overall controlled</td></tr>
</table>

Table 2.3: Table summarizes the simulation results for the overall infections (total infections) with m-strain and r-lineage. We consider a fixed maximum 50,000 testing capacity per day and study different combinations of delays (1,3), (2,3), (1,4), (2,4) for COVID-19 clinical tests and WGS testing, and quarantine fractions (q_{r0}, q_{m0}).

much difference. We also note that if the testing delay of COVID-19 is longer than one day, i.e. $(\tau_1, \tau_2) = (2, 3)$, Figure 2.9, subplots (C) and (D), an outbreak will occur involving both the resident lineage and the m-strain . In this case, even an intensive strain-specific tracing and quarantine $q_{m0} = 30\%$ cannot control the epidemic. Finally, $q_{r0} = 70\%$ yields similar results to the case of $q_{r0} = 60\%$ with clinical COVID test delay as one day. However, Figure 2.10 which includes a two days delay (2, 3) in clinical COVID testing shows that epidemic can still be controlled if the VOC-specific quarantine fraction is in the range 10%-30%. In addition, when $q_{m0} = 10\% - 30\%$, VOC cases rise and a small outbreak occurs while resident lineage cases decrease monotonically. If we exclude VOC-specific quarantine, VOC- strain infections rise, resident lineage infections do not monotonically decrease but instead the number of cases starts growing rapidly and then fall a few days later. If we compare Figure 2.10 with Figure 2.9, subplots (C) and (D), we can see that with same delays and testing capacity, outbreaks can be controlled not only by increasing q_{r0} but also by q_{m0}.

We then consider the case with testing capacity of 60,000 and by varying the delays of tests. The results are summarized in Table 2.4.

Similarly to the previous case, there is an outbreak of disease for a 40% quarantine fraction after clinical testing, whatever the choices of q_{m0} and delays. However, in the case

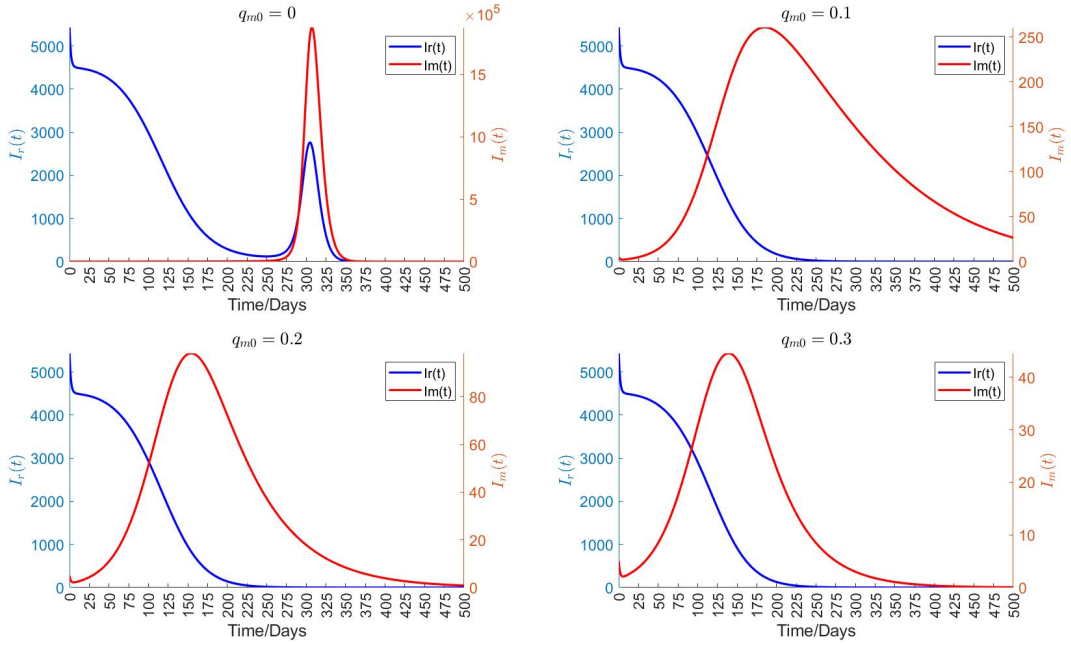

Figure 2.10: The impact of VOC-specific quarantine (q_{m0}) on the number of infections with m-strain and resident lineage. Quarantine fraction ($q_{r0} = 0.7$) after clinical COVID-19 test and testing capacity (50,000 per day). The testing delays are $(\tau_1, \tau_2) = (2, 3)$.

Maximum testing capacity 60,000				
Delay/ (q_{r0}, q_{m0})	(1,3)	(2,3)	(1,4)	(2,4)
(0.4,0) (0.4,0.1) (0.4,0.2) (0.4,0.3)	Outbreak			
(0.5,0) (0.5,0.1) (0.5,0.2) (0.5,0.3)	Slow outbreak with VOC Small outbreak with VOC, Overall controlled	Outbreak	Slow outbreak with VOC Small outbreak with VOC, Overall controlled	Outbreak
(0.6,0) (0.6,0.1) (0.6,0.2) (0.6,0.3)	Under control	Outbreak Small outbreak with VOC, Overall controlled	Under control	Outbreak
(0.7,0) (0.7,0.1) (0.7,0.2) (0.7,0.3)	Under control	Very small outbreak with VOC, Overall controlled	Under control	Very small outbreak with VOC, Overall controlled

Table 2.4: Table summarizes the simulation results of overall infections (total infections) with m-strain and r-lineage. We consider a fixed maximum 60,000 testing capacity per day and study different combinations of delays (1,3), (2,3), (1,4), (2,4) for COVID-19 clinical tests and WGS testing, and quarantine fractions (q_{r0}, q_{m0}).

when quarantine fractions are $(q_{r0}, q_{m0}) = (50\%, 0\% - 30\%)$ and delays (1, 3) or (1,4), we found that there is a declining trend with resident lineage in time and VOC cases rise very slowly without VOC-specific quarantine (i.e. $(q_{m0} = 0)$, and a very small VOC-outbreak with

$q_{m0} = 10\% - 30\%$. So, overall the disease stays under control. We note that with the same testing delays (1, 3) and a 10% increase in the quarantine fraction $q_{r0} = 60\%$, the transmission dynamics is that same as with testing capacity 50,000, and total infection declines and dies out. Similar results are observed with delays (1, 4). However, with an additional testing delay (i.e., (2,3), (2, 4)) and with $q_{r0} = 50\%$, the disease cannot be controlled and there would be an outbreak even we have a high level of additiona VOC-specific quarantine (0% - 30%). Though, with $q_{r0} = 60\%$, as shown in Figure 2.11, infections with r-linage decline and infections with m-strain are significantly slowed down with a small outbreak (total number of infections under control) with 20% or more VOC-specific quarantine fraction.

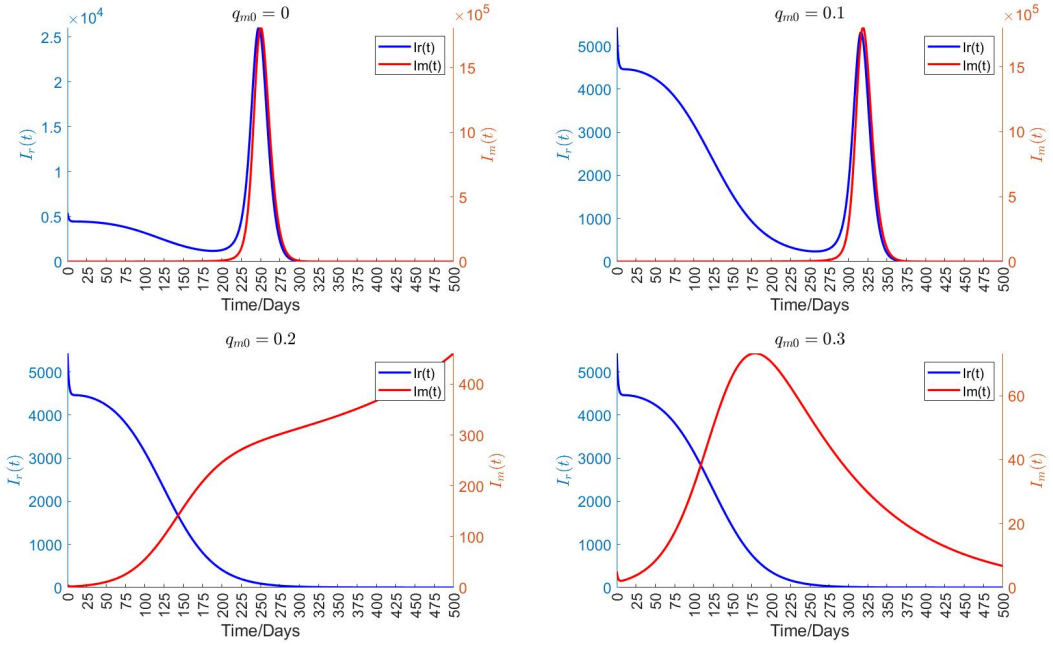

Figure 2.11: The impact of VOC-specific quarantine ($q_{m0} = 0\%, 10\%, 20\%30\%$) on number of infections with m-strain and resident lineage. Quarantine fraction is ($q_{r0} = 0.6$) and testing capacity is 60,000 and the testing delays are $(\tau_1, \tau_2) = (2, 3)$.

But with only 10 % VOC-specific quarantine, resident lineage infections go down first but then start to rise, leading to an outbreak of both r-lineage and m-strain. Therefore, increasing VOC-specific quarantine may help to control not only VOC infections but also

r-lineage infections.

On the other hand, as shown in Figure 2.12 a longer delay in WGS testing (2, 4) leads to an outbreak that cannot be prevented even ($q_{m0} = 30\%$). Recall that if ($q_{r0} = 70\%$), the disease is under control with any combination of delays regardless of VOC-specific quarantine.

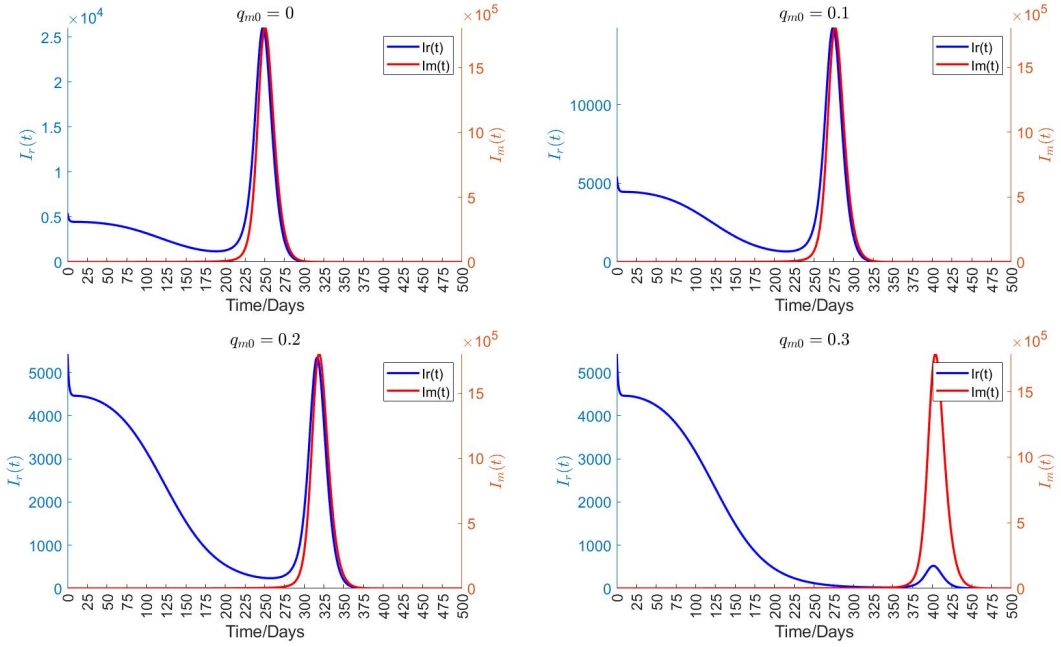

Figure 2.12: The impact of VOC-specific quarantine (q_{m0}) on the numbers of infections with m-strain and resident linage. Quarantine fraction q_{r0} after clinical COVID-19 test and testing capacity are the same as in Figure 2.11. The testing delays are different: $(\tau_1, \tau_2) = (2, 4)$.

Finally, we increase the testing capacity to 70,000, and the results are shown in Table 2.5. In this scenario, most of the results are similar to the 60,000 testing capacity case with $q_{r0} = 40\% - 50\%$ and any test delays. Also, with testing delays (1, 3) and $q_{r0} = 60\%$, the epidemics stays under control without requiring any VOC-specific quarantine. But an additional day delay in clinical COVID-19 testing (2, 3) (see Figure 2.13) leads to a m-strain outbreak and so we see an overall prevalence increases without additional VOC-specific quarantine. However, a small increase of VOC-specific quarantine by 10% eases the situation,

Maximum testing capacity 70,000				
Delay/ (q_{r0}, q_{m0})	(1,3)	(2,3)	(1,4)	(2,4)
(0.4,0) (0.4,0.1) (0.4,0.2) (0.4,0.3)	Outbreak			
(0.5,0) (0.5,0.1) (0.5,0.2) (0.5,0.3)	Slow outbreak with VOC very small outbreak with VOC, Overall under control	Outbreak	Slow outbreak with VOC very small outbreak with VOC, Overall under control	Outbreak
(0.6,0) (0.6,0.1) (0.6,0.2) (0.6,0.3)	Under control	Outbreak with VOC Slow outbreak with VOC Small outbreak with VOC, Overall controlled	Under control	r-lineage under control, Outbreak with VOC
(0.7,0) (0.7,0.1) (0.7,0.2) (0.7,0.3)	Under control	Underll control	Under control	Very small outbreak with VOC, Overall controlled

Table 2.5: Table representing the simulation results of overall infections (total infections) with m-strain and r-lineage. We consider a fixed maximum 70,000 testing capacity per day and study different combinations of delay structures (1,3), (2,3), (1,4), (2,4) for COVID-19 clinical tests and WGS testing for VOC and quarantine fractions (q_{r0}, q_{m0}).

the m-strain infections rise slowly, slowing down the replacement. On the other hand, with an intensive VOC-specific quarantine 20% or 30 %, cases with mutant strain initially rise up but then eventually decrease. Finally, we notice that an additional one day delay in WGS test (2, 4) would produce a VOC outbreak with or without any VOC-specific quarantine measure.

In summary, we infer from our comparative simulations that if the maximum testing capacity maintains to at 60,000-70,000 with minimal delay of one day (delays are then (1,3) and (1,4)) in COVID-19 test, then i). with 50% quarantine the disease can be slowed down or prevented by increasing VOC-specific quarantine; ii). $q_{r0} = 60\%$ can control both strains without any additional VOC-specific quarantine. As delay increases to one more day (2,3) and (2,4) more VOC-specific quarantine would be required to control epidemic.

We also simulated a scenario in which not every positive case receives the WGS testing. Namely, considering different WGS testing capacity, we notice that if less confirmed cases receive the WGS test, VOC-infections and the total infections rise and the peak may arrive earlier. This will create sharp and rapid increase for hospitalization and ICU beds. We presented an illustration in Figure 2.14, where only 5% COVID-19 positive tests receive further WGS test. Comparing Figure 2.14 with Figure 2.4 (when every COVID positive case

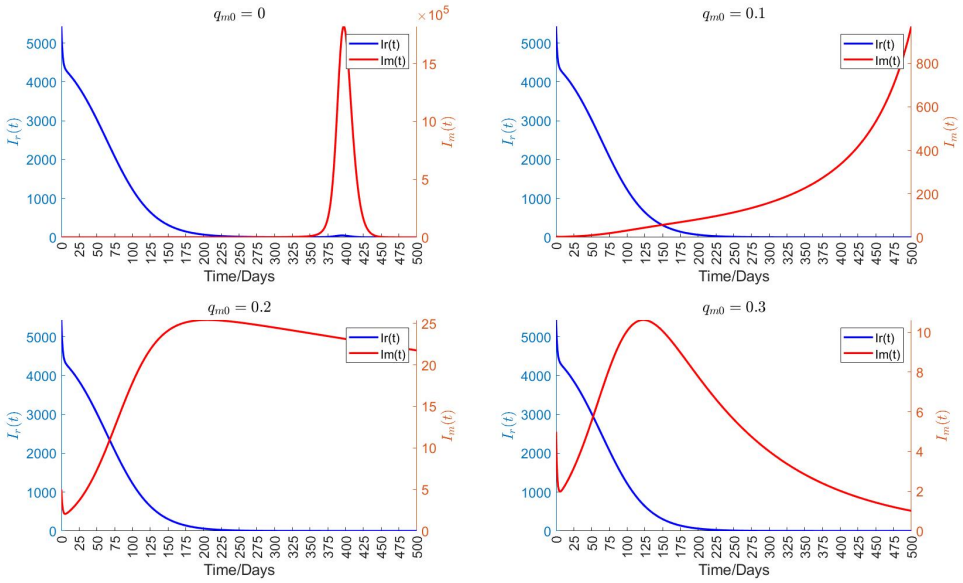

Figure 2.13: The impact of VOC-specific quarantine (q_{m0}) on the number of infections with m-strain and resident lineage. Quarantine fraction is ($q_{r0} = 0.6$) and testing capacity is 70,000 per day. The testing delays are $(\tau_1, \tau_2) = (2, 3)$.

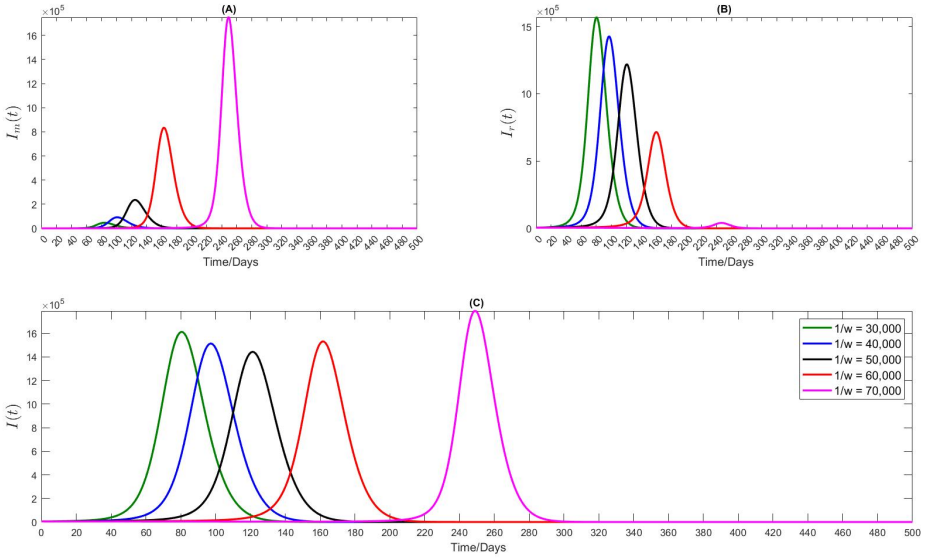

Figure 2.14: The impact of WGS testing capacity on disease prevalence with testing delays $(\tau_1, \tau_2) = (1, 4)$, when only 5 % of confirmed cases receive further WGS testing. Plots (A) and (B) give the numbers of infections with m-strain ($I_m(t)$) and r-lineage ($I_r(t)$) respectively, plot (C) shows the total number of infections $I(t) = I_m(t) + I_r(t)$.

is going through additional WSG test), we observe in the case of 70,000 testing capacity, peak of infections (with only 5% WGS test) can arrive 100 days earlier.

2.3 Discussion

We developed a two strain transmission dynamics model to understand the situation when an existing r-lineage is under control with some social distancing measures including quarantine, but a more transmissible m-strain (VOC) is introduced. We considered the situation where 1) the COVID-19 testing capacity is limited and WGS testing capacity to determine the strain is even more so; 2) each test and each tracing and quarantine of the contacts of confirmed cases takes a certain amount of time, so the more infections to be tested the longer delay for testing triggered contact tracing and quarantine. We use the Holling type saturation function to describe these limitations, and we aim to assess the role of tracing delay and variant-specific intensified quarantine in preventing the replacement and outbreak of an VOC-induced outbreak.

We first showed that the control reproduction number of VOC $R_{m0} < 1$, if the control reproduction number of r-lineage $R_{r0} \leq \frac{1}{\kappa}$ with $\kappa > 1$ being the relative transmissibility of the m-strain over the r-lineage. If this is not possible, a large amount of VOC cases may require to be tracked after WGS test. Our simulation results show that the epidemic growth with VOC depends not only on testing capacity but also on testing delays. In particular, increasing significantly the maximum testing capacity for COVID-19 confirmation and WGS tests can defer the outbreak peak time as well as decrease the peak value, however, lukewarm tracing and quarantine can potentially increase the VOC-cases at the outbreak peak time. We exploited further how regular Covid-19 testing (PCR, antibody and/or antigen) delay increases the chance of an outbreak and the outbreak severity in terms of the total and VOC-cases at the peak time. In addition, we showed that if delay in WGS test cannot be reduced from four days, in the case study of the Province of Ontario, Canada, then the

reduction of COVID-19 clinical test delay to one day and strain-specific quarantine combined is needed and can play a significant role in mitigating the epidemic. Our results supported the fact that a certain level of daily test capacity, 60,000 test per day in the Province of Ontario, must be maintained in order for the testing-to quarantine intervention to be effective. We calculated that with this minimal testing capacity, a quarantine proportion of no less than 40% is needed if we want the strain-specific quarantine after WGS be useful to prevent an VOC-induced outbreak. We also illustrated that the normal quarantine proportion should be increased to 50% then only less intensive strain-specific quarantine is required.

In conclusion, our analyses suggest that a combination of large COVID-19 clinical test capacity, a short delay in both the clinical test and WGS test and the subsequent contact-tracing and quarantine, and moderate level of additional strain-specific quarantine is a feasible and optimal approach to prevent or mitigate a VOC-driven outbreak. Given this conclusion, we suggest that budgetary consideration for testing should not prevent WGS testing from occurring at the expense of first and concomitant quarantine of traced contacts that were not infected. Given the value of WGS and the additional strain-specific interventions, our study calls for investment of WGS testing capacity. Our model includes S_{qr} and S_{qm} compartments, which capture susceptible individuals who are quarantined due to contact tracing, even though they were not exposed. Although this approach can help limit onward transmission, it also results in the temporary removal of healthy individuals from the workforce, leading to absenteeism and loss of productivity. A recent study [53] developed a mathematical model to quantify the collective impact of COVID-19 and influenza on workplace absenteeism across Canada, highlighting the significant strain that concurrent respiratory outbreaks can impose on workforce availability and productivity. Though our model does not count these economic costs. Future extensions should incorporate cost functions that account for workforce interruptions, productivity loss, and the social burden of unnecessary quarantine. This would allow for a more comprehensive assessment of the trade-offs between epidemiological control

and social impact and help guide more cost-effective public health strategies.

Chapter 3

Mitigating Co-circulation of Seasonal Influenza and COVID-19 Pandemic in the Presence of Vaccination: A Mathematical Modelling Approach

3.1 Introduction

Despite the implementation of non-pharmaceutical interventions (NPIs) [74, 75] and the existence of highly effective vaccines [76], the "Coronavirus Disease 2019" (COVID-19) pandemic still continues to plague the globe [77]. Although the end of the global pandemic has been declared, the emergence of multiple highly contagious strains [78] that can evade the immune response and make the existing vaccines less effective [79, 80], indicates that new waves of COVID-19 will arise [81], with COVID-19 transitioning into an endemic disease [82]. If these waves take place during a typical influenza season in many regions of the world, this would create a situation of co-circulation of multiple respiratory viruses, including influenza

and respiratory syncytial virus (RSV) [83], among others. Since respiratory pathogens share similar symptoms, this poses a serious challenge to the global public health system [84]. During the first two years of the still ongoing COVID-19 pandemic, seasonal influenza infections have been mitigated, likely due to the mandatory use of personal protective equipment (PPE) and the implementation of stringent packages of NPIs to contain the spread of COVID-19 [85]. On the other hand, the lack of exposure to the influenza virus may have also decreased the population immunity levels, and increased susceptibility to influenza because of its low-circulation in the two previous seasons [86]. All this, taken together, may potentially lead to a larger seasonal influenza outbreak when COVID-19 induced social distancing and other restrictions are relaxed, creating the ideal situation for influenza-COVID co-circulating in the population.

The combined risk of the concurrent influenza epidemic and COVID-19 pandemic is a serious global public health concern, since it can be extremely difficult to anticipate influenza circulation in the upcoming winter with COVID-19. Some epidemiological observational studies have investigated the impact of SARS-CoV-2 and influenza viruses co-circulation in terms of prevalence rate of co-circulation, clinical outcomes and imposed burden [84, 87].

Mathematical modeling can play a key role in accounting for interactions of a given pathogen with other infectious agents and in quantifying the real burden of each pathogen and the full impact and effectiveness of public health interventions targeting each infectious agent [88, 89]. This is particularly relevant given that, in the current situation, where SARS-CoV-2 virus is still transmitting continuously in the world despite the availability of many effective vaccines, the emergence of new variants of concern (VOCs) is inevitable.

Considering the additional burden of COVID-19 during the influenza season on population health, and healthcare systems, including emergency departments (EDs), it is of paramount importance to investigate the effects of co-circulations when vaccines are available for both diseases. Therefore, the present mathematical model was developed with the aim of studying

the impact of SARS-CoV-2 during an influenza season, quantitatively assessing the effects of the co-circulation of the two respiratory pathogens. In particular, in the present study, we are interested in finding optimal strategies to manage and control both influenza and COVID-19 outbreaks during the same season. Among many scenarios and interventions, we consider optimal strategies to delay and separate the peaks of influenza outbreak and COVID-19 wave.

3.2 The Co-circulation Model

To investigate the co-circulation of influenza and SARS-CoV-2, a deterministic compartmental model formulated in terms of ordinary differential equations was employed. In light of the objective of the study is to identify potential control strategies to mitigate burden caused by both viruses in the near-term, i.e., during a single respiratory illness season, a number of simplifying assumptions were made to focus on essential elements relevant to the present study. Specifically, the following assumptions were made to enable such a focus. Changes in population demographics were not considered, i.e., births and deaths were not modelled, and the population size remained constant. A closed population was considered and therefore no inbound or outbound travel occurred. It was assumed that the population mixed homogeneously. Age-related heterogeneities (e.g., susceptibility to infection, social contact mixing, vaccination coverage) and spatial heterogeneities (e.g., testing and case reporting, social contact mixing, level of pathogen circulation) were not considered. Given that symptomatic influenza and COVID-19 share similar symptoms, the RT-PCR testing capacity was considered to be a shared resource between infections occurring by both influenza and SARS-CoV-2. Due to scarcity of data and for model simplification, we assume that infections are exclusive and neither pathogen can be supplanted within an infected host. In other words, we assume no co-infection and super-infection of both diseases. However, secondary infection is possible i.e., an individual after recovery from one disease can get infected from other disease. In light of the focus on a single respiratory illness reason, it was

assumed that upon infection by both influenza virus and SARS-CoV-2 (temporally distinct infections) that complete immunity against infection by both pathogens was conferred. All individuals were assumed to be vaccinated before the considerd influenza season start and no vaccination occurred during the season.

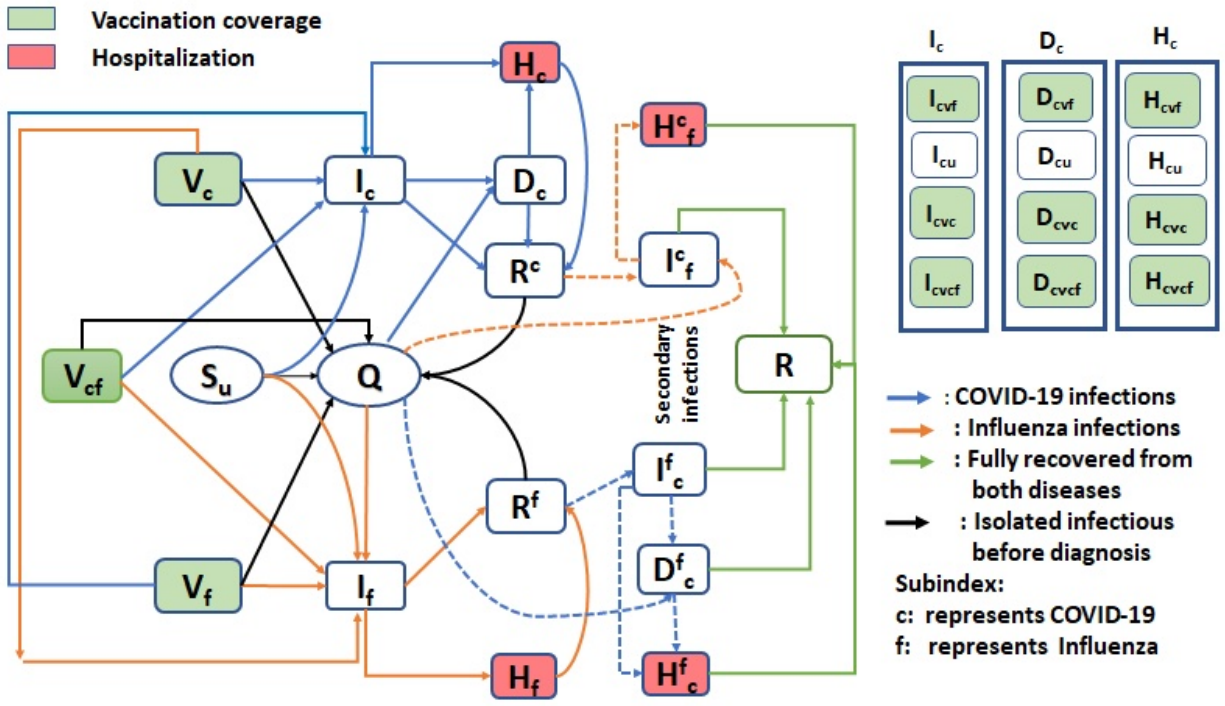

Figure 3.1: Flow diagram of the transmission dynamics model considering the co-circulation of influenza and SARS CoV-2 viruses. On the right side of the diagram, classes I_c, D_c, H_c, represent that there are further sub classes in each of these compartments. Similarly, Flu classes have the sub classes.

The population was stratified into susceptible state, isolated states, infected states, diagnosed states, recovered states and hospitalized states, with further stratification based on epidemiological history (e.g., prior infection) to the two circulating viruses (Figure 1). Vaccination of individuals in the population against both influenza and COVID-19 was considered in the model, therefore dividing the population susceptible to infection by both pathogens into four classes: those individuals not vaccinated against either influenza or

COVID-19 (denoted by S_u), those individuals vaccinated against COVID-19 and not influenza (V_c); those individuals vaccinated against influenza and not COVID-19 (V_f); those individuals vaccinated against influenza and COVID-19 (V_{cf}). Each of these four groups could potentially be infected by SARS-CoV-2 and influenza, with vaccination modulating the infection risk in each class.

In the model, unvaccinated individuals (S_u) were infected by influenza at rate λ_f and with SARS-CoV-2 at rate λ_c. Vaccination status modulated the infection process as follows: Individuals vaccinated against influenza were assumed to be infected by influenza at a reduced rate $(1-\phi_f)\lambda_f$, where ϕ_f is the vaccine effectiveness against infection by influenza. It has been suggested that influenza vaccination may reduce susceptibility to COVID-19 [90, 91]; therefore, those individuals vaccinated against influenza were assumed to be infected by SARS-CoV-2 at the reduced rate $(1-\eta)\lambda_c$, where $0 \leq \eta \leq 1$. Individuals vaccinated against both COVID-19 and influenza were therefore infected by SARS-CoV-2 at rate $\lambda_c(1-\phi_c)(1-\eta)$ and by influenza virus at rate $(1-\phi_f)\lambda_f$.

Upon infection, and in light of the fact that influenza and COVID-19 share common symptoms, it was assumed that a fraction q of symptomatic individuals isolate themselves until their test results become available (thus entering the Q class); meanwhile, the remaining proportion $(1-q)$ continue socio-economic activity without disruption (i.e., their contact patterns were assumed to remain unaltered). Those individuals in the isolated (Q) class that have tested positive for COVID-19 were assumed to remain isolated and not infectious; meanwhile, those individuals in which have tested negative were assumed to end their isolation and resume normal mixing.

Those individuals in I_c are either diagnosed and isolated, recovered naturally or hospitalized from their primary infection. This is in contrast to individuals in I_f who either recover naturally or are hospitalized from their primary infection. Given that the study is concerned with a single respiratory disease season, we considered the case where recovery from this

primary infection yields immunity to re-infection by the same pathogen. Meanwhile, those recovered from primary infection (R^f, R^c) become susceptible to secondary infection. In the case where an individual experiences primary and secondary infection, they are considered to be immune to infection by both influenza and SARS-CoV-2.

Infectious individuals, either influenza (I_f) or COVID-19 (I_c), may be diagnosed and subsequently COVID-19 tested positive individuals are isolated (moving to (D_c) compartment), while COVID-19 tested negative will move out from the Q class to (I_f) compartment. Later on, we will specify how the diagnosis speed is impacted by the incidence of both diseases since they share common symptoms.

Isolated individuals were assumed to no longer transmit the disease. Furthermore, diagnosed (D_c) and infectious individuals (I_f) or (I_c) can recover from influenza or COVID-19 respectively at the rate, γ_{cD} and γ_{fI} , γ_{cI} (moving to class R^f or R^c, respectively), or they will be admitted to hospitals with disease-induced severity, at the rate of τ_f from I_f class, and at the rate θ_c ,τ_c from D_c, I_c class respectively.

We assume that after recovery from either of these diseases, an individual is completely immune (recall this research focuses on a flu season only) to that disease but susceptible to the other disease. Individuals recovered from COVID-19 but infected with influenza are denoted by I_f^c, hospitalised H_f^c. Those individuals recovered from influenza but infected with COVID-19 are denoted by I_c^f, with the diagnosed and isolated denoted by D_c^f and hospitalised H_c^f. Individuals experiencing such secondary infections become immune to both diseases after the recovery from the second disease.

3.2.1 Standing assumptions

We assume a fraction of the population receive the flu vaccine, and another fraction of the population receive the COVID-19 vaccine. It is possible that a fraction of the population receive vaccines for both influenza and COVID-19. We assume they receive the vaccine(s)

before our considered influenza season starts. We do not assume a perfect vaccine so individuals received a vaccine can still be infected by the disease intended. Furthermore, we assume a vaccine against influenza or COVID-19 reduces risk of being infected (reduction in susceptibility), and reduces the risk of severity of disease (hospitalization) if infected by the disease the vaccine is intended.

The flow diagram of the model formulation is shown in Figure 1. Note that in each class other than susceptibles (S_u,V_c,V_f,V_{cf}) and completely recovered R classes, there are further four sub classes that are tracked. For instance, the I_c class have I_{cvc}, I_{cvf}, I_{cu} and I_{cvcf} sub classes. In these sub classes, the first letter in sub index represents the disease class 'f' for flu and 'c' for COVID-19. Other indices represent the status of the vaccine. For example,

I_{cvc}: First letter 'c' in sub index means infectious with COVID-19, next 'vc' represents vaccinated with COVID-19.

I_{cvf}: First letter 'c' in sub index means infectious with COVID-19, next 'vf' represents vaccinated with flu.

I_{cu}: First letter 'c' in sub index means infectious with COVID-19, next 'u' represents unvaccinated.

I_{cvcf}: First letter 'c' in sub index means infectious with COVID-19, next 'vcf' represents vaccinated with both flu and COVID.

Due to the co-circulation of both influenza and SARS CoV-2 in a single season and due to their common symptoms, the COVID-19 testing can be slowed down with a large number of individuals infected with either flu and COVID-19. Therefore, the diagnostic rate to confirm the disease type is a decreasing function of the total number of infections (with either flu or COVID-19) modeled by the available testing capacity. This can be modelled using the Holling Type II functions:

$$F_c(I_c, I_f, I_f^c, I_c^f, Q) = \frac{\delta_{Ic} I_c}{1 + w(I_c + I_f + I_f^c + I_c^f + Q)},$$

$$F_f(I_c, I_f, I_f^c, I_c^f, Q) = \frac{\delta_{If} I_f}{1 + w(I_c + I_f + I_f^c + I_c^f + Q)},$$

$$F_f^c(I_c, I_f, I_f^c, I_c^f, Q) = \frac{\delta_{If} I_f^c}{1 + w(I_c + I_f + I_f^c + I_c^f + Q)},$$

$$F_c^f(I_c, I_f, I_f^c, I_c^f, Q) = \frac{\delta_{Ic} I_c^f}{1 + w(I_c + I_f + I_f^c + I_c^f + Q)},$$

$$F_Q(I_c, I_f, I_f^c, I_c^f, Q) = \frac{\delta_Q Q}{1 + w(I_c + I_f + I_f^c + I_c^f + Q)},$$

, where w is the constant such that $1/w$ is the maximum number of people who can be tested per day(testing capacity per day). These functions characterise the saturation phenomenon of limited testing resources.

3.2.1.1 Forces of infections: COVID-19 and influenza

We use standard incidence to describe the forces of infections:

$$\lambda_c = \frac{\beta_c C(I_{cu} + I_{cvf} + I_{cvc} + I_{cvcf} + I_{cu}^f + I_{cvf}^f + I_{cvc}^f + I_{cvcf}^f)}{N},$$

$$\lambda_f = \frac{\beta_f C(I_{fu} + I_{fvf} + I_{fvc} + I_{fvcf} + I_{fu}^c + I_{fvf}^c + I_{fvc}^c + I_{fvcf}^c)}{N}.$$

In summary, the mathematical model for the co-circulation of COVID-19 and flu is given below, with two diseases coupled through their impact on testing speed (and thus isolation duration of the flu patients):

$$S'_u = -\lambda_c S_u - \lambda_f S_u \tag{3.1}$$

$$V'_c = -\lambda_c(1-\phi_c)V_c - \lambda_f V_c \tag{3.2}$$

$$V'_f = -\lambda_f(1-\phi_f)V_f - \lambda_c(1-\eta)V_f \tag{3.3}$$

$$V'_{cf} = -\lambda_f(1-\phi_f)V_{cf} - \lambda_c(1-\phi_c)(1-\eta)V_{cf} \tag{3.4}$$

Note that there are sixteen subclasses in Q compartment, i.e.

$$\begin{aligned} Q' = {} & Q'_{cvc} + Q'_{cvf} + Q'_{cu} + Q'_{cvcf} + Q'_{fvc} + Q'_{fvf} + Q'_{fu} + Q'_{fvcf} + \\ & Q'^{c}_{fvc} + Q'^{c}_{fu} + Q'^{c}_{fvf} + Q'^{c}_{fvcf} + Q'^{f}_{cvc} + Q'^{f}_{cu} + Q'^{f}_{cvf} + Q'^{f}_{cvcf} \end{aligned}$$

where,

$$\begin{cases} Q'_{cvc} = q\lambda_c(1-\phi_c)V_c - F_{Qcvc} \\ Q'_{cvf} = q\lambda_c(1-\eta)V_f - F_{Qcvf} \\ Q'_{cu} = q\lambda_c S_u - F_{Qcu} \\ Q'_{cvcf} = q\lambda_c(1-\phi_c)(1-\eta)V_{cf} - F_{Qcvcf} \\ Q'_{fvc} = q\lambda_f V_f - F_{Qfvc} \\ Q'_{fvf} = q\lambda_f(1-\phi_f)V_f - F_{Qfvf} \\ Q'_{fu} = q\lambda_f S_f - F_{Qfu} \\ Q'_{fvcf} = q\lambda_f(1-\phi_f)V_{cf} - F_{Qfvcf} \\ Q'^c_{fvc} = q\lambda_f R^c_{vc} - F^c_{Qfvc} \\ Q'^c_{fvf} = q\lambda_f(1-\phi_f)R^c_{vf} - F^c_{Qfvf} \\ Q'^c_{fu} = q\lambda_f R^c_u - F^c_{Qfu} \\ Q'^c_{fvcf} = q\lambda_f(1-\phi_f)R^c_{vcf} - F^c_{fvcf} \\ Q'^f_{cvc} = q\lambda_c(1-\phi_c)R^f_{vc} - F^f_{Qcvc} \\ Q'^f_{cvf} = q\lambda_c(1-\eta)R^f_{vf} - F^f_{Qcvf} \\ Q'^f_{cu} = q\lambda_c R^f_u - F^f_{Qcu} \\ Q'^f_{cvcf} = q\lambda_c(1-\phi_c)(1-\eta)R^f_{vcf} - F^f_{Qcvcf} \end{cases} \tag{3.5}$$

Further, we consider subclasses of I_c as follows.

$$\boxed{I'_c = I'_{cu} + I'_{cvf} + I'_{cvc} + I'_{cvcf}}$$

$$\begin{cases} I'_{cvc} = (1-q)\lambda_c(1-\phi_c)V_c - \gamma_c I_{cvc} - F_{cvc}(I_c, I_f, I_f^c, I_c^f, Q) - (1-\kappa_c)\tau_c I_{cvc} \\ I'_{cvf} = (1-q)\lambda_c(1-\eta)V_f - \gamma_c I_{cvf} - F_{cvf}(I_c, I_f, I_f^c, I_c^f, Q) - \tau_c I_{cvf} \\ I'_{cu} = (1-q)\lambda_c S_u - \gamma_c I_{cu} - F_{cu}(I_c, I_f, I_f^c, I_c^f, Q) - \tau_c I_{cu} \\ I'_{cvcf} = (1-q)\lambda_c(1-\phi_c)(1-\eta)V_{cf} - \gamma_c I_{cvcf} - F_{cvcf}(I_c, I_f, I_f^c, I_c^f, Q) - (1-\kappa_c)\tau_c I_{cvcf} \end{cases} \tag{3.6}$$

$$\boxed{D'_c = D'_{cu} + D'_{cvf} + D'_{cvc} + D'_{cvcf}}$$

$$\begin{cases} D'_{cvc} = F_{cvc}(I_c, I_f, I_f^c, I_c^f, Q) + F_{Qcvc}(I_c, I_f, I_f^c, I_c^f, Q) - \gamma_{cD} D_{cvc} - (1-\kappa_c)\theta_c D_{cvc} \\ D'_{cvf} = F_{cvf}(I_c, I_f, I_f^c, I_c^f, Q) + F_{Qcvf}(I_c, I_f, I_f^c, I_c^f, Q) - \gamma_{cD} D_{cvf} - \theta_c D_{cvf} \\ D'_{cu} = F_{cu}(I_c, I_f, I_f^c, I_c^f, Q) + F_{Qcu}(I_c, I_f, I_f^c, I_c^f, Q) - \gamma_{cD} D_{cu} - \theta_c D_{cu} \\ D'_{cvcf} = F_{cvcf}(I_c, I_f, I_f^c, I_c^f, Q) + F_{Qcvcf}(I_c, I_f, I_f^c, I_c^f, Q) - \gamma_{cD} D_{cvcf} - (1-\kappa_c)\theta_c D_{cvcf} \end{cases} \tag{3.7}$$

$$\boxed{H'_c = H'_{cu} + H'_{cvf} + H'_{cvc} + H'_{cvcf}}$$

$$\begin{cases} H'_{cvc} = (1-\kappa_c)\theta_c D_{cvc} + (1-\kappa_c)\tau_c I_{cvc} - \gamma_{cH} H_{cvc} \\ H'_{cvf} = \theta_c D_{cvf} + \tau_c I_{cvf} - \gamma_{cH} H_{cvf} \\ H'_{cu} = \theta_c D_{cu} + \tau_c I_{cu} - \gamma_{cH} H_{cu} \\ H'_{cvcf} = (1-\kappa_c)\theta_c D_{cvcf} + (1-\kappa_c)\tau_c I_{cvcf} - \gamma_{cH} H_{cvcf} \end{cases} \tag{3.8}$$

Here confirmed/diagnosed cases go to hospitals at rate θ_c and infected but not diagnosed at rate τ_c, and κ_c is the effectiveness of COVID vaccine to severity of infection to breakthrough

infection.

$$\boxed{R'^c = R'^c_{vc} + R'^c_u + R'^c_{vf} + R'^c_{vcf}}$$

$$\begin{cases} R'^c_{vc} = -\lambda_f R^c_{vc} + \gamma_{cH} H_{cvc} + \gamma_{cD} D_{cvc} + \gamma_c I_{cvc} \\ R'^c_{vf} = -\lambda_f (1-\phi_f) R^c_{vf} + \gamma_{cH} H_{cvf} + \gamma_{cD} D_{cvf} + \gamma_c I_{cvf} \\ R'^c_u = -\lambda_f R^c_u + \gamma_{cH} H_{cu} + \gamma_{cD} D_{cu} + \gamma_c I_{cu} \\ R'^c_{vcf} = -\lambda_f (1-\phi_f) R^c_{vcf} + \gamma_{cH} H_{cvcf} + \gamma_{cD} D_{cvf} + \gamma_c I_{cvcf} \end{cases} \tag{3.9}$$

$$\boxed{I'^c_f = I'^c_{fvc} + I'^c_{fu} + I'^c_{fvf} + I'^c_{fvcf}}$$

$$\begin{cases} I'^c_{fvc} = (1-q)\lambda_f R^c_{vc} - \gamma_f I^c_{fvc} - \tau_f I^c_{fvc} + F^c_{Qfvc}(I_c, I_f, I^c_f, I^f_c, Q) \\ I'^c_{fvf} = (1-q)\lambda_f (1-\phi_f) R^c_{vf} - \gamma_f I^c_{fvf} - \tau_f (1-\kappa_f) I^c_{fvf} + F^c_{Qfvf}(I_c, I_f, I^c_f, I^f_c, Q) \\ I'^c_{fu} = (1-q)\lambda_f R^c_u - \gamma_f I^c_{fu} - \tau_f I^c_{fu} + F^c_{Qfu}(I_c, I_f, I^c_f, I^f_c, Q) \\ I'^c_{fvcf} = (1-q)\lambda_f (1-\phi_f) R^c_{vcf} - \gamma_f I^c_{fvcf} - \tau_f (1-\kappa_f) I^c_{fvcf} + F^c_{fvcf}(I_c, I_f, I^c_f, I^f_c, Q) \end{cases} \tag{3.10}$$

$$\boxed{H'^c_f = H'^c_{fvc} + H'^c_{fu} + H'^c_{fvf} + H'^c_{fvcf}}$$

$$\begin{cases} H'^c_{fvc} = \tau_f I^c_{fvc} - \gamma_{fH} H^c_{fvc} \\ H'^c_{fvf} = \tau_f (1-\kappa_f) I^c_{fvf} - \gamma_{fH} H^c_{fvf} \\ H'^c_{fu} = \tau_f I^c_{fu} - \gamma_{fH} H^c_{fu} \\ H'^c_{fvcf} = \tau_f (1-\kappa_f) I^c_{fvcf} - \gamma_{fH} H^c_{fvcf} \end{cases} \tag{3.11}$$

$$\boxed{I'_f = I'_{fvc} + I'_{fu} + I'_{fvf} + I'_{fvcf}}$$

$$\begin{cases} I'_{fvc} = (1-q)\lambda_f V_c - \gamma_f I_{fvc} + F_{Qfvc}(I_c, I_f, I_f^c, I_c^f) - \tau_f I_{fvc} \\ I'_{fvf} = (1-q)\lambda_f (1-\phi_f) V_f - \gamma_f I_{fvf} + F_{Qfvf}(I_c, I_f, I_f^c, I_c^f) - \tau_f (1-\kappa_f) I_{fvf} \\ I'_{fu} = (1-q)\lambda_f S_u - \gamma_f I_{fu} + F_{Qfu}(I_c, I_f, I_f^c, I_c^f) - \tau_f I_{fu} \\ I'_{fvcf} = (1-q)\lambda_f (1-\phi_f) V_{cf} - \gamma_f I_{cvcf} + F_{Qfvcf}(I_c, I_f, I_f^c, I_c^f) - \tau_f (1-\kappa_f) I_{cvcf} \end{cases} \tag{3.12}$$

$$\boxed{H'_f = H'_{fvc} + H'_{fu} + H'_{fvf} + H'_{fvcf}}$$

$$\begin{cases} H'_{fvc} = \tau_f I_{fvc} - \gamma_{fH} H_{fvc} \\ H'_{fvf} = \tau_f (1-\kappa_f) I_{fvf} - \gamma_{fH} H_{fvf} \\ H'_{fu} = \tau_f I_{fu} - \gamma_{fH} H_{fu} \\ H'_{fvcf} = \tau_f (1-\kappa_f) I_{fvcf} - \gamma_{fH} H_{fvcf} \end{cases} \tag{3.13}$$

$$\boxed{R'^f = R'^f_{vc} + R'^f_u + R'^f_{vf} + R'^f_{vcf}}$$

$$\begin{cases} R'^f_{vc} = -\lambda_c (1-\phi_c) R^f_{vc} + \gamma_{fH} H_{fvc} + \gamma_f I_{fvc} \\ R'^f_{vf} = -\lambda_c (1-\eta) R^f_{vf} + \gamma_{fH} H_{fvf} + \gamma_f I_{fvf} \\ R'^f_u = -\lambda_c R^f_u + \gamma_{fH} H_{fu} + \gamma_f I_{fu} \\ R'^f_{vcf} = -\lambda_c (1-\phi_c) R^f_{vcf} + \gamma_{fD} D_{fvcf} + \gamma_f I_{fvcf} \end{cases} \tag{3.14}$$

$$\boxed{I'^f_c = I'^f_{cvc} + I'^f_{cu} + I'^f_{cvf} + I'^f_{cvcf}}$$

$$\begin{cases} I'^{f}_{cvc} = (1-q)\lambda_c(1-\phi_c)R^f_{vc} - \gamma_c I^f_{cvc} - \tau_c(1-\kappa_c)I^f_{cvc} - F^f_{cvc}(I_c, I_f, I^c_f, I^f_c) \\ I'^{f}_{cvf} = (1-q)\lambda_c(1-\eta)R^f_{vf} - \gamma_c I^f_{cvf} - \tau_c I^f_{cvf} - F^f_{cvf}(I_c, I_f, I^c_f, I^f_c) \\ I'^{f}_{cu} = (1-q)\lambda_c R^f_{u} - \gamma_c I^f_{cu} - \tau_c I^f_{cu} - F^f_{cu}(I_c, I_f, I^c_f, I^f_c) \\ I'^{f}_{cvcf} = (1-q)\lambda_c(1-\phi_c)(1-\eta)R^f_{vcf} - \gamma_c I^f_{cvcf} - \tau_c(1-\kappa_c)I^f_{cvcf} - F^f_{cvcf}(I_c, I_f, I^c_f, I^f_c) \end{cases} \tag{3.15}$$

$$\boxed{D'^{f}_{c} = D'^{f}_{cvc} + D'^{f}_{cu} + D'^{f}_{cvf} + D'^{f}_{cvcf}}$$

$$\begin{cases} D'^{f}_{cvc} = F^f_{cvc}(I_c, I_f, I^c_f, I^f_c) + F^f_{Qcvc} - \gamma_{cD} D^f_{cvc} - \theta_c(1-\kappa_c)D^f_{cvc} \\ D'^{f}_{cvf} = F^f_{cvf}(I_c, I_f, I^c_f, I^f_c) + F^f_{Qcvf} - \gamma_{cD} D^f_{cvf} - \theta_c D^f_{cvf} \\ D'^{f}_{cu} = F^f_{cu}(I_c, I_f, I^c_f, I^f_c) + F^f_{Qu} - \gamma_{cD} D^c_{fu} - \theta_c D^f_{cu} \\ D'^{f}_{cvcf} = F^f_{cvcf}(I_c, I_f, I^c_f, I^f_c) + F^f_{Qcvcf} - \gamma_{cD} D^c_{fvcf} - \theta_c(1-\kappa_c)D^f_{fvcf} \end{cases} \tag{3.16}$$

$$\boxed{H'^{f}_{c} = H'^{f}_{cvc} + H'^{f}_{cu} + H'^{f}_{cvf} + H'^{f}_{cvcf}}$$

$$\begin{cases} H'^{f}_{cvc} = \theta_c(1-\kappa_c)D^f_{cvc} + \tau_c(1-\kappa_c)I^f_{cvc} - \gamma_{cH} H'^{f}_{cvc} \\ H'^{f}_{cvf} = \theta_c D^f_{cvf} + \tau_c I^f_{cvf} - \gamma_{cH} H'^{f}_{cvf} \\ H'^{f}_{cu} = \theta_c D^{fc}_{cu} + \tau_c I^f_{cu} - \gamma_{cH} H'^{f}_{cu} \\ H'^{f}_{cvcf} = \theta_c(1-\kappa_c)D^f_{cvcf} + \tau_c(1-\kappa_c)I^f_{cvcf} - \gamma_{cH} H'^{f}_{fvcf} \end{cases} \tag{3.17}$$

Taking

$$I^f_c = I^f_{cvc} + I^f_{cu} + I^f_{cvf} + I^f_{cvcf}$$

$$D^f_c = D^f_{cvc} + D^f_{cu} + D^f_{cvf} + D^f_{cvcf}$$

$$H_c^f = H_{cvc}^f + H_{cu}^f + H_{cvf}^f + H_{cvcf}^f$$

$$I_f^c = I_{fvc}^c + I_{fu}^c + I_{fvf}^c + I_{fvcf}^c$$

$$H_f^c = H_{fvc}^c + H_{fu}^c + H_{fvf}^c + H_{fvcf}^c$$

We get the equation for fully recovered class from both diseases.

$$R' = \gamma_c I_c^f + \gamma_{cD} D_c^f + \gamma_{cH} H_c^f + \gamma_f I_f^c + \gamma_{fH} H_f^c \tag{3.18}$$

3.2.1.2 Dose-specific (COVID-19) vaccine effectiveness

Most existing vaccines are found to be effective against COVID-19 disease, however emergence and persistent spread of new SARS-CoV-2 variants render these vaccines less effective against circulating strain[92, 93]. The effectiveness of COVID-19 vaccines against infection also varies by the number of doses. Our study considers the case where the circulating strain is Omicron (B.1.1.529) variant. The first dose of COVID-19 has been deemed ineffective against Omicron infection, but the vaccine effectiveness against second, third and fourth dose increases, and will be assumed to be 0.06, 0.39, 0.49, respectively [94, 29]. To be more generic, the COVID-19 vaccine effectiveness in our model is defined as follows:

$$\phi_c = \rho_1 * ef_1 + \rho_2 * ef_2 + \rho_3 * ef_3 + \rho_4 * ef_4,$$

where ef_1, ef_2, ef_3 and ef_4 represents effectiveness of dose 1,2,3 and 4 respectively against infection and ρ_1, ρ_2 , ρ_3, ρ_4 represents vaccine coverage with dose 1,2,3 and 4 respectively.

3.2.1.3 Recovery rate of diagnosed/isolated individuals

As documented in [95], for COVID-19 laboratory based testing, patient samples must be first transported to the laboratory and therefore it takes 1 to 3 days to receive test results. So, in what follows, we take diagnose rate $\delta_c = 1/2day^{-1}$ as the baseline assumption. Since we are assuming only flu and COVID-19 are co-circulating a COVID-19 test negative result implies flu test positive, hence we assume the same diagnostic rate for influenza. Further, to calculate the average infectious period $1/\gamma_{cD}$ of COVID-19 test positive/isolated cases, we use

$$1/\gamma_c = \text{average infectious period for Covid-19 ,}$$

and

$$1/\delta_c = \text{average time to test positive of a Covid-19 infection.}$$

Therefore,

$$1/\gamma_{cD} = 1/\gamma_c - 1/\delta_c, \;\; \gamma_{cD} = \frac{\gamma_c \delta_c}{\delta_c - \gamma_c}.$$

As individuals are tested before they recover, $1/\gamma_c > 1/\delta_c$.

3.2.2 Parameters and initial conditions

We have used some of the data of the province Ontario, Canada as case study. We take the following initial values for vaccinated and unvaccinated state variables. We assume N_0 is the total population of Ontario. From [96], 84.81% of the total population of Ontario is vaccinated with COVID-19 either with dose one, two, three or four by July 19th, 2022. So, initially, a proportion of the population vaccinated with COVID-19 is $V_c = 0.8481 \times N_0$. As a baseline, we assume 40% [97] of the population which is vaccinated with COVID-19 also get the Influenza vaccine. Thus this fraction will move to the V_{cf0} initially vaccinated with

both COVID-19 and influenza class. This gives,

$$V_{c0} = 0.8481 \times N_0 - V_{cf0}, V_{cf0} = 0.4 \times 0.8481 \times N_0.$$

Furthermore, because a large proportion of population has received COVID-19 vaccine and only a small proportion (15.19%) is left unvaccinated, we assume 10% of the remaining (COVID-19) unvaccinated population is vaccinated with influenza only. Hence, initially vaccinated with influenza is

$$V_{f0} = 0.1 \times (N_0 - 0.8481 \times N_0).$$

Thus, unvaccinated class has the initial value

$$S_{u0} = N_0 - V_{c0} - V_{cf0} - V_{f0}.$$

The effectiveness of influenza vaccine against hospitalization range about 35%-60% by age [98, 99]. In our study, we assume a homogeneous population, so in our simulations, we use 50% as a baseline. Most of the other parameters are taken from literature. In particular, we numerically estimated the baseline transmission probability β_c for B.A.5 by inverting the formula of reproduction number Ro and following the approach in [100] and using the change in the transmission probability from the ancestral strain to BA.5 in [101, 102]. Some of parameters relevant to influenza including τ_f, the rate at which influenza infectious cases hospitalised and δ_f, diagnose time of symptomatic infected with influenza, are assumed to be same as COVID-19 for simplifications. On average the time a person with COVID-19 stays in hospital is 12 days[103], and 10 days for influenza. Further, a fraction q of individuals who are isolated immediately on symptoms before testing is chosen 50% as a baseline. The parameters of the co-circulation model is given in the Table 1.

Table 3.1: Parameters definitions and values with references

Parameter List			
Parameter	Definition	Value	Source
β_c	Probability of transmission of COVID	0.1351	Estimated for BA.5
β_f	Probability of transmission of Influenza	0.02-0.035	[104]
C	Contact rate	11.58	[105]
η	Protective effect against infection by the coronavirus if vaccinated with influenza	0.297	[91]
ϕ_c	COVID-19 vaccine effectiveness against infection	Section 2.1.2	[106]
ϕ_f	Influenza Vaccine effectiveness against infection (reduction in susceptibility)	0.4-0.6	[107],[108]
γ_c	Recovery rate of COVID-19 infectious individuals	1/7	[100]
γ_{cD}	Recovery rate of COVID-19 diagnosed isolated individuals	1/5	Section 2.1.3
γ_{cH}	Recovery rate of COVID-19 hospitalized individuals	1/12	[103]
γ_f	Recovery rate of influenza infectious individuals	1/5	[89]
q	Fraction of individuals isolated on symptoms before testing	0.5	Assumed
γ_{fH}	Recovery rate of influenza hospitalized individuals	1/10	Assumed
δ_c	Diagnose rate of symptomatic infected with COVID	1/2	[109]
δ_f	Diagnose rate of symptomatic infected with influenza	1/2	Assumed
$1/w$	Maximum testing capacity per day	6000	[110]
θ_c	Rate at which COVID-19 confirmed cases hospitalised	0.0305	[111]
τ_c	Rate at which COVID-19 infectious cases hospitalised	0.0305	[111]
τ_f	Rate at which influenza infectious cases hospitalised	0.0305	Assumed
κ_c	Vaccine effectiveness against hospitalisation with COVID	0.8-0.95	[106]
κ_f	Vaccine effectiveness against hospitalisation with influenza	0.35-0.5748	[112],[98]

3.3 Simulation Results

Increasing COVID-19 test capacity: For simulations below, first we vary the testing capacity from 6000 to 30,000 in Figure 3.2.

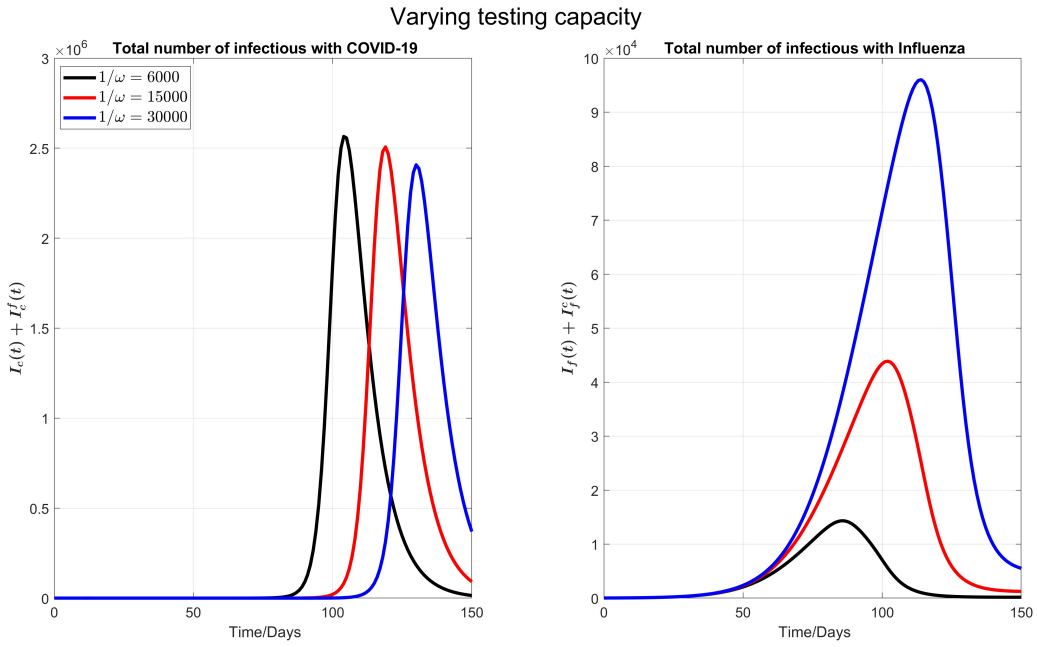

Figure 3.2: The impact of varying the maximum testing capacity per day on COVID-19 and influenza disease prevalence. Left plot represents the total number of infections with COVID-19 $(I_c(t) + I_c^f(t))$ and right plot shows the total number of infections with influenza $(I_f(t) + I_f^c(t))$.

We observe that by increasing testing capacity, the peak time of COVID-19 is postponed and peak value is also reduced (left plot in the figure). On the other side (right plot of the figure), the peak time of influenza cases is delayed but the peak number of influenza infections increases when the COVID-19 test capacity is increased. This is because, when more tests are done per day then more individuals isolated because the common flu and COVID-19 symptoms are diagnosed earlier, and those who are tested negative for COVID-19 will terminate their isolation. So, early conclusion of COVID-19 negative will increase the

force of infections for flu.

Varying flu transmission rate: Next, as shown in Figure 3.3, we consider varying the transmission probability of influenza β_f. This consideration is motivated by the significantly low flu cases during the COVID-19 pandemic due to social distancing. Consequently, there is a possibility that in the coming flu season the population has larger than normal susceptibility to the flu. In our simulations, we kept testing capacity 6000 as a base line.

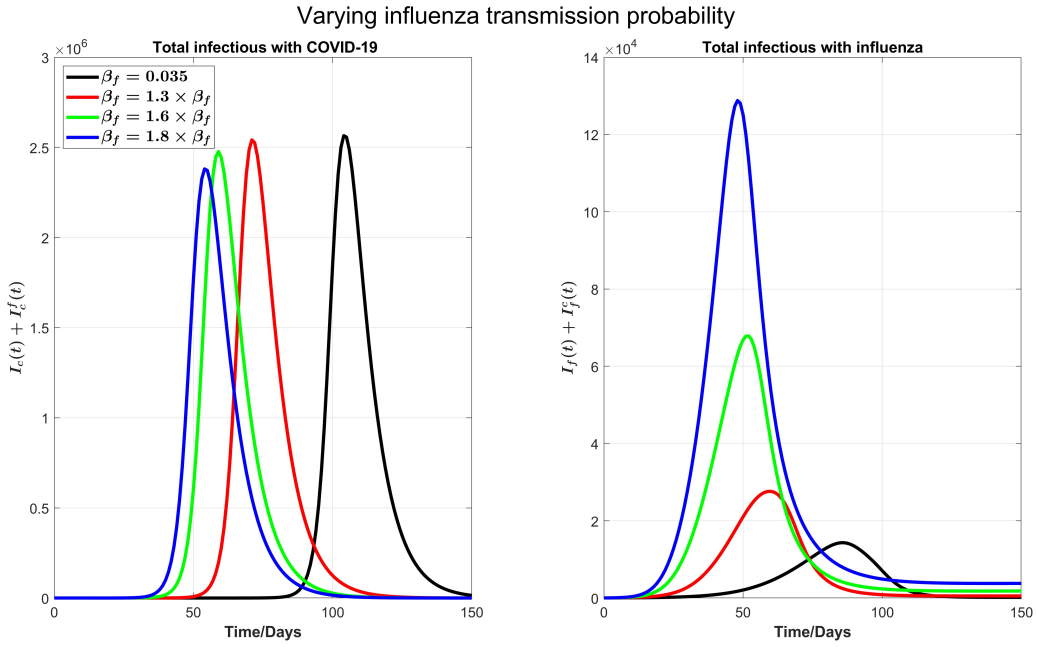

Figure 3.3: The impact of varying the transmission probability β_f on COVID-19 and influenza disease prevalence. Left plot represents the total number of infections with COVID-19 $(I_c(t) + I_c^f(t))$ and right plot shows the total number of infections with influenza $(I_f(t) + I_f^c(t))$.

We can see from right plot of Figure 3.3, influenza cases increases and peak earlier by increasing β_f, which is obvious. However, by increasing transmission probability of influenza, COVID-19 cases (left plot) peaks earlier with visible higher peak value. For example, if β_f is increased by 30%, from 0.035 to 0.0455, COVID-19 infections peak about 30 days earlier. Again this is attributed by the testing delay due to the high volume of influenza infections: the higher the transmission probability for flu, the earlier the peak time for flu outbreak and the higher the number of infections with flu-like symptoms to slow down the COVID-19 testing, leading to delay in full isolation of COVID-19 patients. Figure 3.4, shows the impact of increasing β_f on influenza and COVID-19 infections with high resolution in first 30 days.

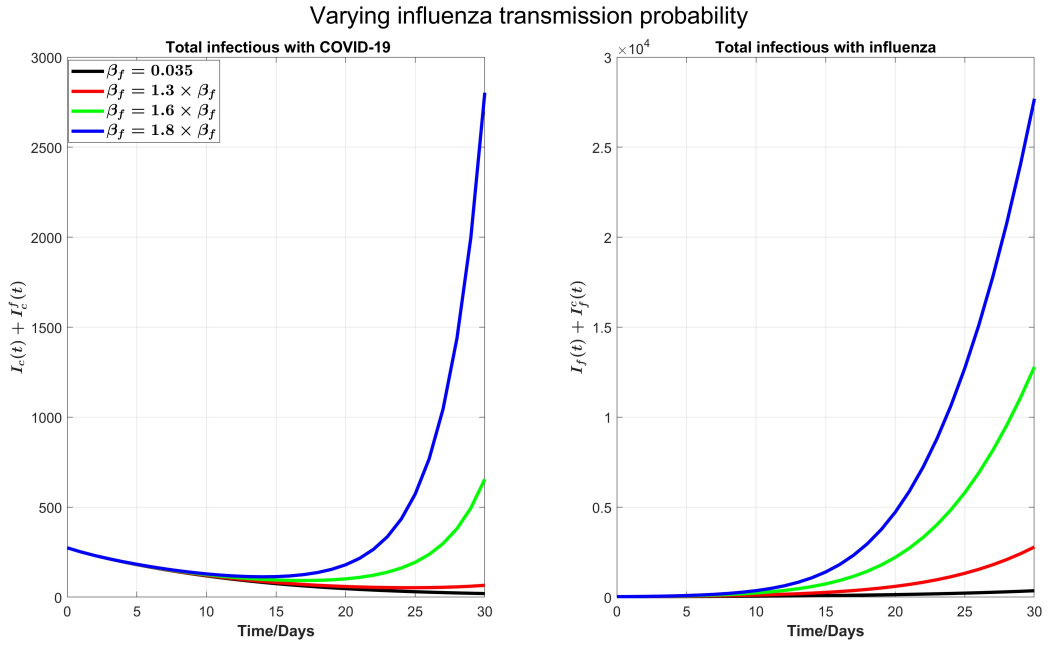

Figure 3.4: A plot with high resolution the case in Figure 3.3 for 30 days. Note that the scale of the infections in this plot is some orders of magnitude smaller than Figure 3.3.

3.3.1 The influenza vaccine and COVID-19 booster coverage

We now consider the issue of minimal and optimal coverage of COVID-19 booster(3rd) and 4th dose and influenza vaccine to control both diseases or to reduce the burden of both diseases together in a single season.

In Figure 3.5, we start with considering 40% of individuals who are vaccinated with COVID-19 either with first, 2nd or third dose also get vaccine of influenza. As of July 19th, 2022, 84.81% of the Ontario residents are fully vaccinated with COVID-19. As such, we consider 33.92% of Ontario residents are vaccinated with influenza from this fraction of population; and 10% of remaining 15.19 % who are not vaccinated with COVID-19 receive influenza vaccine. Thus, overall population initially vaccinated with influenza is $33.92\% + 1.519\% = 35.43\%$. Finally, the proportion of the Ontario population which has received booster dose is 41.35%. In our simulations, we will consider this coverage to be increased to 50%, 60% and 70%, respectively to see the impact of increasing booster coverage on prevalence of both COVID-19 and influenza.

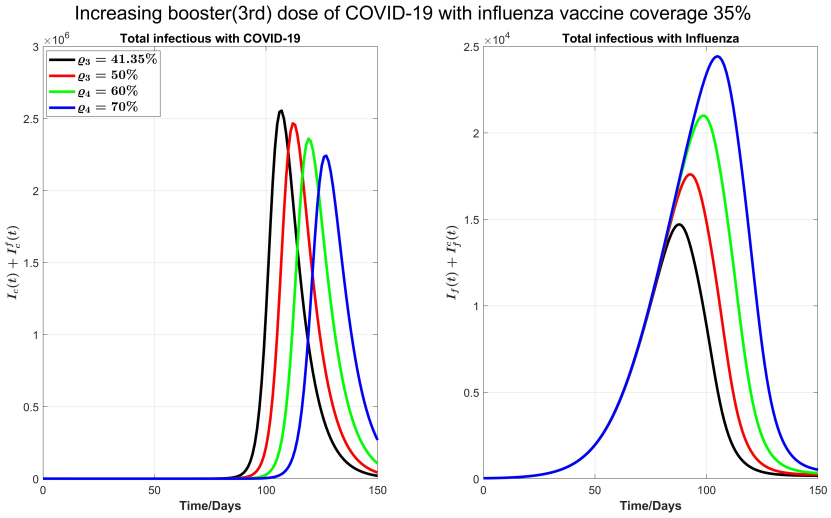

Figure 3.5: Impact of increasing booster dose when influenza vaccine coverage is 35.43%.

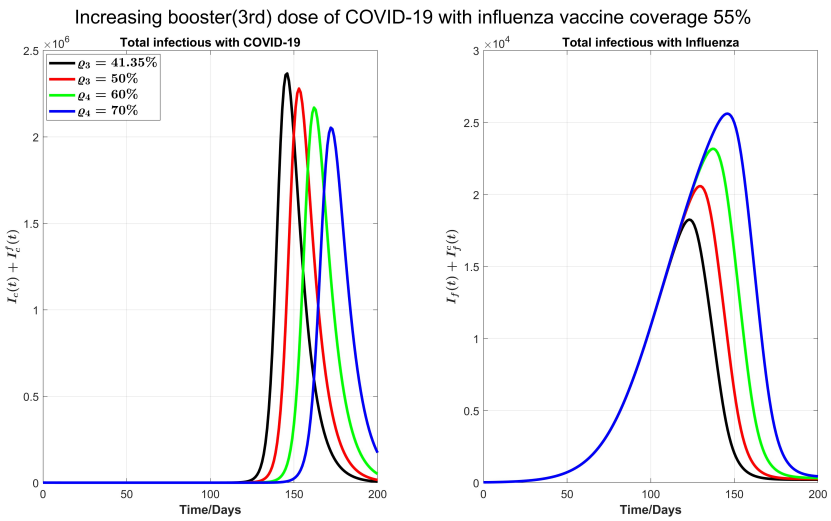

Figure 3.6: Increasing booster dose when influenza vaccine coverage also increases to 55%.

In left plot of Figure 3.5, we observe delaying the COVID-19 peak and reducing the peak size by increasing COVID-19 booster coverage. On the other hand, in the right plot, we observe increase of influenza peak value with increasing COVID-19 booster coverage, increasing the coverage from 41.35% to 70% will see flu peak value changes from close to 15,000 to close to 25000. This is because when we increase the COVID-19 booster coverage there will be less COVID-19 infections and hence less isolation, so this increases the population susceptible to flu.

Next, as shown in Figure 3.6 we investigate the impact of increasing the influenza vaccine coverage to 55% from 35%, along with the increase of the booster dose of COVID-19. We observe that, though there is no significant impact of increasing influenza vaccine coverage on peak values of both diseases,though the peak size of influenza infections increases by increasing influenza vaccine coverage, peak times for both diseases are remarkably delayed. Similar results in Figure3.7 are observed by increasing 10% coverage of booster (3rd dose) and 4th dose of COVID-19 and influenza coverage 55%.

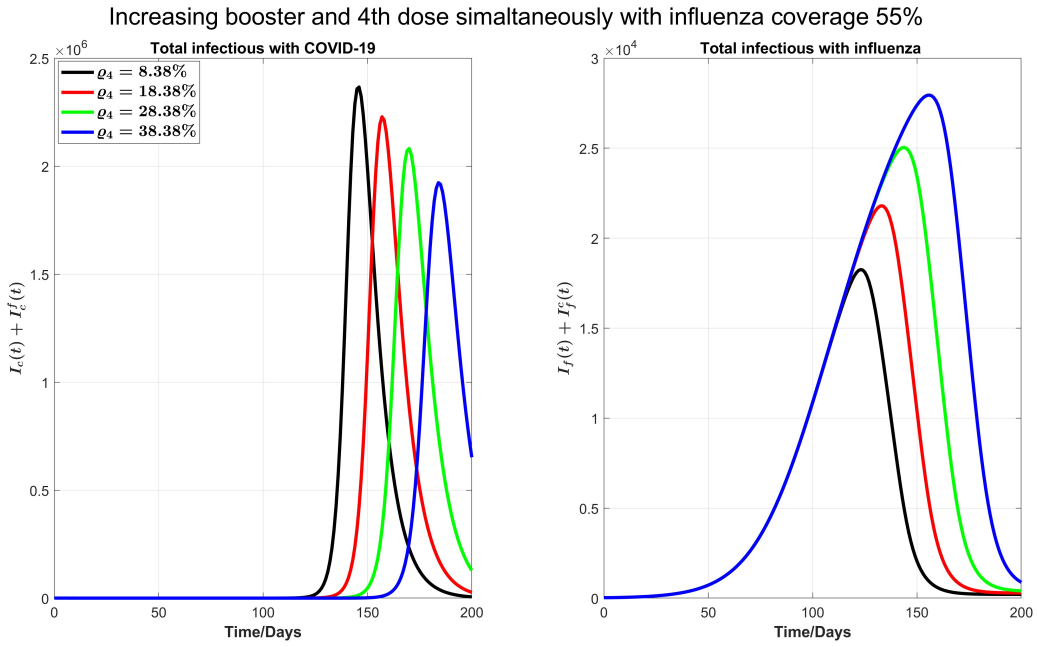

Figure 3.7: Impact of increasing coverage of COVID-19 booster (3rd dose) and 4th dose simultaneously with 55% influenza vaccine coverage on COVID-19 and influenza infections.

We also carry out some simulations to assess the impact of personal protections such as mask wearing along with increasing booster dose of COVID-19 and influenza vaccine coverage 55%. We note that mask wearing is no longer compulsory in Ontario, however mask wearing is strongly recommended. Reducing β_f and β_c by 20% as shown in Figure 3.8, there will be no COVID-19 outbreak under a variety of booster coverage, and we also see noticeable reduction in influenza cases. On the other hand, we observed through simulations result (not shown here), if influenza coverage is kept 35%, there is a high increase in influenza infections. So, we conclude that to control outbreaks of both diseases, an increase in influenza vaccine coverage and continuing the mask wearing to reduce the COVID-19 and flu transmission by 20% can play a considerable role even without increasing COVID-19 booster dose or fourth dose.

We plot some color-coded simulations to visualize the variation of total infections of

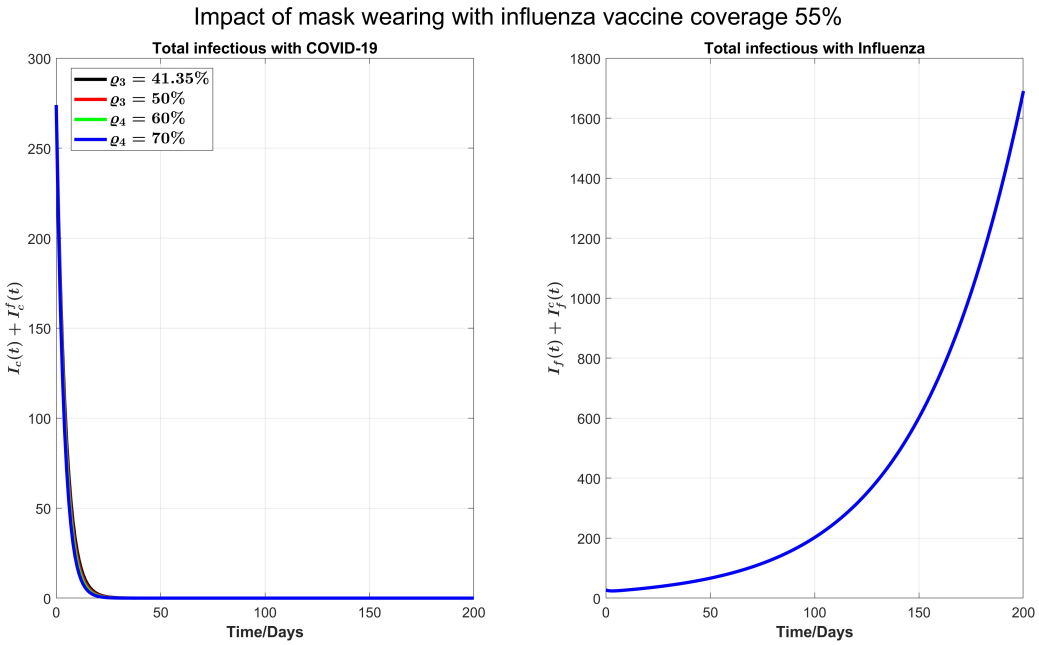

Figure 3.8: Impact of 20% mask wearing with increasing coverage of COVID-19 booster (3rd dose) and 55% influenza vaccine coverage on COVID-19 and influenza prevalence.

COVID-19 and influenza at the peak sizes and overall total infections in Figure 3.9. We vary the proportion of individuals vaccinated with the third dose of COVID-19 vaccine (horizontal axis) against the proportion vaccinated with influenza (vertical axis), and examine the impact on individuals infectious with COVID-19 ($I_c + I_c^f$), upper left panel in Figure 3.9 and influenza ($I_f + I_f^c$), right panel in Figure3.9. The peak size of individuals infectious with COVID-19 decreases with increase in both the proportion of individuals vaccinated with COVID-19 and influenza vaccines. Based on our model results, it is possible to lower the overall peak size and that of individuals infectious with COVID-19 when we vaccinate about 70% of the population with the third dose of COVID-19 vaccine, together with vaccinating about 65% of the population with influenza vaccine (see Figure 3.9 (upper left panel) and bottom panel . Alternatively, increasing the proportion of individuals vaccinated with COVID-19 and/or influenza vaccines increases the peak size of individuals infectious with influenza (see

Figure 3.9 (top right panel)). Further, by varying the same proportion of individuals with the booster dose of COVID-19 and influenza vaccine, we plot Figure 3.10, the peak time (the time when there would be maximum number of total COVID-19 infections (left panel), and total influenza infections(right panel).

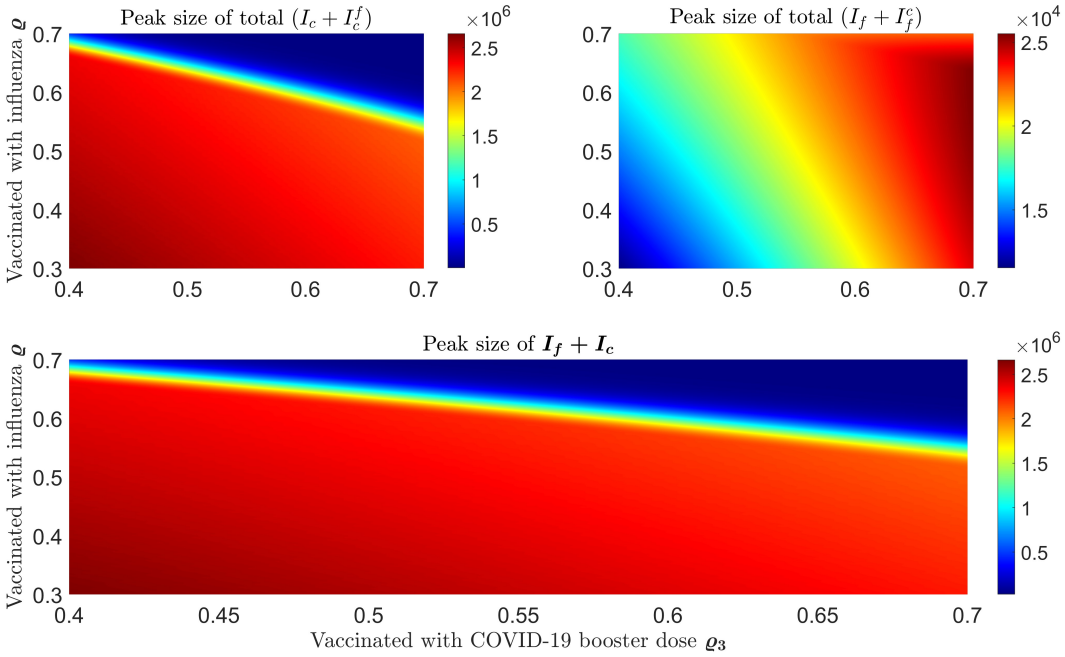

Figure 3.9: Impact of increasing proportion of individuals vaccinated with the first booster dose of COVID-19 and influenza vaccine on the peak size of infections. Top left plot represents the total number of infections with COVID-19 $(I_c(t) + I_c^f(t))$ and top right plot shows the total number of infections with influenza $(I_f(t) + I_f^c(t))$. Bottom panel shows the peak size of overall total COVID-19 and influenza cases $(I_c(t) + I_c^f(t) + (I_f(t) + I_f^c(t))$.

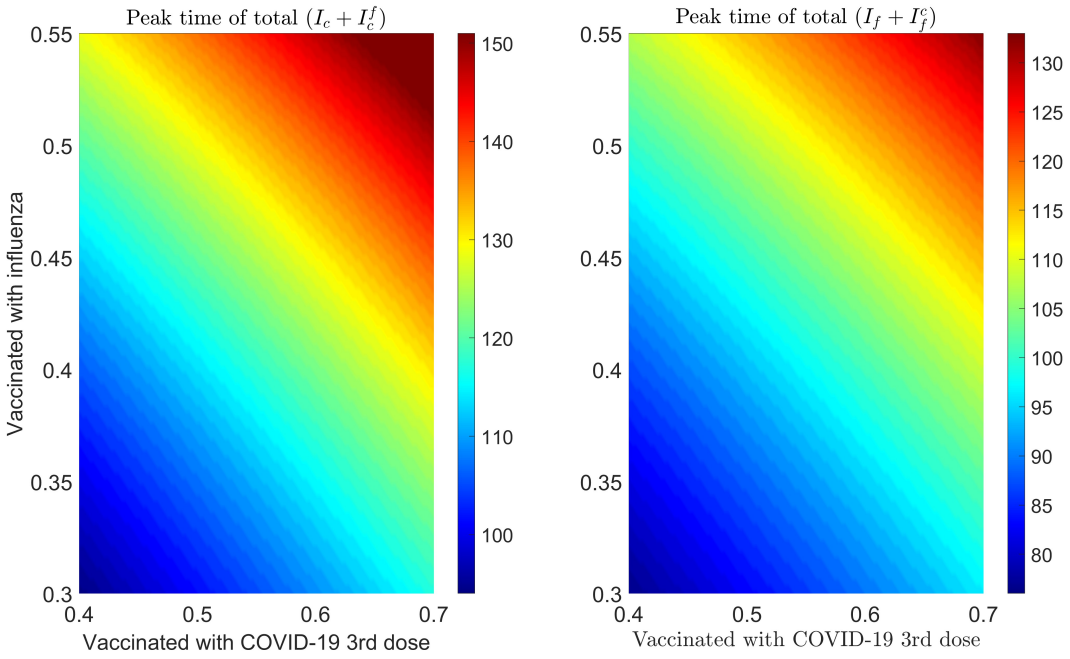

Figure 3.10: Impact of increasing proportion of individuals vaccinated with the first booster dose of COVID-19 and Influenza vaccine on the peak time of infections. Left plot represents the total number of infections with COVID-19 $(I_c(t) + I_c^f(t))$ and right plot shows the total number of infections with influenza $(I_f(t) + I_f^c(t))$.

We also consider the impact of fraction of isolation 'q' of infected individuals with influenza and COVID-19 symptoms before diagnosis. We vary this fraction from 10% - 60% to produce Figure 3.11 with influenza vaccine coverage 35% . In Figure 3.11, we can observe that the peak time for COVID-19 is postponed and peak value is reduced with increasing fraction 'q'. The peak time for influenza is also postponed, however, against the intuition, the peak number of infections with influenza for $q = 20\% - 30\%$ decreases and then increases again by increasing isolation before testing. This is because of intensive transmission rate of COVID-19 and dominance at the beginning, with much higher number of initial infections as compared to the influenza. So, after getting recovered from COVID-19 there would be more susceptible to influenza and so influenza infections starts to increase and COVID-19 infections starts to decrease. But with $q = 40\% - 60\%$, there is a substantial delay in COVID-19 peak, So,

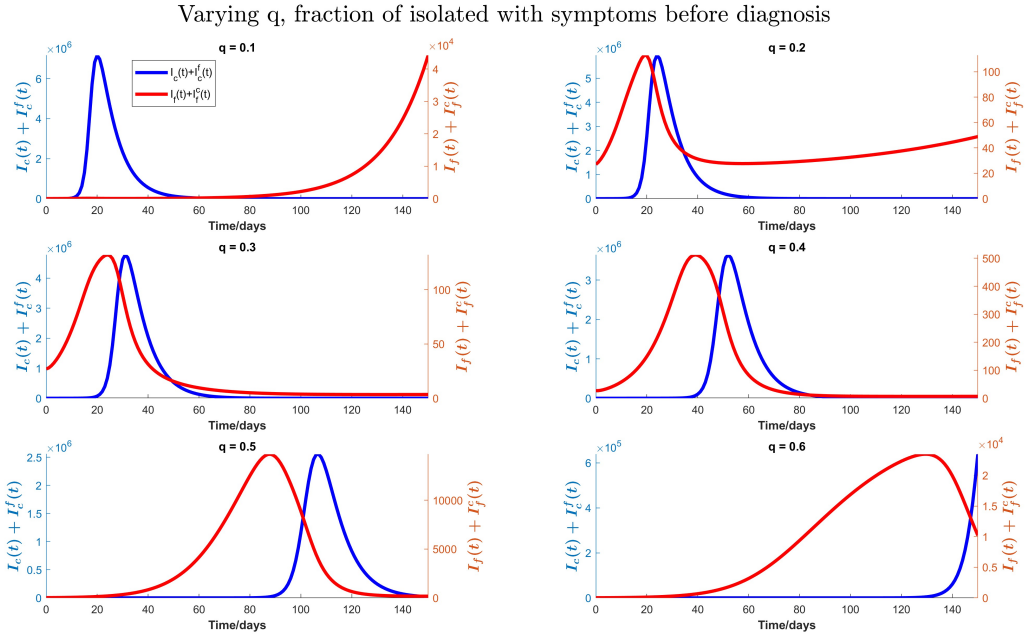

Figure 3.11: Impact of varying fraction (q) of individuals who isolate them on symptoms of influenza and COVID-19 before testing on total influenza and COVID-19 infections when influenza vaccine coverage is 35% .

more infections with influenza can be seen earlier because of more susceptible for influenza. Though, there is also a delay in influenza peak with increasing 'q'. Similar results (not shown here) are found with influenza vaccine coverage 55%.

3.3.2 Sensitivity analysis

In disease modeling, parameter uncertainty can significantly impact model outcomes, making sensitivity analysis crucial for identifying influential parameters. A common method is Latin Hypercube Sampling (LHS) combined with Partial Rank Correlation Coefficient (PRCC) [113, 114]. LHS, introduced by McKay et al. (1979)[115], samples parameters independently across stratified intervals to efficiently explore the parameter space. PRCC measures the strength and direction of monotonic relationships between parameters and outputs, assigning

values between -1 and $+1$ to indicate correlation strength. A positive PRCC value indicates a positive correlation with disease outcomes, while a negative value indicates a negative correlation.

In this study, we apply LHS/PRCC to assess the sensitivity of key epidemic outcomes relevant to public health, including the total number of infections, peak number of infections (peak magnitude), and peak time, with the goal of identifying the most influential parameters and informing control strategies for disease outbreaks. The parameters studied are: β_f, β_c, ϕ_f, ϕ_c, q and C. Monotonicity has been analysed for all the parameters sampled. Figures 3.12 and 3.13, shows the PRCC indices of these selected parameters on total number of infections 12(a), peak time 12(b) and peak number of infections 12(c) of COVID-19 and influenza respectively. Figure 3.12(a) determines that the disease transmission probabilities

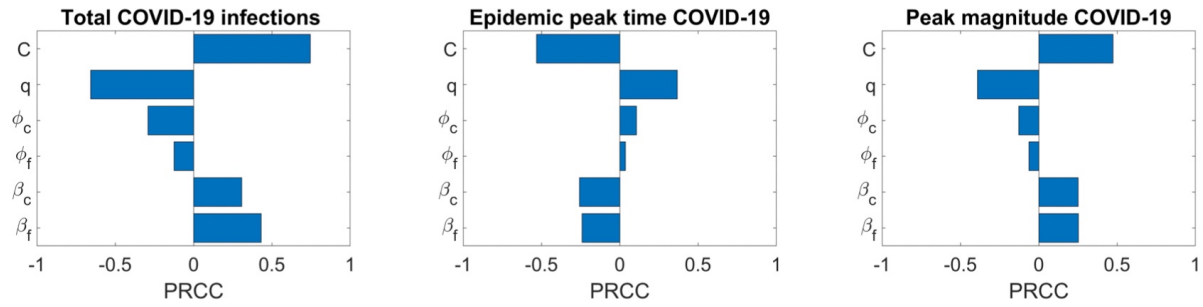

Figure 12a. **Figure 12b.** **Figure 12c.**

Figure 3.12: Sensitivity analysis of three epidemic outcomes of COVID-19. The sensitivity analysis is done with 2000 bins.

β_f, β_c, and contact rate C have positive impact, while vaccine effectiveness ϕ_f, ϕ_c and q have negative impacts. Significant positive correlation among COVID-19 infections and contact rate C and β_f, and negative correlation with COVID-19 vaccine effectiveness ϕ_c are evident. A positive correlation with β_f means more susceptible to influenza in population leading to more infections with influenza would also lead to more infections with COVID-19 because of common symptoms and delay in diagnosis. On the other hand, a strong negative correlation

of q means as much individuals on symptoms immediately isolate them less infections with COVID-19. We can also see, COVID-19 infections are less sensitive to influenza vaccine but increase in influenza coverage would reduce COVID-19 infections. This is because influenza vaccines are assumed to provide some protection against COVID-19 infection too. Figure 3.12(b) shows the effects of the PRCC indices on the peak time. The effects of these parameters are reversed, but their relative levels of influence show a similar pattern. Lastly, Figure 3(c) shows the effects of the PRCC indices on the epidemic peak size. The impacts of these parameters closely resemble to those observed in Figure 3.12(a). Next, Figure 3.13(a) shows the sensitivity of the chosen parameters to total influenza infections. Here, a strong positive co-relation of β_f and contact rate C and a significant negative co-relation of ϕ_f , β_c with total influenza infections are understandable. But a positive impact of ϕ_c on influenza infections means if there are more COID-19 booster or 4th doses are administrated (Considering booster and 4th dose because 1st dose has no and 2nd dose has very low 0.06% effectiveness against COVID-19 infection), it will result in more infections with influenza. Further, here q has a positive co-relation with Influenza infections. Similar sensitivity analysis results are obtained for influenza epidemic peak magnitude 3.13(c) and a reverse pattern for influenza peak time 3.13(b).

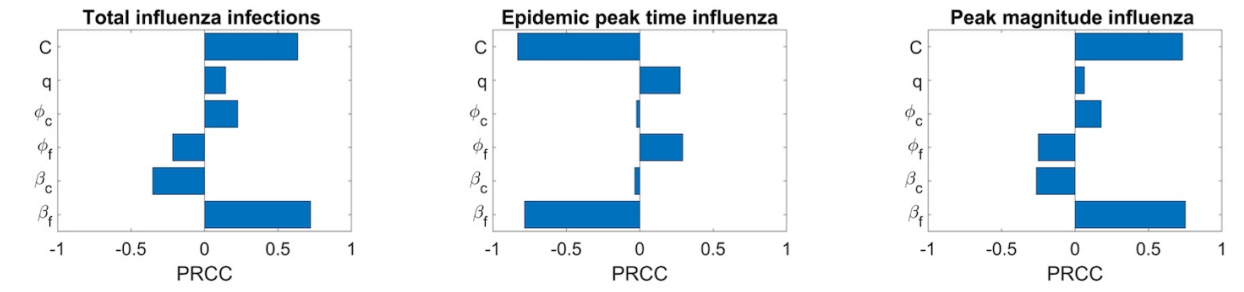

Figure 13a. **Figure 13b.** **Figure 13c.**

Figure 3.13: Sensitivity analysis of three epidemic outcomes of influenza.

3.4 Discussion

In the present study, we developed a deterministic mathematical model to describe the dynamics of COVID-19 and influenza transmission when both are present in the same season and a certain percentage of the population has received either the influenza, COVID-19, or both vaccines. Worldwide, the influenza virus, through seasonal waves of infection, generates a significant toll of cases and deaths [116]. According to the World Health Organization, before the COVID-19 pandemic, there were an estimated 1 billion cases yearly, of which 3 to 5 million were resulting in 290,000–650,000 influenza-related respiratory deaths[117]. In the Northern and Southern Hemispheres, the flu season usually runs from October to April and April to September, respectively.

COVID-19 has perturbed seasonal influenza activity [118]: in 2020 and 2021, this remained low historically at international levels [119, 120, 121, 122, 123, 124]. These changes were attributed to widespread implementation of NPIs such as physical distancing, masking requirements, and lock-downs to mitigate the transmission of SARS-CoV-2. More recently, however, and coinciding with relaxation in public health mitigation, a substantial simultaneous burden of influenza and SARS-CoV-2 has been observed in the Southern Hemisphere. The June 2022 Australian Influenza Surveillance Report reported that from mid-April 2022, the weekly number of laboratory-confirmed influenza cases in Australia had occurred earlier than usually and exceeded the 5-year average [125]. In the Northern Hemisphere, in Canada, after lifting public health measures at the beginning of March 2022, influenza virus circulation increased reaching the seasonal epidemic threshold in April with an unusual peak in May 2022[126].

Although, influenza and COVID-19 viruses belong to different families and have some differences, with SARS-Cov-2 having a much higher basic reproduction number, longer incubation period, shorter interval between symptoms onset and infectivity [127], COVID-19 shares many significant clinical and epidemiological features with influenza, such as

transmission routes and symptoms. Clinical differentiation of these two respiratory diseases can be a challenge, particularly in the early stage, based on a common diagnosis in the absence of laboratory evidence and isolation of a specific pathogen. So, a laboratory diagnostic test may be required to rule out a suspicion and establish a definitive diagnosis. Some sophisticated mathematical/statistical techniques, such as machine learning-based decision modeling approaches, have been able to distinguish between influenza and COVID-19 cases [128, 129].

In terms of clinical public and global health, even though available vaccines do not provide complete protection against infection, they can reduce the severity of the disease significantly. As influenza virus also mutates frequently, every year updated flu vaccine is required considering which strains are anticipated to circulate in the community. So, effectiveness of flu vaccine varies depending on how well the vaccine matches with circulating strains or who is being vaccinated (age or health characteristics of the vaccinated individual) [130]. According to health professionals, receiving influenza and COVID-19 vaccines are a cornerstone to protect against illness of both diseases and potentially their severe consequences, including hospitalization and fatality [131, 132].

So, reducing the burden of COVID-19 and influenza will depend primarily on increasing vaccination coverage. A mathematical model [133] has modelled the interaction between SARS-CoV-2 and influenza during the early phase of the COVID-19 pandemic. Using a population-based modelling approach, the authors found a 2–2.5-fold population-level increase in COVID-19 transmission associated with influenza co-circulation, warranting the importance of being immunized against influenza. Influenza vaccination can represent, indeed, an important public health intervention to, at least partially, relieve and mitigate against the burden generated by SARS-CoV-2 and influenza co-circulation [87]. As found by a systematic review of the literature, influenza immunization can, indeed, confer protection also against COVID-19 [134].

In our model, we took into account the multi-factorial interactions between influenza and COVID-19 in terms of additional epidemiological, clinical, and organizational burden, due to their comparable early symptoms, which can present a clinical challenge in determining the patient's disease type and overwhelm testing capacity, lowering the diagnosis rate. In this scenario, We observe that if testing capacity is increased per day, it would delay the peak of COVID-19 in addition to reducing it. On the other hand, because of early detection and lack of isolation, influenza cases can grow. Agreeing with [135], the low levels of influenza activity in the previous two years of the COVID-19 pandemic may result in an increased proportion of susceptible individuals. Our simulations with increasing influenza transmissibility show that this will bring the peak of influenza and COVID-19 earlier, slightly decrease the COVID-19 peak size, but significantly increase the flu peak. Here, we can see the real influence of co-circulation and interaction of COVID-19 and influenza on each other. It is because of the testing delay brought on by the high number of influenza cases. The earlier the flu season's peak and the greater the number of infections with flu-like symptoms, the greater the risk of flu transmission, which slows down COVID-19 testing, resulting in the delay of complete isolation of COVID-19 patients who have not been isolated before the clinical presentation of symptoms and have been continuing their normal daily activities. Further, our simulations stress the importance of vaccine uptake for preventing infection, severe illness, and hospitalization at the individual level and for disease outbreaks control at the population level to avoid putting strain on already weak and overwhelmed healthcare systems. As such, ensuring optimal vaccine coverage for COVID-19 and influenza to reduce the burden of these infections is paramount. We showed that by keeping the influenza vaccine coverage about 35% and increasing the coverage of booster or 4th dose of COVID-19 not only reduces the infections with COVID-19 but also can delay its peak time. If the influenza vaccine coverage is increased to 55%, unexpectedly, it increases the peak size of influenza infections slightly, while it reduces the peak size of COVID-19 as well as significantly delays the peaks

of both of these diseases. Also, we have shown that personal protection decision like mask wearing can mitigate the COVID-19 outbreak and can avert an outbreak of seasonal influenza significantly. In conclusion, increase in vaccine uptake of both diseases particularly influenza can significantly delay the peak time of both COVID-19 and influenza. Mask wearing coupled with a moderately increase in the vaccine uptake may mitigate COVID-19 and prevent an influenza outbreak. However, there are some limitations in the current study. To keep this model parsimonious, we did not include latent or asymptomatic stages of infection. We believe including these stages would not overly affect our predictions, due to the majority of COVID-19 and flu cases being symptomatic, and therefore requiring diagnosis [136]. Future study may be extended to add these states if needed. Also, We didn't consider outflow from the isolation class (before testing) to the recovered class because of the long delay in diagnosis. Though we did some simulations by incorporating it into our model (not included here because of limitations of figures in the Journal) and observed that there is not much difference between these and our key findings of the given model in this study, except we see more delay in peak times of both diseases and by increasing influenza vaccine coverage from 35% to 55% there is a decay in influenza cases instead of a slight increase in influenza peak as in our original model. Also, with 55% influenza vaccine along with 20% masking, there would be no any outbreak of COVID-19 and influenza even if booster and fourth dose coverage are kept moderate.

Our study has important practical implications for public health policy, in that it shows that effectively managing and controlling both influenza and COVID-19 outbreaks taking place during the same season depends on ensuring optimal strategies in terms of vaccine coverage and personal protection like mask wearing.

Chapter 4

A Mathematical Epidemic Model with Delay in the Removal Rate

4.1 Introduction

This chapter focuses on analyzing the occurrence, direction and stability of a Hopf bifurcation of periodic solutions in an epidemic model with a fixed time delay. In classical epidemic models, the per capita transmission rate, incidence rate or removal rate is assumed to be a constant. This assumption simplifies mathematical analysis but neglects critical real-world complexities such as resource constraints in healthcare systems. Therefore, several studies have been conducted to consider the nonlinear incidence rate and removal rate in terms of the treatment rate for disease transmission dynamics, see [137, 138, 139] and references therein. Furthermore, as resources are used and the number of infections increases, the removal rate is likely to decrease. Thus, a more practical approach would involve a variable removal rate that adapts to different stages of the epidemic. A more realistic approach considers the removal rate as a dynamic quantity that depends on the health system's capacity to diagnose and isolate infectious individuals. This dependency becomes particularly significant during

an outbreak when testing resources are limited, leading to delays in diagnosis and isolation. Previous studies (for example, [140, 141]) have examined epidemic models in which the removal rate depends on the number of infections and incorporated nonlinear incidence rates to account for behavioral and epidemiological factors. Furthermore, research has considered delays due to latency periods, immunity durations, and behavioral adaptations [142, 143, 144, 145] . However, to our knowledge, no study has explicitly investigated Hopf bifurcations in an epidemic model where the removal rate depends on infections with incorporated time delay. In this work, we propose a simple SIR-type model with a nonlinear removal rate that is a function of infections and incorporates a delay term. The inclusion of a time delay in the removal rate is critical for accurately modeling the dynamics of infectious diseases. In real situations, there can be a natural delay between the onset of infection, the emergence of symptoms, the completion of testing, and the initiation of isolation measures. This delay varies according to factors such as the efficiency of the testing infrastructure, public awareness, and the availability of healthcare resources. By explicitly modeling this delay, the time-dependent nature of the removal process is more accurately represented. Furthermore, it may introduce a delay in the feedback mechanism that controls the spread of the disease, which can destabilize the steady-state behavior of the system or result in oscillatory dynamics, leading to recurrent waves of infection. During an outbreak, healthcare systems often face resource constraints, particularly in testing capacity. When the number of infected individuals exceeds the threshold capacity of the system, delays in testing and diagnosis increase, causing more individuals to remain infectious for longer periods. Incorporating a time delay in the removal rate function captures this critical feedback loop, where resource limitations exacerbate the spread of the disease and contribute to the complexity of epidemic dynamics.

4.2 Model Formulation

To account for these delays, here we propose a simple SIR model for the outbreak of an

infectious disease by incorporating a constant time-dependent removal rate, denoted by γ, which depends on the number of infected individuals, $I(t)$, with a time delay τ. This delay reflects the time required for diagnosis and subsequent/initiation of isolation. The removal rate is represented by $\gamma(I(t-\tau))$, where τ accounts for the delay between infection and isolation. If an infectious individual is not diagnosed within the average recovery period, they will be removed from the infectious class naturally after that time. Furthermore, we assume that the function γ exhibits a bell-shaped dependence on the number of infected individuals, reflecting the saturation of healthcare resources as the infection burden increases.

In the case of an outbreak, initially, infected people recover and are removed from the infectious class at an average recovery rate. Later, they are quickly tested, removed, and isolated. However, when the number of infected individuals reaches a certain number or threshold (I_c) of available resources for testing/diagnosis, the removal rate starts to decrease as the number of infected individuals increases. In this context, it is natural to assume that γ is an increasing function on the interval $[0, I_c]$ and decreases for $I > I_c$. As the number of new infectious cases grows significantly, the available resources for testing and diagnosis become insufficient to handle the increasing demand for testing necessary for diagnosis and early isolation, resulting in the possibility that a certain number of infectious individuals will be removed only after average recovery days. A minimum removal rate will be sustained, that is, $\lim_{I\to\infty}\gamma(I) = \gamma_1$, where γ_1 is the minimum per capita removal rate. Therefore, we consider a nonlinear removal rate function γ of the form

$$\gamma(I) = \gamma_1 + (\gamma_0 - \gamma_1)e^{-k(I-I_c)^2}, \;\; I > 0,$$

where γ_0 is the maximum removal rate of infected individuals and I_c is a test resource threshold. Note that I is a function of delay, that is, $I(t-\tau)$.

We can also consider γ in the form of a piece-wise function such as

$$\gamma(I) = \begin{cases} \frac{(\gamma_0 - \gamma_1)}{I_c} I + \gamma_1, & \text{if } I \leq I_c, \\ \gamma_1 + (\gamma_0 - \gamma_1) e^{-k(I - Ic)}, & \text{if } I > I_c. \end{cases} \tag{4.1}$$

We consider the situation in which public health interventions, reflected in the behavioral changes of the population, such as social distancing and personal protection, as well as the rapid removal of infectious individuals through testing and diagnosis, are implemented to prevent a large portion of infections before herd immunity is achieved. Therefore, the susceptible population remains relatively unchanged, and the SIR model reduces accordingly.

$$I'(t) = \beta S_0 I(t) - \gamma(I(t - \tau)) I(t), \tag{4.2}$$

where $I(t)$ is the state variable infected population, β is the transmission rate, S_0 is the susceptible population at equilibrium. Our model 4.2 appears structurally very similar to the classical delayed logistic model; however, there is a significant difference in their underlying mechanisms and applications. The delayed logistic model typically takes the form $N'(t) = bN(t) - dN(t - \tau)N(t)$, with a linear removal term that depends on the delayed population size. In contrast, our epidemic model incorporates a state-dependent nonlinear removal term $\gamma(I(t - \tau))I(t)$, where $\gamma(\cdot)$ is a bell-shaped function reflecting a realistic state-dependent removal rate that varies with the number of infections. Specifically, the removal rate increases with the number of infections up to a critical threshold due to more effective testing and isolation efforts when cases are moderate, but declines beyond this threshold as healthcare resources become saturated. Although the delayed logistic model and its alternative formulations [146, 147, 148] are well studied in ecology, our model introduces a novel, biologically motivated mechanism specific to epidemics, where delayed diagnosis and isolation contribute directly to outbreak dynamics.

4.3 Equilibria, Linearization and Stability Analysis

Model (4.2) has one disease free equilibrium $I^* = 0$ and zero, one, or two positive endemic equilibrium points defined implicitly by the equation

$$\beta S_0 = \gamma(I^*). \tag{4.3}$$

Moreover, the basic reproduction number is given by $R_0 = \frac{\beta S_0}{\gamma(0)}$.

In this subsection, we focus on analyzing the Hopf bifurcation of periodic solutions from the disease-endemic equilibria, by considering τ as the bifurcation parameter. We consider that the particular function γ is given by $\gamma(I) = \gamma_1 + (\gamma_0 - \gamma_1)e^{-k(I-I_c)^2}$ and assume $\gamma_0 > \beta S_0 > \gamma_1$, which allows us to conclude the existence of at least one positive endemic equilibrium. To analyze stability of the equilibrium, we linearize the system around an equilibrium point I^*. The linearized equation is

$$I'(t) = (\beta S_0 - \gamma(I^*))I^* - \gamma'(I^*)I^* I(t-\tau). \tag{4.4}$$

From (4.3), at a positive endemic equilibrium, the first term on the right side of (4.4) is zero, and it can be rewritten as

$$I'(t) = -\gamma'(I^*)I^* I(t-\tau). \tag{4.5}$$

Now, considering the solutions of the form $I(t) = qe^{\lambda t}$ and substituting into the linearized equation, we obtain the characteristic equation

$$\Delta(\lambda, \tau) = \lambda + \gamma'(I^*)I^* e^{-\lambda\tau} = 0, \tag{4.6}$$

which is a transcendental equation, meaning it involves exponential terms and cannot be solved algebraically in a simple way. For stability analysis, we analyze the two cases:

(i) Case 1. $R_0 \leq 1$: that is, $\gamma(0) \geq \beta S_0$. We can see that there exists an unique positive endemic equilibrium $I^* > 0$. Moreover, $I^* > I_c$ and $\gamma'(I^*) < 0$. Therefore, using equation (4.6), for all $\tau > 0$, its stability can be graphically analyzed considering the intersection of two functions: the linear function λ and the non-linear function $-\gamma'(I^*)I^*e^{-\lambda\tau}$. The function (λ) is a straight line passing through the origin with a slope of 1, while $-\gamma'(I^*)I^*e^{-\lambda\tau}$ starts at $-\gamma'(I^*)I^*$ when $\lambda = 0$ and decays exponentially toward zero as $\lambda \to \infty$. The equilibrium's stability depends on whether these two functions intersect at a positive or negative λ. Since, $\gamma'(I^*) < 0$ there exists a positive real number $\lambda(\tau) > 0$ such that $\Delta(\lambda(\tau), \tau) = 0$, which allows us to conclude that I^* is unstable.

(ii) Case 2. $R_0 > 1$: that is, $\gamma(0) < \beta S_0$. In this case, we obtain that there exist two positive endemic equilibria $I_1^*, I_2^* > 0$. Moreover, $I_1^* < I_c < I_2^*$ and $\gamma'(I_2^*) < 0 < \gamma'(I_1^*)$. Using the discussions above, we can conclude that I_2^* is unstable.

From equation (4.6), for λ at $I^* = I_1^*$, graphically, we can see at I_1^*, $\gamma'(I^*) > 0$ there is no intersection, so no real eigenvalue exists at this I_1^*, which implies that all eigenvalues must be complex. First,we notice that when $\tau = 0$, the characteristic equation becomes $\lambda + \gamma'(I^*)I^*$ the eigenvalue $\lambda = -\gamma'(I^*)I^* < 0$ is a negative real number. We seek conditions on τ, such that $Re\lambda$, changes from negative to positive. By the continuity, if λ changes from $-\gamma'(I^*)I^* < 0$ to a value such that $Re\lambda > 0$ when τ increases, there must be some value of τ, say τ^*, at which $Re\lambda = 0$. In other words, the characteristic equation must have a pair of purely imaginary roots.

By assuming $\lambda = i\omega$, $\omega > 0$, in the characteristic equation and separating real and imaginary parts, we obtain

$$\begin{aligned} \gamma'(I^*)I^* cos(\omega\tau) &= 0, \\ \omega - \gamma'(I^*)I^* sin(\omega\tau) &= 0. \end{aligned} \tag{4.7}$$

Solving first of these equations for τ gives $cos(\omega\tau) = 0$. This gives $\tau = \frac{(2n+1)\pi}{2\omega}$, for $n \in Z$, In second equation, by replacing $\omega\tau = \frac{\pi}{2} + n\pi$, we have

$$\omega = \gamma'(I^*)I^* sin(\frac{\pi}{2} + n\pi).$$

Since, $sin(\frac{\pi}{2} + n\pi) = (-1)^n$, we get $\omega = \gamma'(I^*)I^*(-1)^n$. For $\omega > 0$, we will consider the case depending on $\gamma'(I^*)I^*$. If $\gamma'(I^*)I^* > 0$, then for even n, $\omega = \gamma'(I^*)I^*$. Thus

$$\tau = \frac{(2n+1)\pi}{2\gamma'(I^*)I^*}$$

Hence, $\frac{(2n+1)\pi}{2\gamma'(I^*)I^*}$ are critical values of τ. By considering the smallest critical value for $n = 0$,

$$\tau = \tau^* = \frac{\pi}{2\gamma'(I^*)I^*} = \frac{\pi}{2\omega}.$$

Thus, when $\tau = \tau^*$, (4.6) has pure imaginary roots. Further, let $I^* = I_1^*$ and assume that $\lambda = \alpha + i\omega$ is a complex solution of the characteristic equation (4.6) at I^* and $\alpha > 0$. It gives

$$\alpha + i\omega = -\gamma'(I^*)I^* e^{-(\alpha+i\omega)\tau}.$$

Separating the real and the imaginary parts, we have that

$$\begin{aligned} \alpha &= -\gamma'(I^*)I^* e^{-\alpha\tau} cos(\omega\tau), \\ \omega &= \gamma'(I^*)I^* e^{-\alpha\tau} sin(\omega\tau). \end{aligned} \tag{4.8}$$

The first of these equations implies that $\omega > \frac{\pi}{2\tau}$ and the second implies that $\omega < \frac{\pi}{2\tau}$, which gives a contradiction. Hence λ is a complex eigenvalue with a negative real root. It shows that $I_1^* < I_c$ is a stable equilibrium.

The system of equation (4.8) is well known [1] and the following result contains the relevant information regarding the stability for this case.

Lemma 1. *Let $I^* > 0$ be a positive endemic equilibrium such that $\gamma'(I^*) > 0$ and $\tau \geq 0$.*

(i) If $0 \leq \gamma'(I^*)I^*\tau < \frac{\pi}{2}$, then I^* is stable.

(ii) If $\gamma'(I^*)I^*\tau > \frac{\pi}{2}$, then I^* is unstable.

(iii) If $\gamma'(I^*)I^*\tau = \frac{\pi}{2}$, then a Hopf bifurcation occurs at (I^*), i.e., periodic solutions bifurcate from (I^*).

4.3.1 Tranversality condition

The transversality condition requires that $\mathrm{Re}\left(\frac{d\lambda}{d\tau}|_{\lambda=i\omega,\tau=\tau^*}\right) \neq 0$, ensuring that the real part of the eigenvalue crosses the imaginary axis, indicating a change in stability. Differentiating equation (4.6) w.r.t τ, we have

$$0 = \frac{\partial}{\partial\tau}\Delta(\lambda(\tau),\tau) = \frac{\partial\Delta}{\partial\lambda}(\lambda(\tau),\tau)\frac{d\lambda(\tau)}{d\tau} + \frac{\partial\Delta}{\partial\tau}(\lambda(\tau),\tau). \tag{4.9}$$

We obtain that

$$\mathrm{Re}\left(\frac{d\lambda}{d\tau}|_{\lambda=i\omega,\tau=\tau^*}\right) = \mathrm{Re}\left(\frac{-\frac{\partial\Delta}{\partial\tau}(i\omega,\tau^*)}{\frac{\partial\Delta}{\partial\lambda}(i\omega,\tau^*)}\right). \tag{4.10}$$

By taking $b = \gamma'(I^*)I^*$ and replacing $w^{=}b$, $\tau^* = \frac{\pi}{2b}$, we get

$$\frac{\partial\Delta}{\partial\tau}(i\omega,\tau^*) = -b^2,$$

and

$$\frac{\partial\Delta}{\partial\lambda}(i\omega,\tau^*) = 1 + i\frac{\pi}{2}.$$

[1] [147]

After replacing these values in equation (4.10), we get

$$\mathrm{Re}\left(\frac{d\lambda}{d\tau}|_{\lambda=i\omega,\tau=\tau^*}\right) = \frac{b^2}{1+\pi/2} \neq 0. \tag{4.11}$$

Therefore, we conclude that the transversality condition holds and Hopf bifurcation occurs at $\omega = \omega^*$, $\tau = \tau^*$.

4.4 Direction of Hopf Bifurcation

In the last section, we obtained a condition under which the system undergoes Hopf bifurcation at τ^* that is, a family of periodic solutions bifurcate from the positive endemic steady state point at the critical value τ^*. Our goal in this section is to determine the direction of Hopf bifurcation, that is, to ensure whether the bifurcating branch of periodic solution exists locally for $\tau > \tau^*$ or $\tau < \tau^*$. In this section, we study the direction and stability of the bifurcating periodic solutions at $\tau = \tau^*$.

We assume $i\omega^*$ is the corresponding purely imaginary root of the characteristic equation of the linearized equation at the positive equilibrium. The method we used is based from Hassard et. al book [148].

For notational convenience, let $\tau = \tau^* + \mu$, where $\mu \in R$. So that $\mu = 0$ is the Hoph bifurcation value of (4.2). Let $x(t) = I(\tau t) \implies x'(t) = \tau I'(\tau t)$, which allows to obtain that

$$x'(t) = \tau(\beta S_0 - \gamma(x(t-1))x(t). \tag{4.12}$$

Writing $y(t) = I(t-1)$, the gamma function of y becomes

$$\begin{aligned} \gamma(y) &= \gamma_1 + (\gamma_0 - \gamma_1)e^{-k(y-I_c)^2}, \\ &= \gamma_1 + (\gamma_0 - \gamma_1)e^{-kI_c^2}e^{2kI_c y}e^{-ky^2}. \end{aligned} \tag{4.13}$$

Using that the exponential function can be written as $e^x = \sum_{n=0}^{\infty} \frac{x^n}{n!}$, we can obtain

$$e^{2kI_c y} = 1 + 2kI_c y + 2k^2 {I_c}^2 y^2 + \mathcal{O}(3),$$

$$e^{-ky^2} = 1 - ky^2 + \mathcal{O}(4),$$

$$e^{2kI_c y} e^{-ky^2} = 1 + 2kI_c y + (2k^2 {I_c}^2 - k)y^2 + \mathcal{O}(3).$$

So, equation (4.12) becomes

$$\begin{aligned}
x'(t) &= \tau\beta S_0 x(t) - \tau\left(\gamma_1 + (\gamma_0 - \gamma_1)e^{-kI_c^2}(1 + 2kI_c y(t) + (2k^2 {I_c}^2 - k)y^2(t) + \mathcal{O}(3))\right)x(t), \\
&= \tau\beta S_0 x(t) - \tau(\gamma_1 + (\gamma_0 - \gamma_1)e^{-kI_c^2}x(t) - \tau(\gamma_0 - \gamma_1)e^{-kI_c^2}2kI_c y(t)x(t) \\
&- \tau(\gamma_0 - \gamma_1)e^{-kI_c^2}(2k^2 {I_c}^2 - k)y^2(t)x(t) + \mathcal{O}(4), \\
&= \tau(\beta S_0 - \gamma(0))x(t) - \tau(\gamma_0 - \gamma_1)e^{-kI_c^2}2kI_c x(t-1)x(t) \\
&- \tau(\gamma_0 - \gamma_1)e^{-k(I_c)^2}(2k^2 I_c^2 - k)x(t-1)^2 x(t) + \mathcal{O}(4).
\end{aligned} \tag{4.14}$$

Using that $R_0 = \frac{\beta S_0}{\gamma(0)}$ and defining $R_1 = k(\gamma_0 - \gamma_1)e^{-k(I_c)^2}$, equation (4.14) can rewritten as

$$\begin{aligned}
x'(t) &= \tau\gamma(0)(R_0 - 1)x(t) - \tau 2R_1 I_c x(t-1)x(t) - \tau R_1(2kI_c^2 - 1)x(t-1)^2 x(t) + \mathcal{O}(3), \\
&= L_\tau x_t + F(x_t, \tau),
\end{aligned} \tag{4.15}$$

where the linear operator $L_\tau : C \to R$ and function $F : C \times R \to R$ are defined by

$$L_\tau \phi = \tau\gamma(0)(R_0 - 1)\phi(0),$$

and

$$F(\phi, \tau) = -\tau 2R_1 I_c \phi(-1)\phi(0) - \tau R_1(2kI_c^2 - 1)\phi(-1)^2\phi(0) + \mathcal{O}(4).$$

Where

Using that $\Delta(\lambda,\tau)=\lambda+\gamma'(I^*)I^*e^{-\lambda\tau}$, we obtain $D_1\Delta(\lambda,\tau)=1-\gamma'(I^*)I^*\tau e^{-\lambda\tau}$ and $D_1\Delta(iw^*,\tau^*)=1-\frac{\pi}{2}e^{-i\frac{\pi}{2}}=1+i\frac{\pi}{2}$. Let $q=\frac{1}{D_1\Delta(iw^*,\tau^*)}=\frac{1}{1+i\frac{\pi}{2}}=\frac{1-i\frac{\pi}{2}}{1+\frac{\pi^2}{4}}$, and $g(z,\overline{z})=qg_0(z,\overline{z})$, where $g_0(z,\overline{z})=F(w+z\phi+\overline{z}\overline{\phi},\tau)$.

Using the algorithm in [148] to obtain the direction of the bifurcation, we need to determine the sign of C given by

$$C=\frac{i}{2\omega_0}(g_{20}g_{11}-2|g_{11}|^2-\frac{1}{3}|g_{02}|^2)+\frac{g_{21}}{2},$$

where $g(z,\overline{z})=\sum_{i+j\geq 2}g_{ij}z^i\overline{z}^j$.

$$g_0(z,\overline{z}) \;=\; g_{20}\frac{z^2}{2}+g_{11}z\overline{z}+g_{02}\frac{\overline{z}^2}{2}+g_{21}\frac{z^2\overline{z}}{2}+... \tag{4.16}$$

Using the above, we have

$$\begin{aligned} g_0(z,\overline{z}) &= F(w+z\phi+\overline{z}\overline{\phi},\tau),\\ &= -2\tau R_1 I_c\left(w(-1)+z\phi(-1)+\overline{z}\overline{\phi}(-1)\right)\left(w(0)+z\phi(0)+\overline{z}\overline{\phi}(0)\right)-\tau R_1(2k{I_c}^2-1)\\ &\quad \left(w(-1)+z\phi(-1)+\overline{z}\overline{\phi}(-1)\right)^2\left(w(0)+z\phi(0)+\overline{z}\overline{\phi}(0)\right)+\mathcal{O}(4). \end{aligned} \tag{4.17}$$

Let $R_2=2R_1I_c$ and $R_3=R_1(2k{I_c}^2-1)$ in equation (4.17) and replacing $\phi(-1)=e^{-i\omega}$, $\overline{\phi}(-1)=e^{i\omega}$, $\phi(0)=1$ and $\overline{\phi}(0)=1$, we get

$$\begin{aligned} g_0(z,\overline{z}) &= -R_2\tau\left(w(-1)+ze^{-i\omega}+\overline{z}e^{i\omega}\right)(w(0)+z+\overline{z})\\ &- R_3\tau\left(w(-1)+ze^{-i\omega}+\overline{z}e^{i\omega}\right)^2(w(0)+z+\overline{z}). \end{aligned} \tag{4.18}$$

Next, from equation (4.18), we obtain that

$$\left(w(-1)+ze^{-i\omega^*}+\overline{z}e^{i\omega^*}\right)(w(0)+z+\overline{z}) \;=\; 2e^{-i\omega^*}\frac{z^2}{2}+(e^{-i\omega^*}+e^{i\omega^*})z\overline{z}+2e^{i\omega^*}\frac{\overline{z}^2}{2}+z(w(-1)$$

$$+ \quad e^{-i\omega^*}w(0)) + \overline{z}(w(-1) + e^{i\omega^*}w(0)) \tag{4.19}$$

,

and

$$\begin{aligned}\left(w(-1) + ze^{-i\omega} + \overline{z}e^{i\omega}\right)^2 (w(0) + z + \overline{z}) &= (e^{-i\omega^*}z + e^{i\omega^*}\overline{z})^2 (w(0) + z + \overline{z}) + \mathcal{O}(3) \\ &= (e^{-2i\omega^*}z^2 + 2z\overline{z} + e^{2i\omega^*}\overline{z}^2)(z + \overline{z}) + \mathcal{O}(3) \\ &= (e^{-2i\omega^*} + 2)z^2\overline{z} + \mathcal{O}(3). \end{aligned} \tag{4.20}$$

Replacing equations (4.19) and (4.20) in (4.18), we get

$$\begin{aligned} g_0(z,\overline{z}) &= -R_2\tau\left(2e^{-i\omega^*}\frac{z^2}{2} + (e^{-i\omega^*} + e^{i\omega^*})z\overline{z} + 2e^{i\omega^*}\frac{\overline{z}^2}{2}\right) \\ &\quad -R_2\tau(z(w(-1) + e^{-i\omega^*}w(0)) + \overline{z}(w(-1) + e^{i\omega^*}w(0))) \\ &- \quad R_3\tau(e^{-2i\omega^*} + 2)z^2\overline{z} + \mathcal{O}(3). \end{aligned} \tag{4.21}$$

Further, for $g(z,\overline{z}) = qg_0(z,\overline{z})$

$$\begin{aligned} g_{20} &= -2\tau R_2 e^{-i\omega *}q, \\ g_{11} &= -\tau R_2(e^{-i\omega *} + e^{i\omega *})q = -2\tau R_2\cos(\omega *)q, \\ g_{02} &= -2\tau R_2 e^{i\omega *}q, \end{aligned} \tag{4.22}$$

and

$$\frac{g_{21}}{2} = \frac{1}{2}\left[-R_2\tau((w_{11}(-1) + e^{-i\omega^*}w_{11}(0)) + (w_{20}(-1) + e^{i\omega^*}w_{20}(0))) - R_3\tau(e^{-2i\omega^*} + 2)\right]q. \tag{4.23}$$

In addition,

$$H(z,\overline{z})(\theta) = \begin{cases} -g(z,\overline{z})\phi(\theta) - \overline{g(z,\overline{z})}\phi(\overline{\theta}), & \text{if } -1 \leq \theta < 0, \\ -g(z,\overline{z})\phi(0) - g(z,\overline{z})\phi(\overline{0}) + g_0(z,\overline{z}). & \text{if } \theta = 0, \end{cases} \tag{4.24}$$

So,

$$\begin{aligned} H(0) &= -g(z,\overline{z})\phi(0) - g(z,\overline{z})\phi(\overline{0}) + g_0(z,\overline{z}) \\ &= -2Re(g(z,\overline{z})) + g_0(z,\overline{z}). \end{aligned} \tag{4.25}$$

$$\begin{aligned} H_{20}(0) &= -2Re(g_{20}) + g_{20}^0, \\ &= \frac{4\tau R_2(\cos\omega^* - \frac{\pi}{2}\sin\omega^*)}{1+\frac{\pi^2}{4}} - 2\tau R_2 e^{-i\omega *}. \end{aligned} \tag{4.26}$$

$$\begin{aligned} H_{11}(0) &= -2Re(g_{11}) + g_{11}^0 \\ &= \frac{4\tau R_2 \cos\omega^*}{1+\frac{\pi^2}{4}} - 2\tau R_2 \cos\omega^*. \end{aligned} \tag{4.27}$$

Next,

$$A(\phi)(\theta) = \begin{cases} \phi'(\theta), & \text{if } -1 \leq \theta < 0, \\ L\phi & \text{if } \theta = 0. \end{cases} \tag{4.28}$$

In this case, we have

$$A(\phi)(\theta) = \begin{cases} \phi'(\theta), & \text{if } -1 \leq \theta < 0 \\ \tau(\beta S_0 - \gamma(0)\phi(0) & \text{if } \theta = 0, \end{cases} \tag{4.29}$$

and

$$\begin{aligned} H_{20} &= (2iw - A)W_{20}, \\ H_{11} &= -AW_{11}. \end{aligned} \tag{4.30}$$

First equation of (4.30) implies that

$$\begin{aligned} 2i\omega^* W_{20}(\theta) - \frac{d}{d\theta}W_{20}(\theta) = H_{20}(\theta) \quad \text{if } -1 \leq \theta < 0, \\ (2i\omega^* - \tau(\beta S_0 - \gamma(0)))W_{20}(0) = H_{20}(0) \qquad \text{if } \theta = 0. \end{aligned} \tag{4.31}$$

First equation of (4.31) can be written as

$$\frac{d}{d\theta}(e^{-2i\omega^*\theta}W_{20}(\theta)) = -e^{-2i\omega^*\theta}H_{20}(\theta), \tag{4.32}$$

which gives after integration

$$W_{20}(0) - e^{2i\omega^*}W_{20}(-1) = -\int_{-1}^{0} e^{-2i\omega^*\theta}H_{20}(\theta)d\theta, \tag{4.33}$$

where,

$$\begin{aligned} H_{20}(\theta) &= -2Re(g_{20}\phi(\theta)) \\ &= -2Re(-2\tau R_2 e^{-i\omega *}(\frac{1 - i\frac{\pi}{2}}{1 + \frac{\pi^2}{4}})e^{i\omega^*\theta}) \\ &= 4\tau R_2 \frac{(\cos(\omega^*(\theta - 1)) + \frac{\pi}{2}\sin(\omega^*(\theta - 1)))}{1 + \frac{\pi^2}{4}}. \end{aligned} \tag{4.34}$$

Now,

$$-AW_{11}(\theta) = H_{11}(\theta),$$

implies that

$$\begin{aligned} \frac{d}{d\theta}W_{11}(\theta) &= H_{11}(\theta) \quad \text{if } -1 \leq \theta < 0, \\ LW_{11} &= H_{11}(0) \qquad \text{if } \theta = 0, \end{aligned} \tag{4.35}$$

with

$$\begin{aligned} H_{11}(\theta) &= -2Re(g_{11}\phi(\theta)), \\ &= Re(2\tau R_2 cos(\omega^*)(\frac{1-i\frac{\pi}{2}}{1+\frac{\pi^2}{4}})e^{iw\theta}), \\ &= \frac{2\tau R_2 \cos\omega^*(\cos\omega^*\theta + \frac{\pi}{2}\sin\omega^*\theta)}{1+\frac{\pi^2}{4}}. \end{aligned} \tag{4.36}$$

Equation (4.35) implies that

$$\begin{aligned} W_{11}(0) - W_{11}(-1) &= \int_{-1}^{0} H_{11}(\theta)d\theta, \\ \tau(\beta S_0 - \gamma(0))W_{11}(0) &= H_{11}(0). \end{aligned} \tag{4.37}$$

Using the values of $H_{20}(0)$,$H_{11}(0)$ and $H_{20}(\theta)$ from equations (4.26), (4.27) and (4.34), respectively, we can calculate $W_{11}(0)$, $W_{11}(-1)$, $W_{20}(-1)$ and $W_{20}(0)$.
By replacing the value of $H_{20}(0)$ from (4.26) into the second equation of (4.31), we get

$$W_{20}(0) = \frac{1}{2iw^* - \tau(\beta S_0 - \gamma(0))}\left(\frac{4\tau R_2(\cos\omega^* - \frac{\pi}{2}\sin\omega^*)}{1+\frac{\pi^2}{4}} - 2\tau R_2 e^{-i\omega^*}\right). \tag{4.38}$$

Furthermore, by replacing the value of $H_{20}(\theta)$ from equation (4.31) in (4.33) and using $W_{20}(0)$, we can get value of $W_{20}(-1)$:

$$W_{20}(-1) = e^{-2iw^*}W_{20}(0) + \int_{-1}^{0} e^{-2i\omega^*(\theta+1)}H_{20}(\theta)d\theta. \tag{4.39}$$

Using, $\sin(x) = \frac{e^{ix}-e^{-ix}}{2i}$ and $\cos(x) = \frac{e^{ix}+e^{-ix}}{2}$, we can see that

$$e^{-2iw^*}W_{20}(0) = \frac{1}{2iw^* - \tau(\beta S_0 - \gamma(0))}\left(\frac{4\tau R_2(\cos\omega^* - \frac{\pi}{2}\sin\omega^*)}{1+\frac{\pi^2}{4}}e^{-2iw^*} - 2\tau R_2 e^{-3i\omega^*}\right). \tag{4.40}$$

$$\begin{aligned}
\int_{-1}^{0} e^{-2i\omega^*(\theta+1)}\cos(\omega^*(\theta-1))d\theta &= \int_{-1}^{0} e^{-2i\omega^*(\theta+1)}\frac{e^{i\omega^*(\theta-1)}+e^{-i\omega^*(\theta-1)}}{2}d\theta, \\
&= \frac{1}{2}\int_{-1}^{0}(e^{-i\omega^*(\theta-3)}+e^{-i\omega^*(3\theta+1)})d\theta, \\
&= -\left[\frac{e^{-i\omega^*(\theta-3)}}{2i\omega^*}+\frac{e^{-i\omega^*(3\theta+1)}}{6i\omega^*}\right]_{\theta=-1}^{0}, \\
&= -\frac{1}{2}\left[\frac{e^{3i\omega^*}(1-e^{i\omega^*})}{i\omega^*}+\frac{e^{-i\omega^*}(1-e^{3i\omega^*})}{3i\omega^*}\right], \\
&= \frac{3e^{4i\omega^*}-3e^{3i\omega^*}+e^{2i\omega^*}-e^{-i\omega^*}}{6i\omega^*}.
\end{aligned} \tag{4.41}$$

Analogously,

$$\begin{aligned}
\int_{-1}^{0} e^{-2i\omega^*(\theta+1)}\sin(\omega^*(\theta-1))d\theta &= \int_{-1}^{0} e^{-2i\omega^*(\theta+1)}\frac{e^{i\omega^*(\theta-1)}-e^{-i\omega^*(\theta-1)}}{2i}d\theta \\
&= \frac{1}{2i}\int_{-1}^{0}(e^{-i\omega^*(\theta-3)}-e^{-i\omega^*(3\theta+1)})d\theta, \\
&= \frac{1}{2i}\left[-\frac{e^{-i\omega^*(\theta-3)}}{i\omega^*}+\frac{e^{-i\omega^*(3\theta+1)}}{3i\omega^*}\right]_{\theta=-1}^{0} \\
&= \frac{1}{2i}\left[-\frac{e^{3i\omega^*}(1-e^{i\omega^*})}{i\omega^*}+\frac{e^{-i\omega^*}(1-e^{3i\omega^*})}{3i\omega^*}\right], \\
&= \frac{3e^{3i\omega^*}-3e^{4i\omega^*}+e^{2i\omega^*}-e^{-i\omega^*}}{6\omega^*}.
\end{aligned} \tag{4.42}$$

Now using equations (4.41) and (4.42), we get the simplified 2nd term of equation (4.39)

$$e^{-2iw^*}\int_{-1}^{0} e^{-2i\omega^*\theta}H_{20}(\theta)d\theta = \frac{4\tau R_2}{(1+\frac{\pi^2}{4})}\left[\frac{3e^{4i\omega^*}-3e^{3i\omega^*}+e^{2i\omega^*}-e^{-i\omega^*}}{6i\omega^*}\right.$$

$$
\begin{aligned}
&+ \quad \frac{\pi}{2}\left(\frac{3e^{3i\omega^*} - 3e^{4i\omega^*} + e^{2i\omega^*} - e^{-i\omega^*}}{6\omega^*}\right)\Bigg] \\
&= \quad \frac{2\tau R_2}{(1+\frac{\pi^2}{4})3\omega^*}\Bigg[- i(3e^{4i\omega^*} - 3e^{3i\omega^*} + e^{2i\omega^*} - e^{-i\omega^*}) \\
&+ \quad \frac{\pi}{2}\left(3e^{3i\omega^*} - 3e^{4i\omega^*} + e^{2i\omega^*} - e^{-i\omega^*}\right)\Bigg] \\
&= \quad \frac{2\tau R_2}{(1+\frac{\pi^2}{4})3\omega^*}\Bigg[(i+\frac{\pi}{2})(3e^{3i\omega^*} - 3e^{4i\omega^*}) \\
&+ \quad (i-\frac{\pi}{2})(e^{-i\omega^*} + e^{2i\omega^*})\Bigg]. \qquad (4.43)
\end{aligned}
$$

From equations (4.40) and (4.43), we obtain that

$$
\begin{aligned}
W_{20}(-1) &= \frac{1}{2iw^* - \tau(\beta S_0 - \gamma(0))}\left(\frac{4\tau R_2(\cos\omega^* - \frac{\pi}{2}\sin\omega^*)}{1+\frac{\pi^2}{4}}e^{-2iw^*} - 2\tau R_2 e^{-3i\omega^*}\right) \\
&+ \frac{4\tau R_2}{(1+\frac{\pi^2}{4})}\left[\frac{3e^{4i\omega^*} - 3e^{3i\omega^*} + e^{2i\omega^*} - e^{-i\omega^*}}{6i\omega^*} + \frac{\pi}{2}\left(\frac{3e^{3i\omega^*} - 3e^{4i\omega^*} + e^{2i\omega^*} - e^{-i\omega^*}}{6\omega^*}\right)\right] \\
&= \frac{2\tau R_2}{(1+\frac{\pi^2}{4})3\omega^*}\left[- i(3e^{4i\omega^*} - 3e^{3i\omega^*} + e^{2i\omega^*} - e^{-i\omega^*}) + \frac{\pi}{2}\left(3e^{3i\omega^*} - 3e^{4i\omega^*} + e^{2i\omega^*} - e^{-i\omega^*}\right)\right] \\
&= \frac{2\tau R_2}{(1+\frac{\pi^2}{4})3\omega^*}\left[(i+\frac{\pi}{2})(3e^{3i\omega^*} - 3e^{4i\omega^*}) + (i-\frac{\pi}{2})(e^{-i\omega^*} + e^{2i\omega^*})\right]. \qquad (4.44)
\end{aligned}
$$

Using the value of $H_{11}(0)$ from (4.27) in the second equation of (4.37), we get

$$
W_{11}(0) = \frac{\tau R_2\cos(\omega^*)\left(\frac{4}{1+\frac{\pi^2}{4}} - 2\right)}{\beta S_0 - \gamma(0)}. \qquad (4.45)
$$

After replacing $W_{11}(0)$ from equation (4.45) and $H_{11}(\theta)$ from (4.36) in the first equation of (4.37) and integrating, we get

$$
W_{11}(-1) = \frac{\tau R_2\cos(\omega^*)\left(\frac{4}{1+\frac{\pi^2}{4}} - 2\right)}{\beta S_0 - \gamma(0)} - \frac{2\tau R_2\cos(\omega^*)}{1+\frac{\pi^2}{4}}\left[\frac{\sin(\omega^*)}{\omega^*} + \frac{\pi}{2\omega^*}(1-\cos(\omega^*))\right] \qquad (4.46)
$$

We have,

$$\frac{g_{21}}{2} = \frac{1}{2}\left[-R_2\tau((w_{11}(-1) + e^{-i\omega^*}w_{11}(0)) + (w_{20}(-1) + e^{i\omega^*}w_{20}(0))) - R_3\tau(e^{-2i\omega^*} + 2)\right]q. \tag{4.47}$$

Next, we replace the values of $W_{20}(0)$, $W_{20}(-1)$, $W_{11}(0)$ and $W_{11}(-1)$ in equation (4.47) and simplify term by term. First term of $\frac{g_{21}}{2}$ gives

$$-R_2\tau w_{11}(-1)q \;\; = \;\; -R_2\tau(w_{11}(-1)\frac{1 - i\frac{\pi}{2}}{1 + \frac{\pi^2}{4}}. \tag{4.48}$$

In the second term of $\frac{g_{21}}{2}$, since $W_{11(0)}$ is real so it gives

$$\begin{aligned} -R_2\tau e^{-i\omega^*}w_{11}(0)q \;\; &= \;\; -R_2\tau w_{11}(0)\frac{1}{1 + \frac{\pi^2}{4}}\left[\cos(\omega^*) + \frac{\pi}{2}\sin(\omega^*)\right. \\ &- \;\; \left. i\left(\sin(\omega^*) + \frac{\pi}{2}\cos(\omega^*)\right)\right]. \end{aligned} \tag{4.49}$$

Since we need the real part of g_{21} to find the direction and $e^{i\omega^*}w_{20}(0)q$ is a very long expression, so we only consider the real part of this term.

$$\begin{aligned} Re\left[e^{i\omega^*}w_{20}(0)q\right] \;\; &= \;\; \frac{1}{1 + \frac{\pi^2}{4}}\left[Dcos\omega^*E - 2\omega^*sin\omega^*E - \frac{2\tau R_2 D}{4(\omega^*)^2 + D^2}\right] \\ &+ \;\; \frac{\pi/2}{1 + \frac{\pi^2}{4}}\left[Dsin\omega^*E + 2\omega^*cos\omega^*E - \frac{4\tau R_2\omega^*}{4(\omega^*)^2 + D^2}\right], \end{aligned} \tag{4.50}$$

where,

$$D = \tau(\beta S_0 - \gamma(0)),$$

and

$$E = \frac{4\tau R_2(\cos\omega^* - \frac{\pi}{2}\sin\omega^*)}{(1 + \frac{\pi^2}{4})(4(\omega^*)^2 + D^2)}.$$

Similarly,

$$Re\Big[w_{20}(-1)q\Big] = Re\Big[e^{-2iw^*}W_{20}(0)q\Big] + Re\Big[\Big(e^{-2i\omega^*}\int_{-1}^{0} e^{-2i\omega^*\theta}H_{20}\Big)q\Big]. \quad (4.51)$$

$$\begin{aligned} Re\Big[e^{-2iw^*}W_{20}(0)q\Big] &= \frac{1}{1+\frac{\pi^2}{4}}\Bigg[\frac{D}{D^2+4(w^*)^2}\Bigg(\frac{4\tau R_2}{1+\frac{\pi^2}{4}}((\cos\omega^* - \frac{\pi}{2}\sin\omega^*)\cos(2\omega^*)) \\ &- 2\tau R_2\cos(3\omega^*)\Bigg) \\ &+ \frac{2\omega^*}{D^2+4(w^*)^2}\Bigg(\frac{4\tau R_2}{1+\frac{\pi^2}{4}}((\cos\omega^* - \frac{\pi}{2}\sin\omega^*)\sin(2\omega^*)) - 2\tau R_2\sin(3\omega^*)\Bigg)\Bigg] \\ &+ \frac{\pi/2}{1+\frac{\pi^2}{4}}\Bigg[\frac{D}{D^2+4(w^*)^2}\Bigg(-\frac{4\tau R_2}{1+\frac{\pi^2}{4}}(\cos\omega^* - \frac{\pi}{2}\sin\omega^*)\sin(2\omega^*) + 2\tau R_2\sin(3\omega^*)\Bigg) \\ &+ \frac{2w^*}{D^2+4(w^*)^2}\Bigg(\frac{4\tau R_2}{1+\frac{\pi^2}{4}}(\cos\omega^* - \frac{\pi}{2}\sin\omega^*)\cos(2\omega^*) - 2\tau R_2\cos(3\omega^*)\Bigg)\Bigg]. \quad (4.52) \end{aligned}$$

Further, we get

$$\begin{aligned} Re\Bigg[\Big(e^{-2i\omega^*}\int_{-1}^{0} e^{-2i\omega^*\theta}H_{20}(\theta)d\theta\Big)q\Bigg] &= \frac{2\tau R_2}{(1+\frac{\pi^2}{4})^2\omega^*}\Bigg[\pi\Bigg(\cos(3\omega^*) - \cos(4\omega^*) - (1-\frac{\pi^2}{4})(\sin(3\omega^*) \\ &- \sin(4\omega^*))\Bigg)\Bigg] - \frac{2\tau R_2\pi}{(1+\frac{\pi^2}{4})\omega^*}(\sin\omega^* - \sin(2\omega^*)). \quad (4.53) \end{aligned}$$

The real part of the last term of equation (4.47) is

$$Re\Big[R_3\tau(e^{-2i\omega^*}+2)q\Big] = R_3\tau\frac{\cos(2\omega^*) + \frac{\pi}{2}\sin(2\omega^*) + 2}{1+\frac{\pi^2}{4}}. \quad (4.54)$$

To find the direction of Hopf bifurcation, we need to find the sign of μ_2, where

$$\mu_2 = -\frac{Re(C)}{\alpha'(0)},$$

with

$$C = \frac{i}{2w^*}(g_{20}g_{11} - 2|g_{11}|^2 - \frac{1}{3}|g_{02}|^2) + \frac{g_{21}}{2}. \tag{4.55}$$

Next, we get

$$\begin{aligned}(g_{20}g_{11}) &= \frac{4\tau^2 R_2^2}{\left(1+\frac{\pi^2}{4}\right)^2}\left[(1-\frac{\pi^2}{4})\cos^2(\omega^*) + \pi\cos(\omega^*)\sin(\omega^*)\right] \\ &+ i\frac{4\tau^2 R_2^2}{\left(1+\frac{\pi^2}{4}\right)^2}\left[\left(-\pi\cos^2(\omega^*) - \left(1-\frac{\pi^2}{4}\right)\cos(\omega^*)\sin(\omega^*)\right)\right].\end{aligned} \tag{4.56}$$

Based on the above analysis, all g_{ij} have been obtained. Consequently, we can compute the following terms

$$|g_{11}|^2 = 4\tau^2 R_2^2\cos^2(\omega^*)\frac{1}{1+\frac{\pi^2}{4}}, \tag{4.57}$$

and

$$|g_{02}|^2 = \frac{4\tau^2 R_2^2}{1+\frac{\pi^2}{4}}. \tag{4.58}$$

Since R_2 is real, the real part of equations (4.58) and (4.57) are zero in C. Hence,

$$Re(C) = \frac{1}{2\omega^*}\frac{4\tau^2 R_2^2}{\left(1+\frac{\pi^2}{4}\right)^2}\left[\pi\cos^2(\omega^*) + \left(1-\frac{\pi^2}{4}\right)\cos(\omega^*)\sin(\omega^*)\right] + Re(\frac{g_{21}}{2}) \tag{4.59}$$

The general result for the direction and stability of Hopf bifurcation [148], implies that the sign of μ_2 determines the direction of the Hopf bifurcation, and the sign of $\beta_2 = 2\mathrm{Re}(C(\tau^*))$ determines the stability of the bifurcating periodic solutions. Since $\alpha'(\tau^*) > 0$, we thus have the following result:

Theorem 2.1.

Let C be given in equation (4.55), then the bifurcating periodic solutions are stable if $Re(C(\tau^*)) < 0$ and unstable if $Re(C(\tau^*)) > 0$.

These are called supercritical Hopf bifurcation and subcritical Hopf bifurcation, respectively.

4.5 Numerical Simulations

In this section, we confirm these analytical results by numerical simulations of the model with systematically varied τ. To see the Hopf bifuraction around the equilibrium point $I^* = I_1^*$, we take the parameter values of the system considering the SARS-CoV-2 epidemic. We consider $\gamma_o = \frac{1}{2}$, $\gamma_1 = \frac{1}{7}$ and maximum testing $I_c = 6000$ per day [149]. Using these parameter values, we get $\omega^* = 0.2909$ and $\tau^* = 5.40$. So, we get the $Re(C(\tau^*)) = -4.6623$. Therefore, by Theorem 3.1, we conclude that the Hopf bifurcation is supercritical and the bifurcating periodic solution is asymptotically stable.

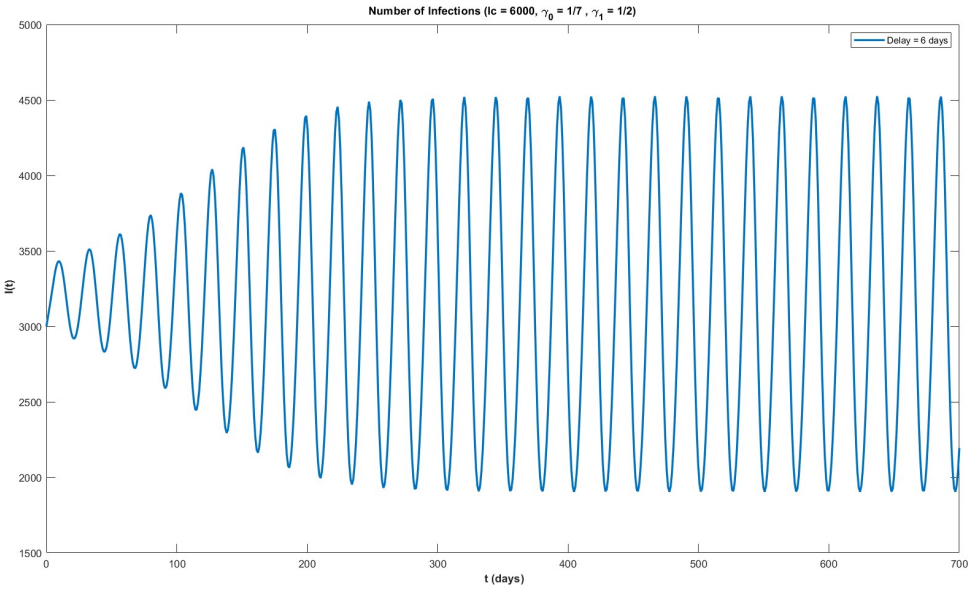

Figure 4.1: When $\tau = 6 > \tau^* = 5.40$, the bifurcating periodic solution occurs.

We observed that for small delays, the system may converge to a stable equilibrium. However, as the delay τ increases beyond a critical value, the system undergoes a Hopf bifurcation, transitioning from a stable steady state to sustained periodic oscillations.

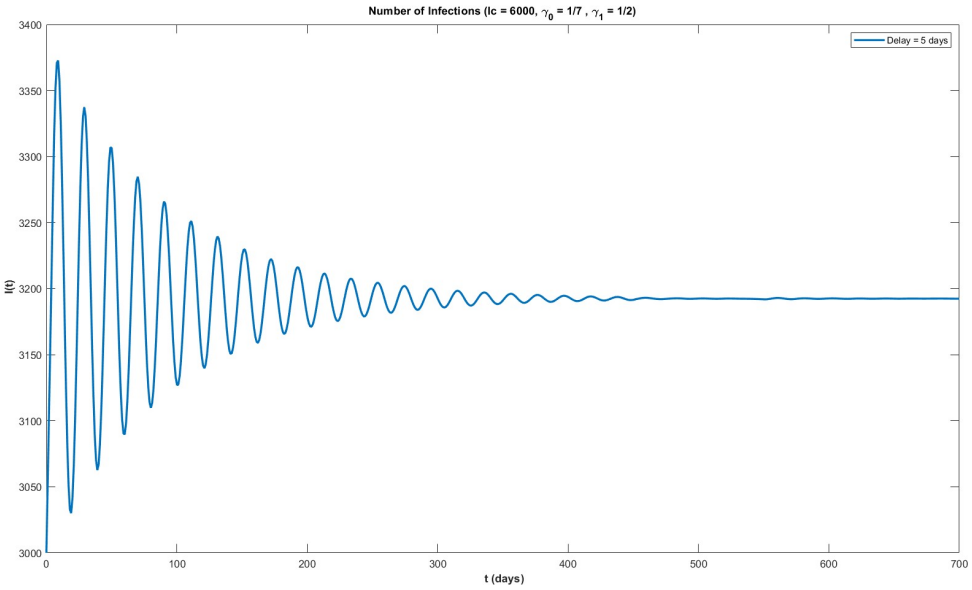

Figure 4.2: When $\tau = 5 < \tau^* = 5.40$, absence of bifurcating periodic solution.

4.6 Discussion

The primary objective of this study was to conduct a detailed Hopf bifurcation analysis of an epidemic model incorporating a time delay in the removal rate, focusing on the dynamics of infectious diseases under resource constraints. The proposed SIR-type model features a nonlinear removal rate dependent on the number of infected individuals and includes a time delay to account for the lag between infection, diagnosis, and isolation. This delay is crucial for capturing real-world complexities, particularly when healthcare resources are overwhelmed. The model exhibits a supercritical Hopf bifurcation when the time delay τ crosses a critical value τ^*, leading to stable periodic oscillations in the number of infected individuals. For small delays, the system stabilizes at a steady state, but as the delay increases beyond τ^*, the system loses stability, resulting in oscillatory dynamics. Numerical simulations, using parameters inspired by the SARS-CoV-2 epidemic, confirmed the theoretical findings, showing periodic solutions for $\tau > \tau^*$ and stable equilibrium for $\tau < \tau^*$. The findings highlight the

critical role of time delays and resource constraints in shaping the dynamics of infectious diseases.

While in our model formulation and analysis, we assume the removal rate is constant. However, in practice, the effort to remove infected individuals day by day differs between weekends and weekdays. To account for this effect, we multiply this γ with Q(t), that is

$$\tilde{\gamma} = \gamma(I(t-\tau)Q(t).$$

Assuming,

Weekdays (Mon–Fri, 5 days): High effort $\rightarrow Q = Q_h$,

Weekends (Sat–Sun, 2 days): Low effort $\rightarrow Q = Q_l$.

$$Q(t) = \begin{cases} Q_h, & if(t \bmod 7) < 5 \\ Q_l, & if(t \bmod 7) \geq 5 \end{cases}$$

Here, $Q_l < Q_h$ are constants. Since $Q(t)$ is periodic (repeats every 7 days), its average value over one week can be written as

$$\bar{Q} = \frac{\text{Total effort over 7 days}}{7} = \frac{5Q_h + 2Q_l}{7}.$$

If we assume that the average effort over a week is 1 as a baseline, then by assuming $Q_l = 0.5$, we get $Q_h = 1.2$. The theoretical study is very challenging for this; we have performed some preliminary numerical analysis for this modified removal rate, see figure 4.3. In these simulations, we still see recurrent solutions, but between the two peaks there are multiple small peaks.

The model demonstrates that delays in diagnosis and isolation, coupled with resource limitations, can lead to oscillatory behavior, resulting in recurrent waves of infection. These insights are crucial for public health decision-making, as they emphasize the importance of

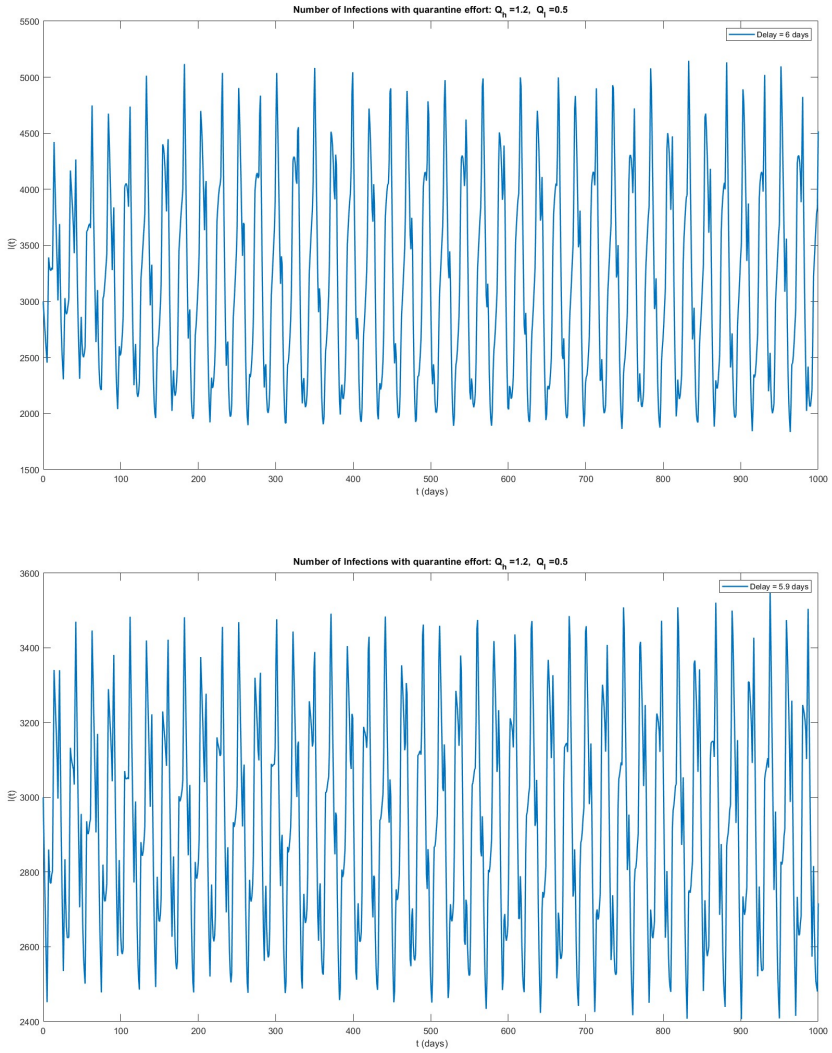

Figure 4.3: Plots with quarantine effort with delay: $\tau = 6$ and $\tau = 5.9$.

timely interventions and adequate resource allocation during outbreaks. By understanding the complex interplay between delays, resource constraints, and nonlinear removal rates, policymakers can design more effective strategies to control the spread of infectious diseases and mitigate the impact of epidemics. The study underscores the importance of timely interventions and adequate resource allocation to prevent destabilization and oscillatory behavior.

Chapter 5

Conclusion and Future Work

Mathematical models play an essential role in understanding the transmission dynamics of infectious diseases, predicting outbreak trajectories, and informing public health responses. Their significance became particularly evident during the COVID-19 pandemic, where they guided policymakers in designing effective prevention strategies. These models help analyze disease spread, assess intervention measures, optimize resource allocation, and refine control strategies, making them invaluable tools for managing epidemics. In this thesis, we developed deterministic compartmental models to address key necessities that emerged during the COVID-19 pandemic and may remain relevant in the post-pandemic era, particularly in the context of emerging variants, co-circulating respiratory infections, and evolving public health policies. This thesis addresses the gaps by developing novel mathematical models that integrate strain-specific interventions, co-circulation dynamics with shared resources, and time-dependent removal rates with delays.

The first study was conducted during the early phase of the COVID-19 pandemic, when the emergence and rapid spread of Variants of Concern (VOC) posed significant challenges to pandemic control, particularly in the absence of vaccines and widespread immunity. To examine the impact of non-pharmaceutical interventions on VOC-driven outbreaks, we developed a mathematical model that incorporates COVID-19 testing (PCR and WGS)

capacity, contact tracing, and quarantine measures. The model explores the competition between an original resident strain and a more transmissible mutant strain, highlighting the critical role of strain-specific interventions in controlling outbreaks. Our findings reveal that inadequate contact tracing and quarantine efforts can unintentionally accelerate the spread of VOCs, increasing case numbers at the outbreak peak. However, rapid testing, WGS-based identification, and strict quarantine protocols can effectively slow variant transmission, prevent outbreaks, or reduce their impact when complete control is not possible. While this study provides valuable insights into the co-dynamics of two competing strains in the short term, it has some limitations due to modeling assumptions. The model assumes a closed population, which means that births, deaths (other than disease-induced), or migration are not considered. In reality, populations undergo continuous changes that can affect disease transmission dynamics. Although this assumption simplifies the mathematical framework and focuses on short-term outbreaks, it limits the model's applicability to long-term epidemiological studies. Additionally, waning immunity and reinfection with different strains after recovery should be considered in the long-term dynamics. While this study assumes no reinfection, future work should include waning immunity and reinfection processes, which are essential for understanding the persistence of endemic pathogens and the changing interactions between co-circulating strains. These extensions would improve our grasp of public health strategies in the context of ongoing healthcare challenges and viral evolution.

The second study was conducted during the later stages of the COVID-19 pandemic, when non-pharmaceutical interventions were gradually lifted, and COVID-19 vaccination programs were being implemented worldwide. This study examines the impact of co-circulating respiratory viruses with overlapping symptoms, particularly in the presence of vaccination strategies in public health. Using a deterministic compartmental model, we explore how simultaneous outbreaks of COVID-19 and influenza strain healthcare systems and evaluate the role of vaccination in mitigating severe disease outcomes. By analyzing the deterministic

compartmental model, the findings of this research contribute to a deeper understanding of respiratory disease interactions and highlight the following key conclusions. Simultaneous outbreaks of COVID-19 and influenza can place an immense burden on healthcare systems, especially during seasonal influenza waves. The model suggests that moderate vaccination coverage of influenza, including booster doses of COVID-19 and mask-wearing, is essential to mitigate the outcomes of severe diseases. However, the model's assumptions, such as a closed population, homogeneous susceptibility, and no reinfections, limit its applicability to long-term epidemiological scenarios. Incorporating demographic changes could improve the accuracy of future models, especially for predicting disease persistence over multiple seasons. In fact, age affects the susceptibility to COVID-19 and influenza and the probability of developing symptoms [150, 151, 152]. Due to differences in contact patterns, different transmission rates are assumed among different age groups [153, 154]. In the future, the model should be adapted to accommodate different age groups. Also, the model operates under the assumption that an individual infected with one disease cannot simultaneously contract the other. While co-infection with both COVID-19 and influenza is possible, studies indicate that such occurrences are relatively rare [155, 156]. This assumption is therefore unlikely to substantially affect the overall findings. Moreover, the model assumes that once an individual recovers from an infection, they cannot be re-infected with the same disease. Research has shown that immunity to both illnesses wanes over time, making reinfection possible. In the case of influenza, reinfections are uncommon in a single season, and the interval between consecutive infections is typically long, making this assumption reasonable for the time frame of the simulations in our model [157, 154]. However, COVID-19 reinfections can occur within shorter time frames, necessitating the incorporation of waning immunity in future models [158], which may have implications for long-term disease dynamics. Furthermore, the continued emergence of variants of concern (VOCs) with altered transmissibility, severity, and potential for immune escape can further complicate epidemic control efforts by driving significant

reinfection rates, as studied in [159]. Recent modeling work [160], using a discrete SIR model and extended ODE/PDE systems [161], has begun to incorporate reinfection mechanisms to better reflect real-world patterns of diminishing immunity and immune escape. Future work should include reinfection dynamics, possibly incorporating time-varying immunity loss. This addition would enhance the predictive capacity of models in assessing long-term epidemic control, vaccine efficacy, and the potential for recurrent outbreaks.

Incorporating population dynamics, age-structured transmission, and waning immunity into future models could enhance their accuracy in predicting the co-circulation of multiple diseases over time. All co-circulation scenarios in this study introduce both pathogens simultaneously. Given that influenza is a seasonal virus while COVID-19 may persist year-round, future research should explore the impact of different introduction times on disease dynamics. Additionally, the model can be expanded to include other co-circulating respiratory diseases, such as respiratory syncytial virus (RSV), which presents similar clinical symptoms.

In the third study, model incorporates time dependent removal rates with delay, capturing the impact of delays in testing and isolation. While this study provides valuable insights into the dynamics of epidemics with delayed removal rates, future work could extend the model to include additional long-term factors such as vaccination. The model currently incorporates a single delay in the removal rate, future research could investigate the impact of multiple delays, such as delays in vaccination rollout or delays in public awareness and behavioral changes. A model with time dependent incidence rate under behaviour change with delay is studied in [145]. The model could be applied to specific infectious diseases, such as influenza, RSV, etc, to study how delays and resource constraints influence the spread of these diseases in different settings.

The findings of this thesis contribute to the understanding of respiratory infectious diseases in both pandemic and epidemic settings. Although our work primarily focuses on SARS-CoV-2 and influenza, the models we developed here are widely applicable to a broader

range of public health challenges, particularly in scenarios when multiple virus pathogens or variants spread at the same time and have similar clinical symptoms. These shared symptoms, combined with limited diagnostic and healthcare resources, can lead to delayed testing, limited capacity, and slower public health responses - all of which contribute to case backlogs and intensified transmission. The models and theoretical insights developed here are well-suited to address these complexities and can be adapted to future outbreaks involving pathogens such as RSV or novel respiratory viruses. While our models capture the impact of such systemic pressures on disease spread and intervention effectiveness, they do not explicitly quantify epidemiological indicators such as the attack ratio (or attack rate), which measures the proportion of a population that becomes infected over the course of an outbreak. This indicator is of particular importance to public health officials, as it helps assess the overall severity and spread of infection, estimate population-level immunity, and guide decisions on resource allocation and vaccination strategies. Future extensions of this work should integrate the attack rate as a key variable to improve the models' applicability for real-time public health planning and situational responsiveness. Overall, the analyses conducted through these models provide valuable guidance for public health officials to strategically optimize resource allocation and strengthen preparedness. As a result, healthcare systems can be better positioned to respond effectively to concurrent respiratory outbreaks.

Bibliography

[1] A Danielle Iuliano et al. “Estimates of global seasonal influenza-associated respiratory mortality: a modelling study”. In: *The Lancet* 391.10127 (2018), pp. 1285–1300.

[2] Niamh M Troy and Anthony Bosco. “Respiratory viral infections and host responses; insights from genomics”. In: *Respiratory research* 17 (2016), pp. 1–12.

[3] Haidong Wang et al. “Estimating excess mortality due to the COVID-19 pandemic: a systematic analysis of COVID-19-related mortality, 2020–21”. In: *The Lancet* 399.10334 (2022), pp. 1513–1536.

[4] Rachael Milwid et al. “Toward standardizing a lexicon of infectious disease modeling terms”. In: *Frontiers in public health* 4 (2016), p. 213.

[5] William Ogilvy Kermack and Anderson G McKendrick. “A contribution to the mathematical theory of epidemics”. In: *Proceedings of the royal society of london. Series A, Containing papers of a mathematical and physical character* 115.772 (1927), pp. 700–721.

[6] William O Kermack and Anderson G McKendrick. “Contributions to the mathematical theory of epidemics–I. 1927.” In: *Bulletin of mathematical biology* 53.1-2 (1991), pp. 33–55.

[7] Seyed M Moghadas. “Gaining insights into human viral diseases through mathematics”. In: *European journal of epidemiology* 21 (2006), pp. 337–342.

[8] James D Murray. *Mathematical biology: I. An introduction*. Vol. 17. Springer Science & Business Media, 2007.

[9] Matt J Keeling and Pejman Rohani. *Modeling infectious diseases in humans and animals*. Princeton university press, 2008.

[10] Fred Brauer. "Compartmental models in epidemiology". In: *Mathematical epidemiology* (2008), pp. 19–79.

[11] RM Anderson. *Infectious diseases of humans: dynamics and control*. Oxford University Press, 1991.

[12] SV Chepur et al. "Respiratory RNA viruses: how to be prepared for an encounter with new pandemic virus strains". In: *Biology Bulletin Reviews* 11.2 (2021), pp. 154–171.

[13] Christopher W Potter. "A history of influenza". In: *Journal of applied microbiology* 91.4 (2001), pp. 572–579.

[14] *Genomic Surveillance for SARS-CoV-2 Variants*. URL: `https://www.cdc.gov/coronavirus/2019-ncov/cases-updates/variant-surveillance.html`.

[15] Maggi Banning. "Influenza: incidence, symptoms and treatment". In: *British journal of nursing* 14.22 (2005), pp. 1192–1197.

[16] Naomi R Waterlow. "Mathematical Modelling of Cross-protection Between Respiratory Viruses." PhD thesis. London School of Hygiene & Tropical Medicine, 2022.

[17] Walter N Harrington, Christina M Kackos, and Richard J Webby. "The evolution and future of influenza pandemic preparedness". In: *Experimental & molecular medicine* 53.5 (2021), pp. 737–749.

[18] Edwin D Kilbourne. "Influenza pandemics of the 20th century". In: *Emerging infectious diseases* 12.1 (2006), p. 9.

[19] Natasha Khan. *New virus discovered by Chinese scientists investigating pneumonia outbreak. Hong Kong: The Wall Street Journal*. 2020.

[20] Na Zhu et al. “A novel coronavirus from patients with pneumonia in China, 2019”. In: *New England journal of medicine* 382.8 (2020), pp. 727–733.

[21] Nanshan Chen et al. “Epidemiological and clinical characteristics of 99 cases of 2019 novel coronavirus pneumonia in Wuhan, China: a descriptive study”. In: *The lancet* 395.10223 (2020), pp. 507–513.

[22] Haidong Wang et al. “Estimating excess mortality due to the COVID-19 pandemic: a systematic analysis of COVID-19-related mortality, 2020–21”. In: *The Lancet* 399.10334 (2022), pp. 1513–1536.

[23] Pratha Sah et al. “Asymptomatic SARS-CoV-2 infection: A systematic review and meta-analysis”. In: *Proceedings of the National Academy of Sciences* 118.34 (2021), e2109229118.

[24] Hien Lau et al. “Evaluating the massive underreporting and undertesting of COVID-19 cases in multiple global epicenters”. In: *Pulmonology* 27.2 (2021), pp. 110–115.

[25] Finlay Campbell et al. “Increased transmissibility and global spread of SARS-CoV-2 variants of concern as at June 2021”. In: *Eurosurveillance* 26.24 (2021), p. 2100509.

[26] *Updates on COVID-19 Variants of concern*. URL: `https://nccid.ca/covid-19-variants/`.

[27] Ingrid Torjesen. *Covid-19: Delta variant is now UK’s most dominant strain and spreading through schools*. 2021.

[28] Adam S Lauring and Emma B Hodcroft. “Genetic variants of SARS-CoV-2—what do they mean?” In: *Jama* 325.6 (2021), pp. 529–531.

[29] Lin Yao et al. “Omicron subvariants escape antibodies elicited by vaccination and BA. 2.2 infection”. In: *The Lancet Infectious Diseases* 22.8 (2022), pp. 1116–1117.

[30] World Health Organization. *Statement on the fifteenth meeting of the International Health Regulations (2005) emergency committee regarding the coronavirus disease (COVID-19) pandemic*. Accessed: 6 May 2023. 2023. URL: https://www.who.int/news/item/05-05-2023-statement-on-the-fifteenth-meeting-of-the-international-health-regulations-(2005)-emergency-committee-regarding-the-coronavirus-disease-(covid-19)-pandemic?adgroupsurvey=7Badgroupsurvey7D&gclid=EAIaIQobChMI4Ojtsdbe_gIVjQRyCh07igt4EAAYASACEgJ9pfD_BwE&fbclid=IwAR2M8EAyiSrAodhK9p-X582nHkP2AigpSX8pYIsLsPwqYh4SG26RGokGe7E.

[31] Carmen Sofia Arriola et al. "Influenza vaccine effectiveness against hospitalizations in children and older adults—data from South America, 2013–2017. A test negative design". In: *Vaccine: X* 3 (2019), p. 100047.

[32] Gilberto Gonzalez-Parra, David Martínez-Rodríguez, and Rafael J Villanueva-Micó. "Impact of a new SARS-CoV-2 variant on the population: A mathematical modeling approach". In: *Mathematical and Computational Applications* 26.2 (2021), p. 25.

[33] SY Tchoumi, H Rwezaura, and JM Tchuenche. "Dynamic of a two-strain COVID-19 model with vaccination". In: *Results in physics* 39 (2022), p. 105777.

[34] Osman Yagan et al. "Modeling and analysis of the spread of COVID-19 under a multiple-strain model with mutations". In: *Harv. Data Sci. Rev* 4 (2021), pp. 1–38.

[35] Adriana-Stefania Ciupeanu et al. "Mathematical modeling of the dynamics of COVID-19 variants of concern: asymptotic and finite-time perspectives". In: *Infectious Disease Modelling* 7.4 (2022), pp. 581–596.

[36] Kaiming Bi et al. "Annual Hospitalizations for COVID-19, Influenza, and Respiratory Syncytial Virus, United States, 2023–2024". In: *Emerging Infectious Diseases* 31.3 (2025), p. 636.

[37] Yonghong Liu et al. “Measuring Interactions between SARS-CoV-2, Influenza, and Respiratory Syncytial Virus In Co-Epidemics: A Modelling Study”. In: ().

[38] M Nuno et al. “Mathematical models of influenza: the role of cross-immunity, quarantine and age-structure”. In: *Mathematical epidemiology*. Springer, 2008, pp. 349–364.

[39] Saminu Bala and Bello Gimba. “Global sensitivity analysis to study the impacts of bed-nets, drug treatment, and their efficacies on a two-strain malaria model”. In: *Mathematical and Computational Applications* 24.1 (2019), p. 32.

[40] Peter Rashkov and Bob W Kooi. “Complexity of host-vector dynamics in a two-strain dengue model”. In: *Journal of Biological Dynamics* 15.1 (2021), pp. 35–72.

[41] Taqi AM Shatnawi et al. “A two-strain COVID-19 co-infection model with strain 1 vaccination”. In: *Partial Differential Equations in Applied Mathematics* 12 (2024), p. 100945.

[42] Bruce Pell et al. “The emergence of a virus variant: dynamics of a competition model with cross-immunity time-delay validated by wastewater surveillance data for COVID-19”. In: *Journal of mathematical biology* 86.5 (2023), p. 63.

[43] Hamed Jabraeilian and Yousef Jamali. “Omicron vs. the rest: Assessing the competitive dynamics and coinfection scenarios of COVID-19 strains on a social network”. In: *Plos one* 19.1 (2024), e0287623.

[44] M Ahumada et al. “Mutation and SARS-CoV-2 strain competition under vaccination in a modified SIR model”. In: *Chaos, Solitons & Fractals* 166 (2023), p. 112964.

[45] Edilson F Arruda et al. “Modelling and optimal control of multi strain epidemics, with application to COVID-19”. In: *Plos one* 16.9 (2021), e0257512.

[46] Li Wen et al. “Modeling the co-circulation of influenza and COVID-19 in Hong Kong, China”. In: *Advances in Continuous and Discrete Models* 2024.1 (2024), p. 32.

[47] John T Kubale et al. “High co-circulation of influenza and SARS-CoV-2”. In: *medRxiv* (2022).

[48] John S Tam and Yuelong Shu. “Public health control measures for the co-circulation of influenza and SARS-CoV-2 during influenza seasons”. In: *China CDC Weekly* 4.2 (2022), p. 22.

[49] Nadine Barth. “A Stochastic Compartmental Model to Describe the Co-Circulation of Influenza and COVID-19 and Investigating the Potential Effects of Vaccination Strategies”. In: (2024).

[50] Qingchun Pan et al. “Co-circulation and co-infection of COVID-19 and influenza in China: challenges and implications”. In: *Frontiers in Public Health* 11 (2023), p. 1295877.

[51] Shuai-xing Wang and Da-yan Wang. “Co-Circulation, Co-infection of SARS-CoV-2 and influenza virus, where will it go?” In: *Zoonoses* 3.1 (2023), p. 980.

[52] Jingyi Liang et al. “Influenza and COVID-19 co-infection and vaccine effectiveness against severe cases: a mathematical modeling study”. In: *Frontiers in Cellular and Infection Microbiology* 14 (2024), p. 1347710.

[53] WS Avusuglo et al. “Workplace absenteeism due to COVID-19 and influenza across Canada: A mathematical model”. In: *Journal of Theoretical Biology* 572 (2023), p. 111559.

[54] Manuel A Acuña-Zegarra et al. “Co-circulation of SARS-CoV-2 and influenza under vaccination scenarios”. In: *medRxiv* (2021), pp. 2020–12.

[55] Maria Pachetti et al. “Emerging SARS-CoV-2 mutation hot spots include a novel RNA-dependent-RNA polymerase variant”. In: *Journal of translational medicine* 18 (2020), pp. 1–9.

[56] Adam J Kucharski et al. “Effectiveness of isolation, testing, contact tracing, and physical distancing on reducing transmission of SARS-CoV-2 in different settings: a mathematical modelling study”. In: *The Lancet Infectious Diseases* 20.10 (2020), pp. 1151–1160.

[57] Biao Tang et al. “The effectiveness of quarantine and isolation determine the trend of the COVID-19 epidemics in the final phase of the current outbreak in China”. In: *International Journal of Infectious Diseases* 95 (2020), pp. 288–293.

[58] Calistus N Ngonghala et al. “Mathematical assessment of the impact of non-pharmaceutical interventions on curtailing the 2019 novel Coronavirus”. In: *Mathematical biosciences* 325 (2020), p. 108364.

[59] Mirjam E Kretzschmar et al. “Impact of delays on effectiveness of contact tracing strategies for COVID-19: a modelling study”. In: *The Lancet Public Health* 5.8 (2020), e452–e459.

[60] Joel Hellewell et al. “Feasibility of controlling COVID-19 outbreaks by isolation of cases and contacts”. In: *The Lancet Global Health* 8.4 (2020), e488–e496.

[61] Luca Ferretti et al. “Quantifying SARS-CoV-2 transmission suggests epidemic control with digital contact tracing”. In: *Science* 368.6491 (2020).

[62] Tony Kirby. “New variant of SARS-CoV-2 in UK causes surge of COVID-19”. In: *The Lancet Respiratory Medicine* 9.2 (2021), e20–e21.

[63] Sergio Celaschi. “The impact of SARS-CoV-2 variant to COVID-19 epidemic in Brazil”. In: *medRxiv* (2020).

[64] Houriiyah Tegally et al. “Major new lineages of SARS-CoV-2 emerge and spread in South Africa during lockdown”. In: *medRxiv* (2020).

[65] Nicholas G Davies et al. “Estimated transmissibility and impact of SARS-CoV-2 lineage B. 1.1. 7 in England”. In: *Science* 372.6538 (2021).

[66] Erik Volz et al. “Transmission of SARS-CoV-2 Lineage B. 1.1. 7 in England: Insights from linking epidemiological and genetic data”. In: *MedRxiv* (2021), pp. 2020–12.

[67] Jianhong Wu et al. “The Impact of Public Health Interventions on Delaying and Mitigating against Replacement by SARS-CoV-2 Variants of Concern”. In: *Available at SSRN 3779007* (2021).

[68] Gilberto Gonzalez-Parra, David Martínez-Rodríguez, and Rafael J Villanueva-Micó. “Impact of a new SARS-CoV-2 variant on the population: A mathematical modeling approach”. In: *Mathematical and Computational Applications* 26.2 (2021), p. 25.

[69] Biao Tang et al. “De-escalation by reversing the escalation with a stronger synergistic package of contact tracing, quarantine, isolation and personal protection: feasibility of preventing a COVID-19 rebound in Ontario, Canada, as a case study”. In: *Biology* 9.5 (2020), p. 100.

[70] Odo Diekmann, Johan Andre Peter Heesterbeek, and Johan AJ Metz. “On the definition and the computation of the basic reproduction ratio R 0 in models for infectious diseases in heterogeneous populations”. In: *Journal of mathematical biology* 28.4 (1990), pp. 365–382.

[71] Jane M Heffernan, Robert J Smith, and Lindi M Wahl. “Perspectives on the basic reproductive ratio”. In: *Journal of the Royal Society Interface* 2.4 (2005), pp. 281–293.

[72] M Li, X Liang, Q Jiang, et al. “The latest understanding of the epidemiological characteristics of new coronavirus pneumonia”. In: *Chin J Epidemiol* 41 (2020), pp. 139–143.

[73] Biao Tang et al. “Estimation of the transmission risk of the 2019-nCoV and its implication for public health interventions”. In: *Journal of clinical medicine* 9.2 (2020), p. 462.

[74] Shabnam Iezadi et al. “Effectiveness of non-pharmaceutical public health interventions against COVID-19: A systematic review and meta-analysis”. In: *PloS one* 16.11 (2021), e0260371.

[75] Nicola Perra. “Non-pharmaceutical interventions during the COVID-19 pandemic: A review”. In: *Physics Reports* 913 (2021), pp. 1–52.

[76] Daniel R Feikin et al. “Duration of effectiveness of vaccines against SARS-CoV-2 infection and COVID-19 disease: results of a systematic review and meta-regression”. In: *The Lancet* (2022).

[77] Megan Scudellari. “How the pandemic might play out in 2021 and beyond.” In: *Nature* (2020), pp. 22–25.

[78] Yusha Araf et al. “Omicron variant of SARS-CoV-2: genomics, transmissibility, and responses to current COVID-19 vaccines”. In: *Journal of medical virology* 94.5 (2022), pp. 1825–1832.

[79] Yuntao Zou et al. “The vaccine efficacy against the SARS-CoV-2 omicron: a systemic review and meta-analysis”. In: *Frontiers in Public Health* (2022), p. 2235.

[80] Sarah A Buchan et al. “Estimated Effectiveness of COVID-19 Vaccines Against Omicron or Delta Symptomatic Infection and Severe Outcomes”. In: *JAMA network open* 5.9 (2022), e2232760–e2232760.

[81] Senjuti Saha et al. “New waves, new variants, old inequity: a continuing COVID-19 crisis”. In: *BMJ Global Health* 6.8 (2021), e007031.

[82] Rustom Antia and M Elizabeth Halloran. “Transition to endemicity: Understanding COVID-19”. In: *Immunity* 54.10 (2021), pp. 2172–2176.

[83] You Li et al. “The role of respiratory co-infection with influenza or respiratory syncytial virus in the clinical severity of COVID-19 patients: a systematic review and meta-analysis”. In: *Authorea Preprints* (2022).

[84] Resat Ozaras et al. “Influenza and COVID-19 coinfection: report of six cases and review of the literature”. In: *Journal of medical virology* 92.11 (2020), pp. 2657–2665.

[85] Q Sue Huang et al. “Impact of the COVID-19 nonpharmaceutical interventions on influenza and other respiratory viral infections in New Zealand”. In: *Nature communications* 12.1 (2021), pp. 1–7.

[86] Vijaykrishna Dhanasekaran et al. “Human seasonal influenza under COVID-19 and the potential consequences of influenza lineage elimination”. In: *Nature communications* 13.1 (2022), pp. 1–11.

[87] Ehrlich, Haley and Boneva, Dessy and Elkbuli, Adel. “The intersection of viral illnesses: A seasonal influenza epidemic amidst the COVID-19 pandemic”. In: *Annals of Medicine and Surgery* 60 (2020), pp. 41–43.

[88] Lulla Opatowski, Marc Baguelin, and Rosalind M Eggo. “Influenza interaction with cocirculating pathogens and its impact on surveillance, pathogenesis, and epidemic profile: A key role for mathematical modelling”. In: *PLoS pathogens* 14.2 (2018), e1006770.

[89] Manuel Adrian Acuna Zegarra et al. “Co-circulation of SARS-CoV-2 and Influenza under vaccination scenarios”. In: (2021). Preprint on webpage at `https://www.medrxiv.org/content/10.1101/2020.12.29.20248953v2`. DOI: `10.1101/2020.12.29.20248953`.

[90] Alexander Domnich et al. “Effect of the 2020/21 season influenza vaccine on SARS-CoV-2 infection in a cohort of Italian healthcare workers”. In: *Vaccine* 40.12 (2022), pp. 1755–1760.

[91] Elias Tayar et al. “Effectiveness of influenza vaccination against SARS-CoV-2 infection among healthcare workers in Qatar”. In: *medRxiv* (2022).

[92] Kadhim Hayawi et al. “Vaccine versus Variants (3Vs): are the COVID-19 vaccines effective against the variants? A systematic review”. In: *Vaccines* 9.11 (2021), p. 1305.

[93] Santenna Chenchula et al. “Current evidence on efficacy of COVID-19 booster dose vaccination against the Omicron variant: A systematic review”. In: *Journal of Medical Virology* 94.7 (2022), pp. 2969–2976.

[94] Ramandip Grewal et al. “Effectiveness of a fourth dose of covid-19 mRNA vaccine against the omicron variant among long term care residents in Ontario, Canada: test negative design study”. In: *bmj* 378 (2022).

[95] Government of Canada. *Testing for COVID-19: When to get tested and testing results*. https://www.canada.ca/en/public-health/services/diseases/2019-novel-coronavirus-infection/symptoms/testing/diagnosing.html#a4, note=. 2022.

[96] Government of Canada. *Covid-19 Vaccination in Canada*. https://health-infobase.canada.ca/covid-19/vaccination-coverage/, note =. 2022.

[97] Public Health Canada. *Seasonal Influenza (Flu) Vaccination Coverage Survey Results, 2019-2020*. https://www.canada.ca/en/public-health/services/publications/vaccines-immunization/2019-2020-seasonal-influenza-flu-vaccine-coverage-survey-results.html. Acessed: August 26, 2022. 2022.

[98] Melissa K Andrew et al. “Influenza vaccine effectiveness against influenza-related hospitalization during a season with mixed outbreaks of four influenza viruses: a test-negative case-control study in adults in Canada”. In: *BMC Infectious Diseases* 17.1 (2017), pp. 1–11.

[99] Michaela K Nichols et al. “Influenza vaccine effectiveness to prevent influenza-related hospitalizations and serious outcomes in Canadian adults over the 2011/12 through 2013/14 influenza seasons: a pooled analysis from the Canadian Immunization Research

Network (CIRN) Serious Outcomes Surveillance (SOS Network)". In: *Vaccine* 36.16 (2018), pp. 2166–2175.

[100] Jummy David et al. "Non-pharmaceutical intervention levels to reduce the COVID-19 attack ratio among children". In: *Royal Society Open Science* 9.3 (2022), p. 211863.

[101] Nicholas G Davies et al. "Estimated transmissibility and impact of SARS-CoV-2 lineage B. 1.1. 7 in England". In: *Science* 372.6538 (2021), eabg3055.

[102] Erik Volz et al. "Assessing transmissibility of SARS-CoV-2 lineage B. 1.1. 7 in England". In: *Nature* 593.7858 (2021), pp. 266–269.

[103] Canadian Institute for Health Information. *COVID-19 Hospitalization and Emergency Department Statistics, 2021–2022*. `https://www.cihi.ca/en/covid-19-hospitalization-and-emergency-department-statistics`. Acessed: July 25, 2022. 2022.

[104] Zachary McCarthy et al. "Quantifying the annual incidence and underestimation of seasonal influenza: A modelling approach". In: *Theoretical Biology and Medical Modelling* 17.1 (2020), pp. 1–16.

[105] Biao Tang et al. "De-escalation by reversing the escalation with a stronger synergistic package of contact tracing, quarantine, isolation and personal protection: feasibility of preventing a COVID-19 rebound in Ontario, Canada, as a case study". In: *Biology* 9.5 (2020), p. 100.

[106] Sarah A Buchan et al. "Effectiveness of COVID-19 vaccines against Omicron or Delta infection". In: *MedRxiv* (2022), pp. 2021–12.

[107] Kyeongah Nah et al. "Impact of influenza vaccine-modified infectivity on attack rate, case fatality ratio and mortality". In: *Journal of Theoretical Biology* 492 (2020), p. 110190.

[108] Center for Disease Control and Prevention (CDC). *Vaccine Effectiveness: How Well Do Flu Vaccines Work?* https://www.cdc.gov/flu/vaccines-work/vaccineeffect.htm, note=. 2022.

[109] Govermment of Canada. *Testing for COVID-19*. https://www.canada.ca/en/public-health/services/diseases/2019-novel-coronavirus-infection/symptoms/testing/diagnosing.html. Last modified: July 30, 2022, Acessed: August 5, 2022. 2022.

[110] Public Helath Ontario. *Ontario COVID-19 Data Tool*. https://www.publichealthontario.ca/en/data-and-analysis/infectious-disease/covid-19-data-surveillance/covid-19-data-tool?tab=overview. Acessed: August 17, 2022. 2022.

[111] Public Health Ontarion. *COVID-19 Vaccine Data in Ontario-Hospitalizations by vaccination status*. https://data2.ontario.ca/en/dataset/covid-19-vaccine-data-in-ontario/resource/274b819c-5d69-4539-a4db-f2950794138c. Acessed: july 7,2022. 2022.

[112] Markos Kalligeros et al. "Influenza vaccine effectiveness against influenza-associated hospitalization in children: a systematic review and meta-analysis". In: *Vaccine* 38.14 (2020), pp. 2893–2903.

[113] Boloye Gomero. "Latin hypercube sampling and partial rank correlation coefficient analysis applied to an optimal control problem". In: (2012).

[114] Simeone Marino et al. "A methodology for performing global uncertainty and sensitivity analysis in systems biology". In: *Journal of theoretical biology* 254.1 (2008), pp. 178–196.

[115] MD McKay. "McKay, MD, Conover, WJ and RJ Beckman (1979)". In: *A comparison of three methods for selecting values of input variables in the analysis of output from a computer code. Technometrics* 21 (1979), pp. 239–245.

[116] John Paget et al. "Global mortality associated with seasonal influenza epidemics: New burden estimates and predictors from the GLaMOR Project". In: *Journal of global health* 9.2 (2019).

[117] WHO. *Influenza (seasonal).* `https://www.who.int/news-room/fact-sheets/detail/influenza-(seasonal)`. Acessed: August 15, 2022. 2022.

[118] Shui Shan Lee, Cecile Viboud, and Eskild Petersen. "Understanding the rebound of influenza in the post COVID-19 pandemic period holds important clues for epidemiology and control". In: *International Journal of Infectious Diseases* 122 (2022), pp. 1002–1004.

[119] Hao Lei et al. "Nonpharmaceutical interventions used to control COVID-19 reduced seasonal influenza transmission in China". In: *The Journal of infectious diseases* 222.11 (2020), pp. 1780–1783.

[120] Helen E Groves et al. "The impact of the COVID-19 pandemic on influenza, respiratory syncytial virus, and other seasonal respiratory virus circulation in Canada: A population-based study". In: *The Lancet Regional Health-Americas* 1 (2021), p. 100015.

[121] Andrea Nwosu et al. "Influenza Vaccine: National Influenza Annual Report, Canada, 2020–2021, in the global context". In: *Canada Communicable Disease Report* 47.10 (2021), p. 405.

[122] Sonja J Olsen et al. "Decreased influenza activity during the COVID-19 pandemic—United States, Australia, Chile, and South Africa, 2020". In: *American Journal of Transplantation* 20.12 (2020), pp. 3681–3685.

[123] Takahiro Itaya, Yuki Furuse, and Kazuaki Jindai. "Does COVID-19 infection impact on the trend of seasonal influenza infection? 11 countries and regions, from 2014 to 2020". In: *International Journal of Infectious Diseases* 97 (2020), pp. 78–80.

[124] Jeehyun Kim et al. "Changing influenza activity in the Southern hemisphere countries during the COVID-19 pandemic". In: *International Journal of Infectious Diseases* 108 (2021), pp. 109–111.

[125] Australian Department of Health and Aged Care. *Australian Influenza Surveillance Report and Activity Updates*. https://www1.health.gov.au/internet/main/publishing.nsf/Content/ozflu-surveil-no06-22.html. Acessed: July 5, 2022.

[126] Public Health Agency of Canada (PHAC). *Influenza weekly reports 2021-22 season. Ottawa: PHAC; 2022*. https://www.canada.ca/en/public-health/services/publications/diseases-conditions/fluwatch/2021-2022/weeks-16-18-april-17-may-7-2022.html. Acessed: July 5, 2022.

[127] Eskild Petersen et al. "Comparing SARS-CoV-2 with SARS-CoV and influenza pandemics". In: *The Lancet infectious diseases* 20.9 (2020), e238–e244.

[128] Xianlong Zhou et al. "Machine learning-based decision model to distinguish between COVID-19 and influenza: A retrospective, two-centered, diagnostic study". In: *Risk Management and Healthcare Policy* 14 (2021), p. 595.

[129] Suzan Farhang-Sardroodi et al. "A machine learning approach to differentiate between COVID-19 and influenza infection using synthetic infection and immune response data". In: *medRxiv* (2022).

[130] CDC. *Seasonal Flu Vaccine Effectiveness Studies*. https://www.cdc.gov/flu/vaccines-work/effectiveness-studies.htm. Acessed: August 15, 2022. 2022.

[131] Hannah E Segaloff et al. “Influenza vaccine effectiveness against hospitalization in fully and partially vaccinated children in Israel: 2015–2016, 2016–2017, and 2017–2018”. In: *Clinical Infectious Diseases* 69.12 (2019), pp. 2153–2161.

[132] Carmen Sofia Arriola et al. “Influenza vaccine effectiveness against hospitalizations in children and older adults—Data from South America, 2013–2017. A test negative design”. In: *Vaccine: X* 3 (2019), p. 100047.

[133] Matthieu Domenech de Cellès et al. “Influenza may facilitate the spread of SARS-CoV-2”. In: *medRxiv* (2020).

[134] Marco Del Riccio et al. “The association between influenza vaccination and the risk of SARS-CoV-2 infection, severe illness, and death: a systematic review of the literature”. In: *International journal of environmental research and public health* 17.21 (2020), p. 7870.

[135] Amparo Larrauri and Katarina Prosenc Trilar. “Preparing for an influenza season 2021/22 with a likely co-circulation of influenza virus and SARS-CoV-2”. In: *Eurosurveillance* 26.41 (2021), p. 2100975.

[136] Jingjing He et al. “Proportion of asymptomatic coronavirus disease 2019: A systematic review and meta-analysis”. In: *Journal of medical virology* 93.2 (2021), pp. 820–830.

[137] Kanica Goel, Abhishek Kumar, and Nilam. “Nonlinear dynamics of a time-delayed epidemic model with two explicit aware classes, saturated incidences, and treatment”. In: *Nonlinear Dynamics* 101.3 (2020), pp. 1693–1715.

[138] Balram Dubey, Preeti Dubey, and Uma S Dubey. “Dynamics of an SIR model with nonlinear incidence and treatment rate”. In: *Applications and Applied Mathematics: An International Journal (AAM)* 10.2 (2015), p. 5.

[139] Chunhua Shan and Huaiping Zhu. “Bifurcations and complex dynamics of an SIR model with the impact of the number of hospital beds”. In: *Journal of Differential Equations* 257.5 (2014), pp. 1662–1688.

[140] Seyed M Moghadas and Murray E Alexander. “Bifurcations of an epidemic model with non-linear incidence and infection-dependent removal rate”. In: *Mathematical Medicine and Biology: A Journal of the IMA* 23.3 (2006), pp. 231–254.

[141] ME Alexander and SM Moghadas. “Periodicity in an epidemic model with a generalized non-linear incidence”. In: *Mathematical Biosciences* 189.1 (2004), pp. 75–96.

[142] Yoichi Enatsu et al. “Stability analysis of delayed SIR epidemic models with a class of nonlinear incidence rates”. In: *Applied Mathematics and Computation* 218.9 (2012), pp. 5327–5336.

[143] Ram Naresh et al. “Stability analysis of a time delayed SIR epidemic model with nonlinear incidence rate”. In: *Computers & mathematics with applications* 58.2 (2009), pp. 348–359.

[144] Hongfan Lu et al. “Mathematical modeling and dynamic analysis of SIQR model with delay for pandemic COVID-19”. In: *Math. Biosci. Eng* 18.4 (2021), pp. 3197–3214.

[145] Xue Zhang et al. “Renewal equations for delayed population behaviour adaptation coupled with disease transmission dynamics: A mechanism for multiple waves of emerging infections”. In: *Mathematical Biosciences* 365 (2023), p. 109068.

[146] Julien Arino, Lin Wang, and Gail SK Wolkowicz. “An alternative formulation for a delayed logistic equation”. In: *Journal of theoretical biology* 241.1 (2006), pp. 109–119.

[147] Shigui Ruan. “Delay differential equations in single species dynamics”. In: *Delay differential equations and applications*. Springer, 2006, pp. 477–517.

[148] Brian D Hassard, Nicholas D Kazarinoff, and Yieh-Hei Wan. *Theory and applications of Hopf bifurcation*. Vol. 41. CUP Archive, 1981.

[149] Bushra Majeed, Marco Tosato, and Jianhong Wu. “Variant-specific interventions to slow down replacement and prevent outbreaks”. In: *Mathematical Biosciences* 343 (2022), p. 108703.

[150] Nicholas G Davies et al. “Age-dependent effects in the transmission and control of COVID-19 epidemics”. In: *Nature medicine* 26.8 (2020), pp. 1205–1211.

[151] Edward Goldstein, Marc Lipsitch, and Muge Cevik. “On the effect of age on the transmission of SARS-CoV-2 in households, schools, and the community”. In: *The Journal of infectious diseases* 223.3 (2021), pp. 362–369.

[152] Colin J Worby et al. “On the relative role of different age groups in influenza epidemics”. In: *Epidemics* 13 (2015), pp. 10–16.

[153] Yang Liu et al. “What are the underlying transmission patterns of COVID-19 outbreak? An age-specific social contact characterization”. In: *EClinicalMedicine* 22 (2020).

[154] Mostafa Javanian et al. “A brief review of influenza virus infection”. In: *Journal of medical virology* 93.8 (2021), pp. 4638–4646.

[155] Shabnam Dehghan Tarzjani et al. “Clinical challenge of co-infection of SARS-CoV-2 with influenza during the influenza circulation season: suggestions for prevention.” In: *Germs* 13.2 (2023).

[156] Masoud Dadashi et al. “COVID-19 and influenza co-infection: a systematic review and meta-analysis”. In: *Frontiers in medicine* 8 (2021), p. 681469.

[157] Jing Wang et al. “Epidemiology of influenza virus reinfection in Guangxi, China: a retrospective analysis of a nine-year influenza surveillance data: characteristics of influenza virus reinfection”. In: *International Journal of Infectious Diseases* 120 (2022), pp. 135–141.

[158] Caroline Stein et al. “Past SARS-CoV-2 infection protection against re-infection: a systematic review and meta-analysis”. In: *The Lancet* 401.10379 (2023), pp. 833–842.

[159] Luojia Deng et al. “Risk of SARS-CoV-2 reinfection: a systematic review and meta-analysis”. In: *Scientific reports* 12.1 (2022), p. 20763.

[160] Andrew McMahon, Nicole C Robb, et al. “Reinfection with SARS-CoV-2: Discrete SIR (susceptible, infected, recovered) modeling using empirical infection data”. In: *JMIR public health and surveillance* 6.4 (2020), e21168.

[161] Hamadjam Abboubakar, Reinhard Racke, and Nicolas Schlosser. “ODE and PDE models for COVID-19, with reinfection and vaccination process for Cameroon and Germany”. In: *arXiv preprint arXiv:2504.21613* (2025).